DAMAGE ANALYSIS OF LAMINATED COMPOSITE BEAMS UNDER BENDING LOADS USING THE LAYER-WISE THEORY

A Dissertation

by

WOOK JIN NA

Submitted to the Office of Graduate Studies of
Texas A&M University
in partial fulfillment of the requirements for the degree of

DOCTOR OF PHILOSOPHY

May 2008

Major Subject: Mechanical Engineering

DAMAGE ANALYSIS OF LAMINATED COMPOSITE BEAMS UNDER BENDING LOADS USING THE LAYER-WISE THEORY

A Dissertation

by

WOOK JIN NA

Submitted to the Office of Graduate Studies of
Texas A&M University
in partial fulfillment of the requirements for the degree of

DOCTOR OF PHILOSOPHY

Approved by:

Chair of Committee,	Junuthula N. Reddy
Committee Members,	Harry A. Hogan
	Chii-Der Suh
	Ramesh R. Talreja
	Jay R. Walton
Head of Department,	Dennis L. O'Neal

May 2008

Major Subject: Mechanical Engineering

ABSTRACT

Damage Analysis of Laminated Composite Beams

under Bending Loads Using the Layer-Wise Theory. (May 2008)

Wook Jin Na, B.S., Korea University;

M.S., Korea Advanced Institute of Science and Technology

Chair of Advisory Committee: Dr. Junuthula N. Reddy

A finite element model based on the layer-wise theory and the von Kármán type nonlinear strains is used to analyze damage in laminated composite beams. In the formulation, the Heaviside step function is employed to express the discontinuous interlaminar displacement field at the delaminated interfaces. Two types of the most common damage modes in composite laminates are investigated for cross-ply laminated beams using a numerical approach.

First, a multi-scale analysis approach to determine the influence of transverse cracks on a laminate is proposed. In the meso-scale model, the finite element model based on the classical laminate theory provides the material stiffness reduction in terms of the crack density by computing homogenized material properties of the cracked ply. The multiplication of transverse cracks is predicted in a macro-scale beam model under bending loads. In particular, a damage analysis based on nonlinear strain fields in contrast to the linear case is carried out for a moderately large deformation.

Secondly, the effect of delamination in a cross-ply laminated beam under bending loads is studied for various boundary conditions with various cross-ply laminate lay-ups. The crack growth of delamination is predicted through investigating the strain energy release rate.

Finally, the interactions of a transverse crack and delamination are considered for beams of different configurations. The relationships between the two different damage modes are described through the density of intralaminar cracks and the length of the interlaminar crack.

It is found that geometric nonlinearity plays an important role in progression of interlaminar cracks whereas growth of intralaminar cracks is not significantly influenced. This study also shows that the mixture of fracture mode I and II should be considered for analysis of delamination under bending loads and the fracture mode leading delamination changes as the damage develops. The growth of delamination originated from the tip of the transverse crack is found to strongly depend on the thickness of 90-degree layers as well as the transverse crack density. Further, the effect of interfacial crack growth on the transverse cracking can be quatitatively determined by the delamination length, the thickness of 90-degree layers and the transverse crack density.

DEDICATION

To

my beloved wife, Aerim

and

our precious princess, Jeeho.

ACKNOWLEDGEMENTS

I would like to sincerely thank my committee chair, Dr. J. N. Reddy who led me to a higher point and supported my research in every aspect. His incessant passion for learning and teaching showed me a model of what a scholar ought to be.

My gratitude goes to the committee members, Dr. Harry Hogan, Dr. Steve Suh, Dr. Ramesh Talreja, and Dr. Jay Walton, for providing guidance and insight throughout the course of this research work. In particular, I would like to thank Dr. Ramesh Talreja for his deep interest in my research and discussion.

I would also like to convey my gratitude to Dr. Xin-Lin Gao and Dr. Jose Roessett for their time and suggestions.

All of my memories that I shared with my colleagues at ACML will be cherished and I wish good luck to each one of them. Special thanks go to Vinu and Ginu Unnithan for their friendship, help and discussion that made my stay at TAMU more enjoyable.

I will certainly remember all of the friends that I met at TAMU. Their smile and assistance added priceless reminiscence to my experience at Aggieland.

Most of all, thanks to my wife, Aerim, for her unchanged love and to Jeeho for being our daughter. Without their love and support, none of this research work would have proceeded.

Finally, thanks to my father and my brother for their encouragement and to my parents in-laws for their support and patience.

TABLE OF CONTENTS

CHAPTER Page

CHAPTER Page

LIST OF FIGURES

FIGURE Page

FIGURE Page

FIGURE Page

FIGURE Page

FIGURE Page

LIST OF TABLES

CHAPTER I

INTRODUCTION

1.1 Background

The composite materials are one of the most widely used engineering materials in mechanical structures due to its high strength and relatively light weight. The composite materials are composed of matrix and reinforcement materials. Matrix is considered as a continuous phase and the reinforcement as a discontinuous phase. The reinforcement is often supplied in the form of fibers and the matrix materials are often made of metals, ceramics, or polymers. The unidirectional fiber-reinforced composites are widely employed in forming composite laminates.

Unidirectional layers are stacked with different fiber orientation to achieve desired stiffness, strength, and thermal characteristics. The strength of a laminate in the fiber direction is higher than that in the direction of normal to the fiber direction. The sudden change in the material between the layers with different orientation angles often results in concentration of the local stresses. Hence, since laminates are made of layers with different orientations, damage in the laminate appears to be inevitable under service loads.

When unidirectional composites are subjected to various loading conditions, sub-critical damage precedes in the laminated composites before a catastrophic failure

---

The journal model is *IEEE Transactions on Automatic Control*.

prohibits the material from performing the structural function. Initiation of damage may not directly attribute to the failure of structure, but the stiffness and the strength can be considerably weakened. Unlike the macroscopic cracks on the surface of a structure, microscopic damage in the composite laminate is developed. Therefore, prediction of formation of damage and accurate assessment of the effect of damage in the laminate are crucial to design the structure using the composite laminates.

The predominant damage mode found in cross-ply laminates is matrix cracks in the plies with fibers oriented in off-axis to the direction of loading. Especially when those cracks form along the transverse direction to the major load, they are called transverse cracks. These cracks are usually arrested by the adjacent plies having different orientation angles, so the transverse cracks do not propagate across the neighboring plies and the matrix cracks often called intralaminar damage. Such matrix cracks within the off-axis plies multiply the number of cracks according to the loading condition, but the number of matrix cracks is also bounded. Thus, the maximum number of cracks in a unit length of specimen shows a characteristic damage state (CDS). The multiplication of transverse matrix cracks appears to reach a saturation state when the CDS is reached.

Another damage mode frequently found in the composite laminates is the separation of layers, called delamination. The cracks formed between the interfaces of the layers show a growth along the interface. Therefore, delamination is also called interlaminar damage. Delamination can occur at the edge of the laminate under the unidirectional tensile load due to concentration of the interlaminar shear stress as well as normal stress. Delamination can also develop within the laminate depending on the

stacking configuration and loading conditions. In impact or fatigue tests, delamination is often initiated from the transverse crack tips.

In order to take these damage modes into account in a numerical model based on the finite element analysis, the accuracy of the solutions obtained from the model is a critical issue because initiation of damage is a localized phenomenon. If the application of computational damage results to a practical structure is aimed, the structural base model must accommodate accurate description of the kinematic behavior of layers in the laminate and the damage mode as well.

1.2 Literature Review

1.2.1 Laminated Beam Model

A simple analytical model of a laminated beam is provided by a beam theory combined with the laminate theory. The Euler-Bernoulli beam theory (EBT) and Timoshenko beam theory (TBT) are the most often used beam models due to the simplicity of formulation and relatively accurate solutions for slender beams. The material properties of each lamina can be taken care of by the laminate theory and the whole laminate can be dealt with as simple stacks of the laminas. This idea is often called equivalent single layer laminate theories (ESL) [1]. However, when the thickness of the laminated beam becomes moderately thick, the lack of accuracy stemming from neglecting variation of the transverse shear strain through the thickness causes difficulty in predicting accurate stress fields in practical applications. To capture the actual kinematic behavior of transverse shear deformation, attempts have been made by introducing high order

theories such as the third order theory [2, 3]. Nevertheless, beam theories in conjunction with the laminate theory fail to assess the localized stresses with a high accuracy, which is often required for evaluating ply level responses such as in damage analysis.

In contrast to the equivalent single layer theories, both of the intralaminar and the interlaminar responses can be assessed with a high accuracy in the layer-wise theory(LWT). The layer-wise laminated beam model can be seen as a simplified version of the layer-wise laminate plate model of Reddy [4]. In the original work of Reddy, the displacement-based theory of laminate plates has been treated. The main idea of Reddy's layer-wise theory is that the three-dimensional elasticity theory can be reduced to a two dimensional laminate theory by assuming the displacement field to vary through the thickness as explicit functions of the thickness coordinate. Several studies ensued by making use of the layer-wise plate theory of Reddy to analyze bending beams [5, 6]. However, most of the works have dealt with linear beams based on the assumption of linearized strain fields. Although the linear layer-wise beam model is easy to formulate and gives a satisfactory solution within the range of small deformation, the nonlinear characteristics under a large deformed behavior cannot be captured.

1.2.2 Damage in Laminated Composites

A. *Transverse cracking – intralaminar damage*

Reifsnider and Masters [7] made an observation on the characteristic damage state where the matrix cracks are saturated through a tensile test on the cross-ply. They pointed that the tensile strain to initiate the transverse crack depends on the thickness of the 90-

degree ply. Bader *et al.* [8] also conducted a tensile test on cross-ply laminates and concluded that the state of saturation of transverse cracks depends on the thickness of 90-degree plies.

A series of researchers attempted to quantify the stiffness reduction in a transversely cracked laminate. Aveston *et al*. [9] proposed a so called "shear lag model" to model the stress transfer between fibers and matrix. This model is based on one dimensional analysis and was employed by Garrett and Bailey [10] and others [11, 12] to estimate the effective stiffness in a cracked laminate.

Hashin [13] derived a variational solution to the stress field in a cross ply laminate under the assumption of uniformly distributed transverse cracks in 90-degree layer. His approach was a two dimensional analysis and adopted and modified by many[14-16] to obtain the closed form solution of the normal and shear stresses as well as the axial stresses in the cracked 90-degree layers.

The continuum damage mechanics (CDM) has been studied profoundly and refined by a number of researchers [17, 18] since Kachanov [19] introduced the concept. Talreja [20, 21] is credited for applying the CDM theory systematically to a practical model. In the CDM model of Talreja, the material coefficients are described at the level of laminated structure, that is, a macro scale. Hence, the characteristics of each ply are smeared out in the macro scale system, and the stiffness change in the individual ply of laminate structures cannot be specified. To overcome this shorthand, Thionnet and Renard [22] attempted to apply Talreja's model to the ply level by using the classic laminate theory for the transverse crack damage in cross-plies. Similarly, the damaged

material stiffness coefficients of the individual damaged ply were proposed by Boniface *et al.* [23]. In addition to those, Li *et al.* [24] employed the strain energy equivalence to obtain the material stiffness coefficients of the individual damaged ply. The view that the transverse cracks in the laminate structure are local phenomena has been justified by the experimental observations and the results of the numerical computation [22].

B. *Delamination – interlaminar damage*

The common sequences of the actual damage which a composite laminated structure suffers are reported as transverse cracking followed by delamination in many experimental observations [8, 25-27]. Free-edge delamination is observed in the uniaxial tensile test and internal delamination is also found under various loading conditions. In many cases, the interfacial cracks appear to be originated from the tips of the precedent transverse cracks. For cross-ply laminates, 90-degree plies are susceptible to the transverse cracks and they result in delamination at the interfaces of the transversely cracked 90-degree plies and the adjacent 0-degree plies.

Delamination is often analyzed using the principles of fracture mechanics because delamination has more similarities to the growing crack in the framework of fracture mechanics than transverse matrix cracking. In the matrix cracking, the progress of damage is measured by the multiplying number of cracks in the damaged layer. However, the crack length is the measure of the damage growth in delamination and it is predicted by estimating the strain energy release rate.

Griffith [28] proposed a condition for a crack to extend using the principle of minimum total potential energy by equating the strain energy increase rate to the crack length due to forming new surfaces and the potential energy of the crack surface rate to the crack length. This condition is called Griffith criterion for a crack to grow. Griffith criterion has been mathematically and thermodynamically improved by Rice [29] who postulated a contour integral that is path independent as the change in potential energy for a virtual crack extension. This special integral is known as *J*-integral under the context of fracture mechanics .Gurtin [30] later showed that *J*-integral is equivalent to the strain energy release rate for the linear elastic material.

Pagano and Pipes [31] provided an analytic solution to the distribution of the interlaminar transverse normal stress along the interface of free edge delamination. They also conducted an experiment to check of the free edge phenomenon. Kim [32, 33] reported the characteristics of free edge delamination under tensile loads and attempted to give a criterion for the onset of delamination by a strength criterion [34]. Brewer and Lagace [35] also proposed a quadratic stress criterion for initiation of delamination.

Wang [36] asserted that the rate of energy release during crack extension is a material property, which is known as the critical energy release rate, and the critical strain energy release rate is determined experimentally by a procedure in that a controlled stable crack growth is examined. Wang and his colleagues intensively investigated delamination phenomena related to transverse cracks and produced useful information about the strain energy release rate through a series of works [25, 27, 37, 38].

The strain energy release rate is suggested as a criterion for delamination growth

by a number of others [26, 39, 40]. Among those, Sih et al. [41] and O'brien [42] addressed different contributions of the strain energy release rate depending on the failure mode, and pointed out that the total mixed mode strain energy release rate controls the onset of edge delamination under cyclic loads. The strain energy release rates of mixed modes are considered by Wilkins *et al*. [43] and Hahn [44], too.

C. *Damage under bending loads*

Though damage in the composite laminates has been investigated in depth for decades, the major contribution was attributed to the case under the uniaxial tensile load. The damage in composite laminates under bending loads is paid attention in relatively recent studies. Usually under the bending loads, both matrix cracking and delamination damage are observed and the failure modes are also mixed in the interlaminar cracks. Delamination induced by matrix cracking under transverse loading was observed by experiments, especially in impact tests [45-47].

Echaani *et al.* [48] investigated the damage progression in a flexural test and reported the formation of matrix cracking and delamination. They also observed the failure in 0-degree ply depending on the lay-ups. Murri and Guynn [49] conducted experiments to find the critical strain energy release rate for the delamination growth from matrix cracks under three different bending boundary conditions. Choi *et al*. [50, 51] reported the damage sequence in a low velocity impact test and observed the different delamination behaviors according to the location of crack. The matrix crack with an angle of 45 degree is also observed in a low velocity impact by Salpekar [52].

He claimed that delamination during the impact event cannot be characterized by the critical strain energy release rate of Mode II alone.

Delamination cracks originated from transverse cracks which are assumed to be uniformly distributed in the laminate is studied by Kim and Im [53]. They applied several different plane loading conditions to the unit cell model. Liu and Chang [54] found that Mode I fracture dominates the delamination initiation, but the other modes' fracture toughness govern the delamination propagation through a quasi-static vertical load at the center of clamped plate. Zhang and Lewandowski [55] performed a slow four point bending test on pre-damaged bi-layer metal-matrix composites. They observed the transverse crack tip merged into the pre-existing delamination at the middle interface under the four point bending. Dharani et al. [56] studied the interactions between the transverse cracks and delamination in $[0_m / 90_n]_S$ cross ply laminate and they concluded that the two damage modes compete with each other depending on the damage state. Kuriakose [57] studied the delamination at the tip of transverse crack in cross ply by making use of the variational approach and the finite element method.

More studies on the damage in the composite laminates under bending loads can be found in literatures [58-61].

1.3 Objectives of the Present Research

The whole progression of damage developed in the laminated composite beams under bending loads is investigated using the layer-wise theory and the finite element method. The progressive damage behavior includes the initiation of damage, its propagation, and

inducing other damage modes.

1.3.1 Developing a Fully Layer-wise Nonlinear Beam Model

As mentioned in the previous section, the high accuracy of solutions to the stress fields of the localized region in the laminate is crucial for studying damage. Thus, the finite element model is developed to meet the kinematic requirements that capture the transverse shear deformation and evaluate the precise stresses in a laminated beam. For this purpose, the layer-wise theory is employed represent the kinematics of the beam. The present layer-wise model is capable of taking into account the geometric nonlinearity due to moderately large flexural deformation by including von Kármán type nonlinear strains.

The present research work presents a complete formulation of the layer-wise beam model derived using nonlinear strain fields followed by the finite element model. The layer-wise beam model is extended to another level that accounts for discontinuous displacement fields between layers to analyze delamination damage.

1.3.2 Analysis of Transverse Crack

Basically the multiscale approach is attempted to predict the transverse cracking and its effect in composite laminates.

The transverse cracks in the laminated beam are treated as a localized damage in the cracked ply and the numerical computation is adopted to determine the damaged ply's homogenized material stiffness in the mesoscale. The unit cell model is used to

obtain the stiffness reduction in the cracked layer and the effective material stiffness is applied to the macroscale beam structure model. In the structural length scale, the initiation and propagation of the transverse cracks are predicted under bending loads.

1.3.3 Analysis of Delamination

The characteristics of delamination in the laminated beam under bending are investigated for the various cases of bending loads as well as the laminate lay-ups.

The change of strain energy release rate is examined to predict the delamination growth. Also, mixture of failure modes in the laminate under bending is considered and the contribution of each mode's strain energy release rate to the total strain energy release rate is studied so that the predominant mode in delamination can be identified.

Interactions between transverse cracks and delamination are studied through the case of delamination originated from transverse cracks. The effect of varying transverse crack density on the growth of delamination is highlighted from that perspective.

CHAPTER II

LAYER-WISE BEAM MODEL

2.1 Laminated Beam Theories

2.1.1 Equivalent Single Layer Theory

Two commonly used laminated beam models are making use of Euler-Bernoulli beam theory (EBT) and Timoshenko beam theory (TBT) (see Reddy [62]). These two conventional beam theories are widely employed to give good results on analysis of relatively long and thin beams.

In EBT, the displacement field is given as

$$u(x,z) = u_0(x,z) - z\frac{\partial w_0}{\partial x} \tag{2.1a}$$

$$v(x,z) = 0 \tag{2.1b}$$

$$w(x,z) = w_0(x,z) \tag{2.1c}$$

where (u_0, w_0) are the displacement components along the (x,z) coordinate directions, respectively, of a point on $z = 0$ plane and the displacement fields in equations (2.1a)-(2.1c) are valid under the Euler-Bernoulli hypothesis.

On the other hand, the displacement field in TBT is given by

$$u(x,z) = u_0(x,z) + z\phi(x) \tag{2.2a}$$

$$v(x,z) = 0 \tag{2.2b}$$

$$w(x,z) = w_0(x,z) \tag{2.2c}$$

where $\phi(x)$ is an independent function of x and denotes rotation about the y axis. The strict kinematic assumption of Euler-Bernoulli hypothesis, namely, the normality assumption, is relaxed in TBT by allowing independent rotation of a transverse normal line, i.e., include shear deformation, γ_{xz}.

In the course of developing an analytic model of the laminated beam, the kinematic representation of the deformation can be implemented in a finite element model with each layer's material properties. Although the material properties of each layer are taken into account, the equivalent single layer (ESL) theories (i.e. EBT and TBT) cannot accurately capture the interlaminar stresses, especially for the thick and short beams. On top of that, the ESL beam models often turn out to be improper for the damage analysis because the damage analysis requires a highly accurate assessment of localized regions [1].

2.1.2 Layer-wise Theory

Similar to the layer-wise plate theory of Reddy [1, 4], the total displacement fields of the laminated beam are written as [6]

$$u(x,z)=\sum_{I=1}^{N}U_I(x)\Phi^I(z) \tag{2.3a}$$

$$v(x,z)=0 \tag{2.3b}$$

$$w(x,z)=\sum_{I=1}^{M}W_I(x)\Psi^I(z) \tag{2.3c}$$

where (U_I,W_I) denote the Ith nodal values of (u,w) while Φ^I and Ψ^I are the global interpolation functions for the longitudinal displacement and the transverse displacement through the thickness, respectively. N and M in equations (2.3a)-(2.3c) are the numbers of nodes through the thickness for the longitudinal displacement and the transverse displacement respectively. In general, $\Phi^I \neq \Psi^I$ and $N \neq M$. It is worth addressing that the kinematic displacement fields are expressed in terms of the transverse directional coordinate as well as the longitudinal one.

The von Kármán type nonlinear strains associated with the given displacement fields are

$$\begin{aligned}\varepsilon_{xx}&=\frac{\partial u}{\partial x}+\frac{1}{2}\left(\frac{\partial w}{\partial x}\right)^2\\&=\sum_{I=1}^{N}\frac{dU_I(x)}{dx}\Phi^I(z)+\frac{1}{2}\left(\sum_{I=1}^{M}\frac{dW_I(x)}{dx}\Psi^I(z)\right)\left(\sum_{J=1}^{M}\frac{dW_J(x)}{dx}\Psi^J(z)\right)\end{aligned} \tag{2.4a}$$

$$\varepsilon_{zz}=\frac{\partial w}{\partial z}=\sum_{I=1}^{M}W_I(x)\frac{d\Psi^I(z)}{dz} \tag{2.4b}$$

$$\gamma_{xz} = \frac{\partial w}{\partial x} + \frac{\partial u}{\partial z} = \sum_{I=1}^{M} \frac{dW_I(x)}{dx} \Psi^I(z) + \sum_{I=1}^{N} U_I(x) \frac{d\Phi^I(z)}{dx} \tag{2.4c}$$

$$\varepsilon_{yy} = \gamma_{xy} = \gamma_{yz} = 0\,. \tag{2.4d}$$

For the *k*th orthotropic lamina, the stresses can be obtained from the 3-D stress-strain relation,

$$\begin{Bmatrix} \sigma_{xx} \\ \sigma_{yy} \\ \sigma_{zz} \\ \sigma_{yz} \\ \sigma_{xz} \\ \sigma_{xy} \end{Bmatrix}^{(k)} = \begin{bmatrix} \overline{C}_{11} & \overline{C}_{12} & \overline{C}_{13} & 0 & 0 & \overline{C}_{16} \\ \overline{C}_{21} & \overline{C}_{22} & \overline{C}_{23} & 0 & 0 & \overline{C}_{26} \\ \overline{C}_{31} & \overline{C}_{32} & \overline{C}_{33} & 0 & 0 & \overline{C}_{36} \\ 0 & 0 & 0 & \overline{C}_{44} & \overline{C}_{45} & 0 \\ 0 & 0 & 0 & \overline{C}_{54} & \overline{C}_{55} & 0 \\ \overline{C}_{61} & \overline{C}_{62} & \overline{C}_{63} & 0 & 0 & \overline{C}_{66} \end{bmatrix}^{(k)} \begin{Bmatrix} \varepsilon_{xx} \\ \varepsilon_{yy} \\ \varepsilon_{zz} \\ \gamma_{yz} \\ \gamma_{xz} \\ \gamma_{xy} \end{Bmatrix}^{(k)} \tag{2.5}$$

where $\overline{C}_{ij}^{(k)}$ are the transformed elastic coefficients [1], which are symmetric for orthotropic materials.

The governing equations of the layer-wise beam depicted in Fig. 2.1 are derived from the principle of virtual displacements [1, 62],

$$0 = \delta U + \delta V \tag{2.6}$$

where the virtual strain energy δU and the virtual work done δV are given by

$$\delta U = \int_{x_a}^{x_b} \int_{-\frac{h}{2}}^{\frac{h}{2}} \left(\sigma_{xx} \delta \varepsilon_{xx} + \sigma_{zz} \delta \varepsilon_{zz} + \sigma_{xz} \delta \gamma_{xz} \right) dz dx \tag{2.7a}$$

$$\delta V = -\int_{x_a}^{x_b} \left(f_b(x) \delta u(x, -\tfrac{h}{2}) + f_t(x) \delta u(x, \tfrac{h}{2}) \right) dx$$

$$- \int_{x_a}^{x_b} \left(q_b(x) \delta w(x, -\tfrac{h}{2}) + q_t(x) \delta w(x, \tfrac{h}{2}) \right) dx \,. \tag{2.7b}$$

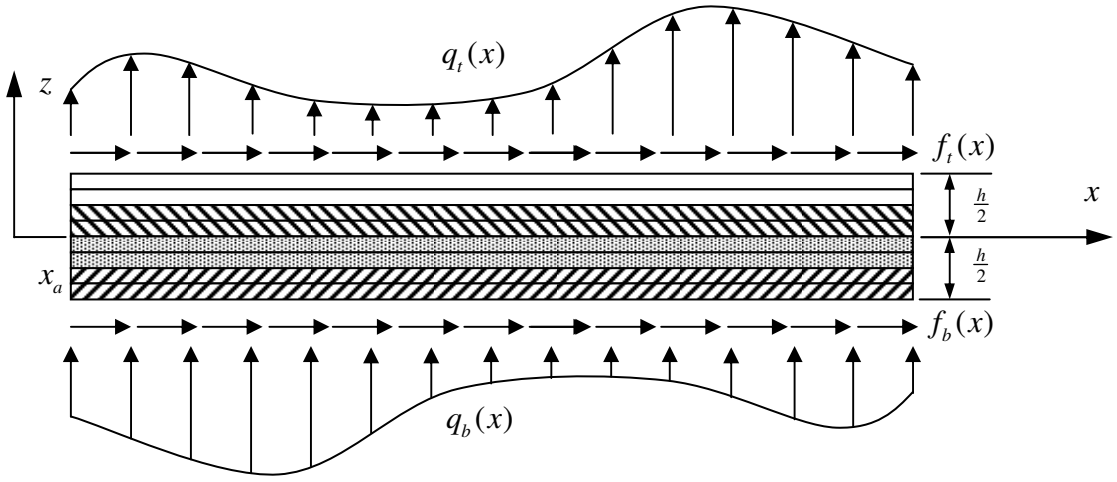

Fig. 2.1. Laminated beam model based on the layer-wise theory

Applying the stress-strain relations in equation (2.5) and displacement field equations (2.3a)-(2.3c) to (2.7a) and (2.7b), the virtual energy and the virtual work done can be described in terms of the nodal displacements as follows

$$\delta U = \int_{x_a}^{x_b} \sum_{I=1}^{N} \left(N_{xx}^{I} \frac{d\delta U_I}{dx} + Q_x^I \delta U_I \right) dx$$

$$+\int_{x_a}^{x_b}\sum_{I=1}^{N}\left(\sum_{J=1}^{M}N_{xx}^{IJ}\frac{d\delta W_I}{dx}\frac{dW_J}{dx}+Q_z^I\delta W_I+\tilde{Q}_x^I\frac{d\delta W_I}{dx}\right)dx \tag{2.8a}$$

$$\delta V=-\int_{x_a}^{x_b}\left(f_b\delta U_1+f_t\delta U_N\right)dx-\int_{x_a}^{x_b}\left(q_b\delta W_1+q_t\delta W_M\right)dx \tag{2.8b}$$

where

$$N_{xx}^I=\sum_{J=1}^{N}A_{11}^{IJ}\frac{dU_J}{dx}+\frac{1}{2}\sum_{J=1}^{M}\sum_{K=1}^{M}B_{11}^{IJK}\frac{dW_J}{dx}\frac{dW_K}{dx}+\sum_{J=1}^{M}\tilde{A}_{13}^{IJ}W_J \tag{2.9a}$$

$$N_{xx}^{IJ}=\sum_{K=1}^{N}B_{11}^{KIJ}\frac{dU_K}{dx}+\frac{1}{2}\sum_{K=1}^{M}\sum_{L=1}^{M}D_{11}^{IJKL}\frac{dW_K}{dx}\frac{dW_L}{dx}+\sum_{K=1}^{M}\tilde{B}_{13}^{IJK}W_K \tag{2.9b}$$

$$Q_x^I=\sum_{J=1}^{M}\bar{B}_{55}^{IJ}\frac{dW_J}{dx}+\sum_{J=1}^{N}\bar{A}_{55}^{IJ}U_J \tag{2.9c}$$

$$\tilde{Q}_x^I=\sum_{J=1}^{M}\bar{D}_{55}^{IJ}\frac{dW_J}{dx}+\sum_{J=1}^{N}\bar{B}_{55}^{JI}U_J \tag{2.9d}$$

$$Q_z^I=\sum_{J=1}^{N}\tilde{A}_{31}^{JI}\frac{dU_J}{dx}+\frac{1}{2}\sum_{J=1}^{M}\sum_{K=1}^{M}\tilde{B}_{31}^{JKI}\frac{dW_J}{dx}\frac{dW_K}{dx}+\sum_{J=1}^{M}\hat{A}_{33}^{IJ}W_J \tag{2.9e}$$

and

$$A_{11}^{IJ}=\sum_{k=1}^{Ne}\int_{z_k}^{z_{k+1}}C_{11}^{(k)}\Phi^I\Phi^J dz \tag{2.10a}$$

$$\tilde{A}_{13}^{IJ}=\tilde{A}_{31}^{IJ}=\sum_{k=1}^{Ne}\int_{z_k}^{z_{k+1}}\bar{C}_{13}^{(k)}\Phi^I\frac{d\Psi^J}{dz}dz \tag{2.10b}$$

$$\overline{A}_{55}^{IJ} = \sum_{k=1}^{Ne} \int_{z_k}^{z_{k+1}} \overline{C}_{55}^{(k)} \frac{d\Phi^I}{dz} \frac{d\Phi^J}{dz} dz \tag{2.10c}$$

$$\hat{A}_{33}^{IJ} = \sum_{k=1}^{Ne} \int_{z_k}^{z_{k+1}} \overline{C}_{33}^{(k)} \frac{d\Psi^I}{dz} \frac{d\Psi^J}{dz} dz \tag{2.10d}$$

$$\overline{B}_{55}^{IJ} = \sum_{k=1}^{Ne} \int_{z_k}^{z_{k+1}} \overline{C}_{55}^{(k)} \frac{d\Phi^I}{dz} \Psi^J dz \tag{2.10e}$$

$$\overline{D}_{55}^{IJ} = \sum_{k=1}^{Ne} \int_{z_k}^{z_{k+1}} \overline{C}_{55}^{(k)} \Psi^I \Psi^J dz \tag{2.10f}$$

$$B_{11}^{IJK} = \sum_{k=1}^{Ne} \int_{z_k}^{z_{k+1}} \overline{C}_{11}^{(k)} \Phi^I \Psi^J \Psi^K dz \tag{2.10g}$$

$$\tilde{B}_{13}^{IJK} = \tilde{B}_{31}^{IJK} = \sum_{k=1}^{Ne} \int_{z_k}^{z_{k+1}} \overline{C}_{13}^{(k)} \Psi^I \Psi^J \frac{d\Psi^K}{dz} dz \tag{2.10h}$$

$$D_{11}^{IJKL} = \sum_{k=1}^{Ne} \int_{z_k}^{z_{k+1}} \overline{C}_{11}^{(k)} \Psi^I \Psi^J \Psi^K \Psi^L dz\,. \tag{2.10i}$$

Note that *Ne* is the number of physical layers in the laminate, and that three or four superscripts are introduced due to the von Kármán type nonlinearity. That is, only two superscripts will appear in the laminate stiffness coefficients if linear strain fields are assumed.

2.2 Finite Element Model

The displacement field (2.3a)-(2.3c) are interpolated by appropriate interpolation functions in order to represent a finite element model for a layer-wise beam, as follows

$$U_I(x) = \sum_{j=1}^{p} U_I^j \varphi_j^{(1)}(x) \tag{2.11a}$$

$$W_I(x) = \sum_{j=1}^{q} W_I^j \varphi_j^{(2)}(x) \tag{2.11b}$$

where p and q are the number of nodes per 1-D element used to approximate the longitudinal and transverse deflections, respectively, and U_I^j and W_I^j are the displacement values at the jth node along the longitudinal (x) direction of Ith beam element. The interpolation functions, $\varphi_j^{(1)}$ and $\varphi_j^{(2)}$ are the 1-D Lagrangian polynomials with respect to the longitudinal and transverse deflections at the jth node of each beam element. Substituting the displacement fields (2.11a) and (2.11b) in the longitudinal direction and their variational forms

$$\delta U_I = \varphi_i^{(1)}(x) \tag{2.12a}$$

$$\delta W_I = \varphi_i^{(2)}(x) \tag{2.12b}$$

into the energy equations (2.8a) and (2.8b) yields the equations for the finite element model as

$$\sum_{j=1}^{p}\sum_{J=1}^{N} K_{ij}^{(11)IJ} U_J^j + \sum_{j=1}^{q}\sum_{J=1}^{M} K_{ij}^{(12)IJ} W_J^j = {}^1F_i^I$$

$$(i = 1, 2, \cdots, p \text{ and } I = 1, 2, \cdots, N) \tag{2.13a}$$

$$\sum_{j=1}^{p}\sum_{J=1}^{N} K_{ij}^{(21)IJ} U_J^j + \sum_{j=1}^{q}\sum_{J=1}^{M} K_{ij}^{(22)IJ} W_J^j = {}^2F_i^I$$

$$(i = 1, 2, \cdots, q \text{ and } I = 1, 2, \cdots, M) \quad (2.13b)$$

where

$$K_{ij}^{(11)IJ} = \int_{x_a}^{x_b} \left(A_{11}^{IJ} \frac{d\varphi_i^{(1)}}{dx} \frac{d\varphi_j^{(1)}}{dx} + \overline{A}_{55}^{IJ} \varphi_i^{(1)} \varphi_j^{(1)} \right) dx \quad (2.14a)$$

$$K_{ij}^{(12)IJ} = \int_{x_a}^{x_b} \left[\frac{1}{2} \left(\sum_{K=1}^{M} B_{11}^{IJK} \frac{dW_K}{dx} \right) \frac{d\varphi_i^{(1)}}{dx} \frac{d\varphi_j^{(2)}}{dx} + \tilde{A}_{13}^{IJ} \frac{d\varphi_i^{(1)}}{dx} \varphi_j^{(2)} + \overline{B}_{55}^{IJ} \varphi_i^{(1)} \frac{d\varphi_j^{(2)}}{dx} \right] dx \quad (2.14b)$$

$$K_{ij}^{(21)IJ} = \int_{x_a}^{x_b} \left[\left(\sum_{K=1}^{M} B_{11}^{IKJ} \frac{dW_K}{dx} \right) \frac{d\varphi_i^{(2)}}{dx} \frac{d\varphi_j^{(1)}}{dx} + \tilde{A}_{31}^{JI} \varphi_i^{(2)} \frac{d\varphi_j^{(1)}}{dx} + \overline{B}_{55}^{JI} \frac{d\varphi_i^{(2)}}{dx} \varphi_j^{(1)} \right] dx \quad (2.14c)$$

$$\begin{aligned} K_{ij}^{(22)IJ} = & \int_{x_a}^{x_b} \frac{1}{2} \left(\sum_{K=1}^{M}\sum_{L=1}^{M} D_{11}^{IJKL} \frac{dW_K}{dx} \frac{dW_L}{dx} \right) \frac{d\varphi_i^{(2)}}{dx} \frac{d\varphi_j^{(2)}}{dx} dx \\ & + \int_{x_a}^{x_b} \left[\left(\sum_{K=1}^{M} \tilde{B}_{13}^{IKJ} \frac{dW_K}{dx} \right) \frac{d\varphi_i^{(2)}}{dx} \varphi_j^{(2)} + \frac{1}{2} \left(\sum_{K=1}^{M} \tilde{B}_{31}^{JKI} \frac{dW_K}{dx} \right) \varphi_i^{(2)} \frac{d\varphi_j^{(2)}}{dx} \right] dx \\ & + \int_{x_a}^{x_b} \left[\hat{A}_{33}^{IJ} \varphi_i^{(2)} \varphi_j^{(2)} + \overline{D}_{55}^{IJ} \frac{d\varphi_i^{(2)}}{dx} \frac{d\varphi_j^{(2)}}{dx} \right] dx \end{aligned} \quad (2.14d)$$

and

$$
{}^{1}F_i^I = \begin{cases} \int_{x_a}^{x_b} f_b(x)\varphi_i^{(1)} dx & \left(I = 1\right) \\ \int_{x_a}^{x_b} f_t(x)\varphi_i^{(1)} dx & \left(I = N\right) \\ 0 & \left(I = 2,3,\cdots,N-1\right) \end{cases} \tag{2.15a}
$$

$$
{}^{2}F_i^I = \begin{cases} \int_{x_a}^{x_b} q_b(x)\varphi_i^{(2)} dx & \left(I = 1\right) \\ \int_{x_a}^{x_b} q_t(x)\varphi_i^{(2)} dx & \left(I = M\right) \\ 0 & \left(I = 2,3,\cdots,M-1\right) \end{cases} \tag{2.15b}
$$

Note that the coefficient matrices $\left[K^{(12)}\right]$, $\left[K^{(21)}\right]$ and $\left[K^{(22)}\right]$ contain nonlinearity in such a way that they are functions of the unknown $W(x)$, also note that the finite element stiffness matrix is unsymmetric because $\left[K^{(12)}\right]^T \neq \left[K^{(21)}\right]$ for the nonlinear case [63].

The equations (2.13a) through (2.15b) are used to compute the nonlinear responses based on the direct iteration scheme. The direct iteration converges if the nonlinearity is not very prominent but it tends to diverge if the nonlinearity is severe. Divergence is more likely for hardening type nonlinearity [63]. In this study, another numerical iteration scheme known as the Newton-Raphson method is employed to cover hardening types of nonlinear problems as well. The Newton-Raphson method makes use of the residual vector of the finite element equations (2.13a), (2.13b) and its Taylor's series about the solution from the previous iteration. Here the details of the Newton-Raphson method are omitted and, instead, the components of the tangent matrix[63] for the nonlinear layer-wise beam model are listed as follows

$$T_{ij}^{(11)IJ} = \int_{x_a}^{x_b} \left(A_{11}^{IJ} \frac{d\varphi_i^{(1)}}{dx} \frac{d\varphi_j^{(1)}}{dx} + \overline{A}_{55}^{IJ} \varphi_i^{(1)} \varphi_j^{(1)} \right) dx \tag{2.16a}$$

$$T_{ij}^{(12)IJ} = \int_{x_a}^{x_b} \left[\left(\sum_{K=1}^{M} B_{11}^{IJK} \frac{dW_K}{dx} \right) \frac{d\varphi_i^{(1)}}{dx} \frac{d\varphi_j^{(2)}}{dx} + \tilde{A}_{13}^{IJ} \frac{d\varphi_i^{(1)}}{dx} \varphi_j^{(2)} + \overline{B}_{55}^{IJ} \varphi_i^{(1)} \frac{d\varphi_j^{(2)}}{dx} \right] dx \tag{2.16b}$$

$$T_{ij}^{(21)IJ} = \int_{x_a}^{x_b} \left[\left(\sum_{K=1}^{M} B_{11}^{IKJ} \frac{dW_K}{dx} \right) \frac{d\varphi_i^{(2)}}{dx} \frac{d\varphi_j^{(1)}}{dx} + \tilde{A}_{31}^{JI} \varphi_i^{(2)} \frac{d\varphi_j^{(1)}}{dx} + \overline{B}_{55}^{JI} \frac{d\varphi_i^{(2)}}{dx} \varphi_j^{(1)} \right] dx \tag{2.16c}$$

$$\begin{aligned} T_{ij}^{(22)IJ} = & \int_{x_a}^{x_b} \left(\sum_{K=1}^{N} B_{11}^{IJK} \frac{dU_K}{dx} \right) \frac{d\varphi_i^{(2)}}{dx} \frac{d\varphi_j^{(2)}}{dx} dx \\ & + \int_{x_a}^{x_b} \frac{3}{2} \left(\sum_{K=1}^{M} \sum_{L=1}^{M} D_{11}^{IJKL} \frac{dW_K}{dx} \frac{dW_L}{dx} \right) \frac{d\varphi_i^{(2)}}{dx} \frac{d\varphi_j^{(2)}}{dx} dx \\ & + \int_{x_a}^{x_b} \left[\left(\sum_{K=1}^{M} \tilde{B}_{13}^{IJK} W_K \right) \frac{d\varphi_i^{(2)}}{dx} \frac{d\varphi_j^{(2)}}{dx} + \left(\sum_{K=1}^{M} \tilde{B}_{31}^{JKI} \frac{dW_K}{dx} \right) \varphi_i^{(2)} \frac{d\varphi_j^{(2)}}{dx} \right] dx \\ & + \int_{x_a}^{x_b} \left[\left(\sum_{K=1}^{M} \tilde{B}_{13}^{IKJ} \frac{dW_K}{dx} \right) \frac{d\varphi_i^{(2)}}{dx} \varphi_j^{(2)} + \overline{A}_{33}^{IJ} \varphi_i^{(2)} \varphi_j^{(2)} + A_{55}^{IJ} \frac{d\varphi_i^{(2)}}{dx} \frac{d\varphi_j^{(2)}}{dx} \right] dx \,. \end{aligned} \tag{2.16d}$$

Unlike the unsymmetric coefficient matrix in the direct iteration method, the tangent stiffness matrix is symmetric for the nonlinear case.

2.3 Numerical Examples

To demonstrate the accuracy of solutions using LWT, a simply supported laminated beam with [0/90/0] lay-up subjected to sinusoidally distributed transverse load is considered. Since an exact elasticity solution based on the linear strain fields is available

for this example problem [64], the solutions from the linear finite element models based on all three different beam theories can be compared. One-half of the simply supported laminated beam is modeled using LWT, EBT, and TBT imposing the symmetry condition of rotation being zero at the center of the beam. The meshes in the vicinity of the boundaries are gradually refined so that the Gauss points at which the stresses are computed are close enough to the end points. Also, the number and the length of elements of LWT, EBT and TBT are chosen in such a way that the Gauss points are same at which the stress is computed. A total 16 Lagrange quadratic beam elements are used for LWT and TBT while 32 Hermite cubic beam elements are used for EBT. As for the approximation of the displacement fields through the thickness in the model of LWT, two numerical layers per each physical layer are modeled using Lagrange quadratic interpolation functions for Φ^I and Ψ^I in equations (2.3a)-(2.3c). Not to mention, the finite element models based on ESL theories are incapable of representing the layer-wise kinematics of the laminated beam through the thickness (height).

The material properties of the unidirectional fibrous graphite/epoxy composite are taken as used by Pagano [64]:

$$E_1 = 25\times10^6\,\text{psi} \qquad E_2 = E_3 = 1\times10^6\,\text{psi}$$

$$G_{12} = G_{13} = 0.5\times10^6\,\text{psi} \qquad G_{23} = 0.2\times10^6\,\text{psi}$$

$$\nu_{12} = \nu_{13} = \nu_{23} = 0.25\,.$$

Fig. 2.2 (a) shows nondimensional transverse deflections versus the length-to-

thickness ratio and (b) displays the ratio of transverse deflections of each beam theory to the exact solutions. As can be seen from Fig. 2.2 , the LWT solution is in excellent agreement with the exact solutions in the range of length-to-thickness ratios considered. For the thick beams, namely, when the length-to-thickness ratio of the laminated beam is small, the ESL solutions are underestimated values compared to the LWT solutions. Especially, the EBT presents a poorer solution than the TBT does. However, as the beam gets thinner and longer, or as the length-to-thickness ratio increases, both the ESL solutions and the LWT solutions converge to the same solution.

The stresses through the thickness of the beams are shown in Fig. 2.3 through 2.5 for the linear case. The stresses are obtained at the reduced Gauss points closest to the position where each stress component reaches a maximum value. All the stresses obtained from the finite element models using LWT show very close agreement with the exact elasticity solutions whereas the ESL solutions considerably deviate from the exact elasticity solutions for the thick beam ($L/h=4$). It is noted that the transverse stress σ_{zz} is not available for the ESL beams and even the shear stress σ_{xz} cannot be obtained from the EBT due to the kinematic assumption of the theory. In contrast to the limitation of the ESL beams, the finite element model derived using the LWT is capable of yielding all three in-plane stresses as well as the deflection of the laminated beam with an excellent accuracy.

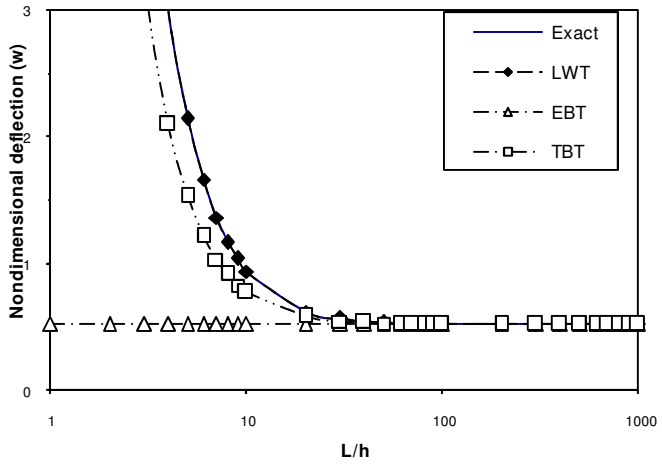

(a)

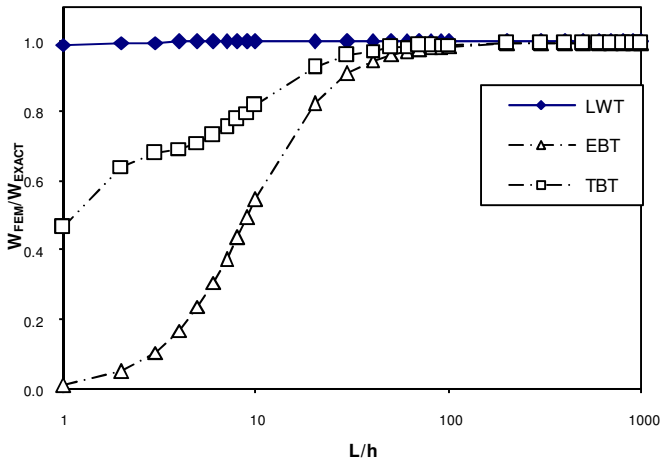

(b)

Fig. 2.2. Normalized transverse deflections of simply supported [0/90/0] laminated beams subjected to sinusoidally distributed transverse load (a) $\bar{w} = w(\frac{L}{2}, \frac{h}{2}) \frac{E_2 h^3}{q_0 L^4}$ (b) w_{FEM} / w_{Exact} at $(\frac{L}{2}, \frac{h}{2})$

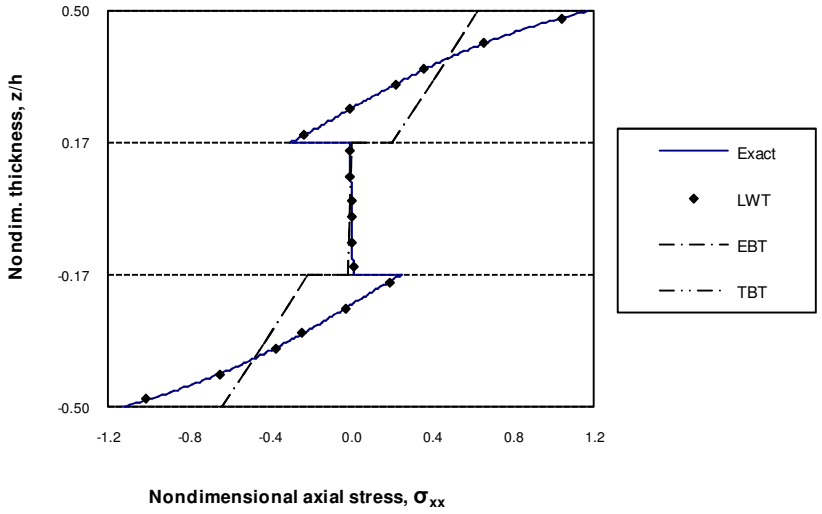

(a)

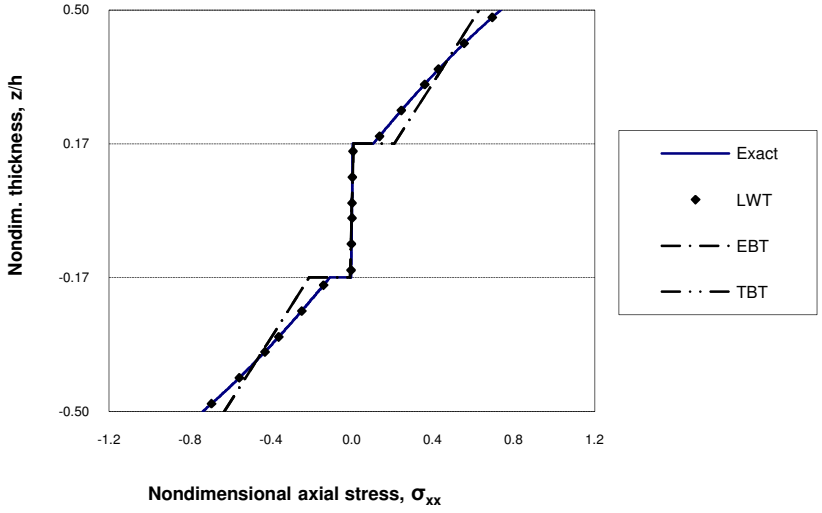

(b)

Fig. 2.3. Nondimensional axial stress $\bar{\sigma}_{xx} = \sigma_{xx}(\frac{L}{2}, z)\frac{h^2}{q_0 L^2}$ distribution through the thickness of simply supported $[0/90/0]$ laminated beams subjected to sinusoidally distributed transverse load (a) $L/h = 4$ (b) $L/h = 10$

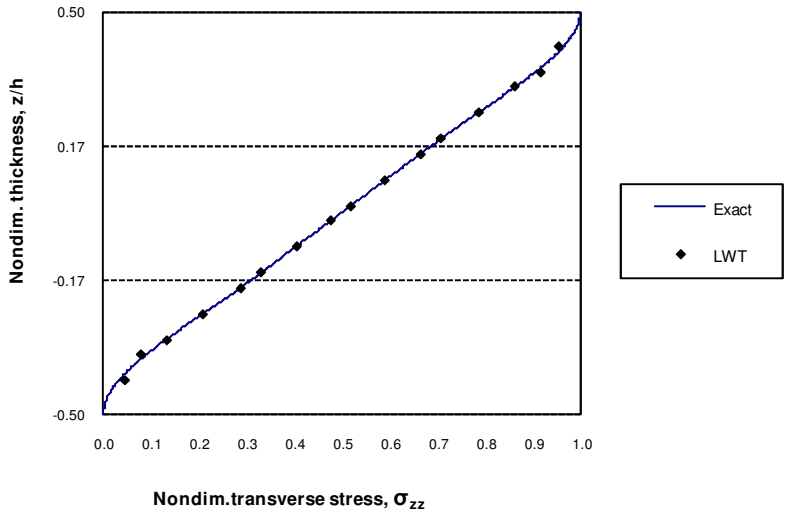

(a)

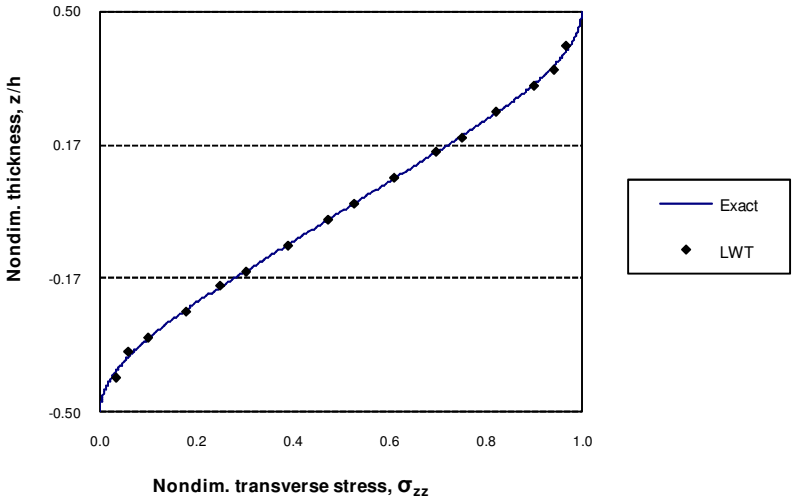

(b)

Fig. 2.4. Nondimensional transverse stress $\bar{\sigma}_{zz} = \sigma_{zz}(\frac{L}{2}, z)\frac{1}{q_0}$ distribution through the thickness of simply supported $[0/90/0]$ laminated beams subjected to sinusoidally distributed transverse load (a) $L/h = 4$ (b) $L/h = 10$

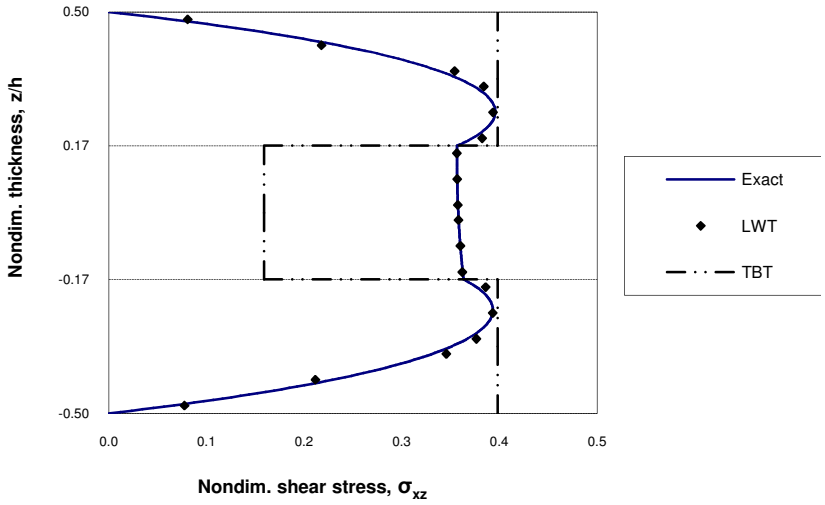

(a)

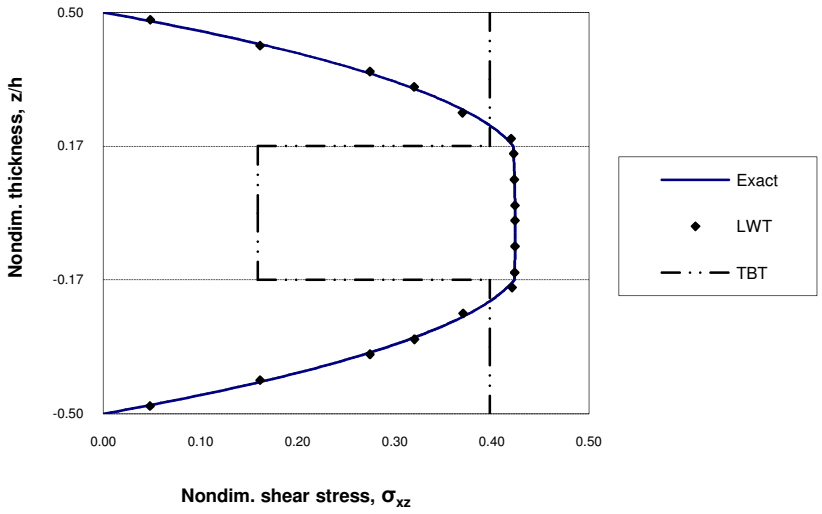

(b)

Fig. 2.5. Nondimensional shear stress $\bar{\sigma}_{xz} = \sigma_{xz}(0,z)\dfrac{h}{q_0 L}$ distribution through the thickness of simply supported [0/90/0] laminated beams subjected to sinusoidally distributed transverse load (a) $L/h = 4$ (b) $L/h = 10$

CHAPTER III

TRANSVERSE CRACKS

3.1 Transverse Cracking in Laminated Beams

In the current chapter, the transverse cracks in laminated beams are treated as a localized damage in the cracked ply, and a numerical computation will be adopted to determine the damaged ply's homogenized material stiffness. A typical unit cell of the damaged laminate is taken from one transverse crack to the next one under the assumption of uniform distance between the adjacent cracks.

3.1.1 Stiffness Reduction Scheme in Mesoscale

One of the main difficulties of using Talreja's model is that the material constants used to evaluate the damage effects are determined by experimental data, and typically, the material constant associated with the change in the shear modulus cannot be determined due to large uncertainty in the measurement [65]. To construct a complete constitutive equation of the damaged material, Thionnet *et al*. [22] evoked the conventional laminate plate theory in which the resultant homogenized material stiffness coefficients of the laminate are described as the superposition form of the material stiffnesses of the plies. In their work, the components of the homogenized material stiffness coefficients of the cracked ply have been derived on the cross-ply laminate. However, layers with any angle θ in the $[0_m / \theta_n]$ configurations are applicable to determining homogenized material stiffness coefficients of the cracked θ° ply in the laminate. Thus,

$$C_{11}^{D} = \frac{C_{22}^{H} - r^{0}C_{22}^{0} - r^{\theta}C_{22}^{\theta}}{r^{c}} \tag{3.1a}$$

$$C_{12}^{D} = \frac{C_{12}^{H} - r^{0}C_{12}^{0} - r^{\theta}C_{12}^{\theta}}{r^{c}} \tag{3.1b}$$

$$C_{22}^{D} = \frac{C_{11}^{H} - r^{0}C_{11}^{0} - r^{\theta}C_{11}^{\theta}}{r^{c}} \tag{3.1c}$$

$$C_{66}^{D} = \frac{C_{66}^{H} - r^{0}C_{66}^{0} - r^{\theta}C_{66}^{\theta}}{r^{c}} \tag{3.1d}$$

where the superscripts D, H, 0 and θ refer to the cracked ply, the total homogenized laminate, 0-degree and 90-degree ply, respectively (see Fig. 3.1). Also,

$$r^{D} = \frac{t^{D}}{h} \tag{3.2a}$$

$$r^{0} = \frac{t^{0}}{h} \tag{3.2b}$$

$$r^{\theta} = \frac{t^{\theta}}{h}. \tag{3.2c}$$

Here, a scalar damage variable is introduced to represent the damage state at a certain moment during the process of multiplication of the number of cracks, and it is defined using the geometry of Fig. 3.1 (a) as

$$\boldsymbol{D} = \frac{t^{\theta}}{l} \tag{3.3}$$

where l is the length of the unit cell of the damaged laminate. The scalar damage variable $\boldsymbol{D}$ is often referred to as the normalized crack density. The normalized crack density will be an appropriate measure of the damage if the homogenized material stiffness coefficients of the damaged laminate vary with the change of $\boldsymbol{D}$.

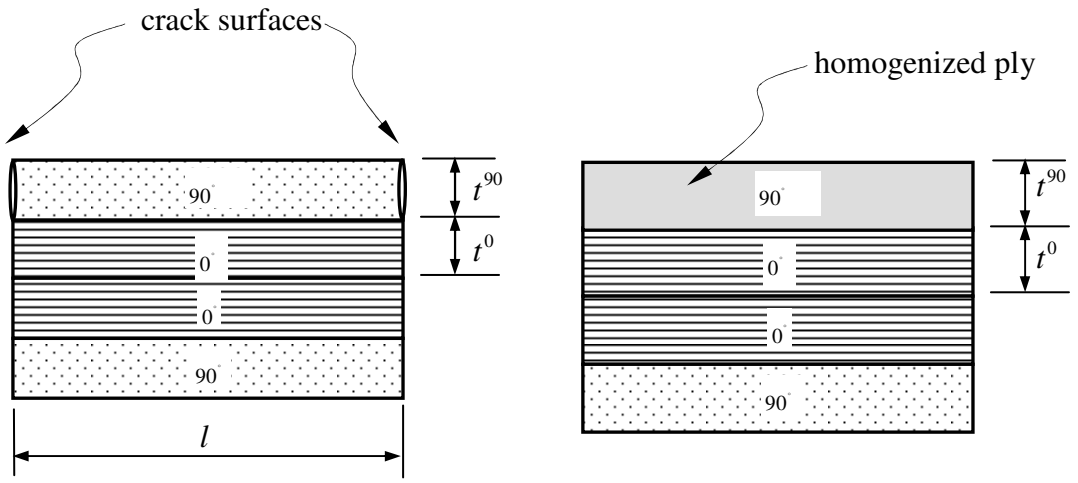

Fig. 3.1. Multiscale finite element model of $[90/0]_s$ laminated beam (a) mesoscale model including cracks (b) homogenized macroscale model

The total homogenized constitutive equation for the unit cell of a laminated beam that includes the cracked plies can be written

$$\begin{Bmatrix}\sigma_1\\ \sigma_2\\ \sigma_6\end{Bmatrix}=\begin{bmatrix}C_{11}^H & C_{12}^H & 0\\ C_{12}^H & C_{22}^H & 0\\ 0 & 0 & C_{66}^H\end{bmatrix}\begin{Bmatrix}\varepsilon_1\\ \varepsilon_2\\ \varepsilon_6\end{Bmatrix}. \tag{3.4}$$

If the homogenized material stiffness coefficients of the damaged laminate C_{ij}^H are known, the homogenized material stiffness coefficients of the cracked ply for a given damage state $\boldsymbol{D}$ are determined from equation (3.3). Yet, C_{ij}^H are the unknowns and should be determined by a proper numerical simulation.

In order to identify C_{ij}^H, the following four boundary conditions are imposed to the model (a) for one value of the damage variable $\boldsymbol{D}$,

$$i)\quad \varepsilon_1=\varepsilon_{1c}\quad,\quad \varepsilon_2=0 \tag{3.5a}$$

$$ii)\quad \varepsilon_1=\varepsilon_{1c}\quad,\quad \varepsilon_2=\varepsilon_{2c} \tag{3.5b}$$

$$iii)\quad \varepsilon_2=\varepsilon_{2c} \tag{3.5c}$$

$$iv)\quad \varepsilon_6=\varepsilon_{6c} \tag{3.5d}$$

where ε_{ic} represent arbitrary constants. Since the model (a) of Fig. 3.1 contains physical discontinuities inside the 90° ply, the strains and the stresses obtained from this model

are not unifrom. Hence, the strains and the stresses should be homogenized so that they can represent the equivalent values of homogenized material of the model (b). Using the homogenized strains and stresses computed from the unit cell model, the total homogenized material stiffness coefficients are given as

$$i)\quad C_{11}^{H} = \frac{\sigma_1}{\varepsilon_{1c}} \tag{3.6a}$$

$$ii)\quad C_{12}^{H} = \frac{\sigma_1 - C_{11}^{H}\varepsilon_{1c}}{\varepsilon_{2c}} \tag{3.6b}$$

$$iii)\quad C_{22}^{H} = \frac{\sigma_2}{\varepsilon_{2c}} \tag{3.6c}$$

$$iv)\quad C_{66}^{H} = \frac{\sigma_6}{\varepsilon_{6c}} \tag{3.6d}$$

Substituting C_{ij}^{H} into (3.1a)-(3.1d) yields the homogenized material stiffness coefficients of the cracked ply.

Additionally, the effective elastic moduli and Poisson's ratio of the cracked material can be extracted from the homogenized material stiffness coefficients of the associated ply as

$$E_1^{D} = \frac{C_{11}^{D}C_{22}^{D} - \left(C_{12}^{D}\right)^2}{C_{22}^{D}} \tag{3.7a}$$

$$E_2^D = \frac{C_{11}^D C_{22}^D - \left(C_{12}^D\right)^2}{C_{11}^D} \tag{3.7b}$$

$$G_{12}^D = C_{66}^D \tag{3.7c}$$

$$\nu_{12}^D = \frac{C_{12}^D}{C_{22}^D} \tag{3.7d}$$

where the superscript D denotes the damaged ply and the subscripts are not referring to the laminate structure's direction but referring to the material direction of the transformed composite layer.

3.1.2 Damage Implementation on Bending Beam in Macroscale

Once the relation between the normalized crack density and the material stiffness coefficients is obtained, the homogenized material stiffness coefficients of the cracked ply for a given damage state can be used for the damaged beam bending analysis. Identifying the stiffness reduction of the cracked ply enables the effect of transverse cracks to be included in the bending analysis of the laminated composite beam. An assumption is made to simplify the problem in the macroscale beam bending analysis: a beam element that reaches a critical strain value is assumed to be fully cracked over the entire element with a certain normalized crack density D. Therefore, the material properties of the element showing the critical strain will be replaced by the homogenized values of the cracked ply which has been prepared in the mesoscale analysis.

3.2 Numerical Results and Discussion

A finite element model composed of membrane elements has been used to identify C_{ij}^{H} in [22, 23]. In the present study, the layer-wise laminated beam model will be applied by taking advantage of the excellent accuracy of the solutions from LWT, as shown in the previous section. As demonstrated in the previous section, the layer-wise laminated beam model is completely suitable for a mesoscale unit cell model with a small length-to-thickness ratio as well as the macroscale beam structure with a large length-to-thickness ratio.

Two finite element models using the layer-wise laminated beam theory are depicted in Fig. 3.1. The model (a) of Fig. 3.1 is the numerical unit cell in the mesoscale and the model (b) of Fig. 3.1 is the homogenized laminated beam in the macroscale which will be utilized to analyze the bending behavior of the damaged beam. Naturally, two steps of numerical simulations are carried out according to the view of multi-scale approach. At the first step of numerical simulation, a set of boundary conditions in equation (3.5a)-(3.5d) are imposed on the mesoscale unit cell model (a) of Fig. 3.1 to compute the stresses and eventually C_{ij}^{H} are determined. Once C_{ij}^{H} are known, the cracked ply's reduced material stiffness coefficients are computed from equation (3.1a)-(3.1d). The second numerical computation step to analyze the bending behavior of the damaged beam is performed with the macroscale beam model (b) of Fig. 3.1 by replacing the material properties of the cracked plies with the homogenized values C_{ij}^{c} which are given in the first numerical simulation step.

3.2.1 Mesoscale Analysis

The reduced material stiffness coefficients of a unit cell are computed for the same graphite/epoxy composite as chosen in the former section but the laminate consists of $[90/0]_s$ lay-up. The half part of the unit cell is modeled with eight quadratic beam elements using symmetric boundary conditions and each physical layer of the unit cell is interpolated by two quadratic Lagrange interpolation functions through the thickness. The lengths of the beam elements are gradually refined in the region which is close to the crack. Following the procedure explained with equations (18) through (20), the homogenized material stiffness coefficients of the total laminate for the same laminate configuration is obtained and plotted in Fig. 3.2. It is noted in this fig. that the ratio of the homogenized material stiffness coefficient to the virgin material stiffness coefficient of the total laminate gets smaller as the crack density is larger.

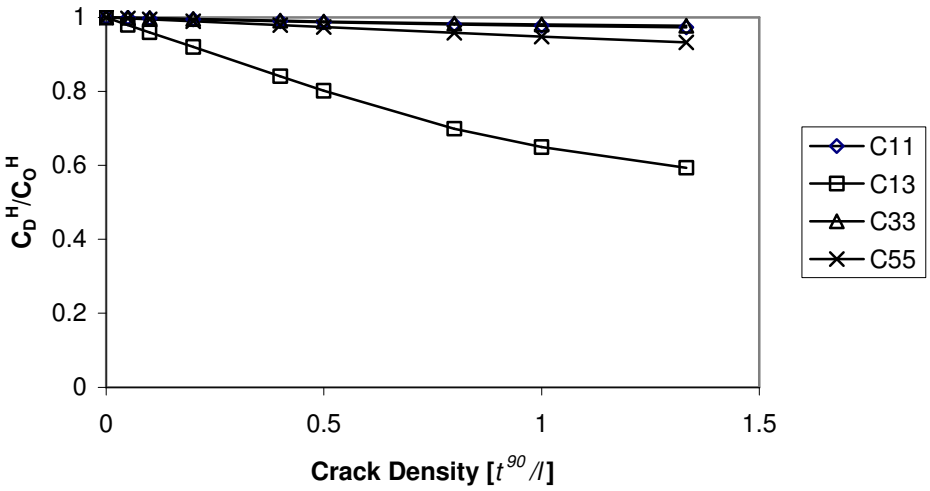

Fig. 3.2. Homogenized material stiffness coefficients of the total $[90/0]_s$ laminate

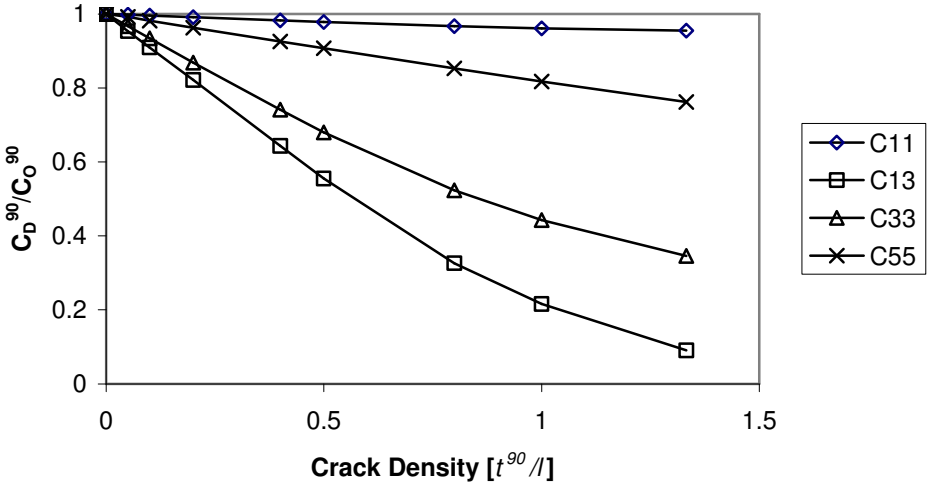

Fig. 3.3. Homogenized material stiffness coefficients of the cracked (90°) ply in $[90/0]_s$ laminate

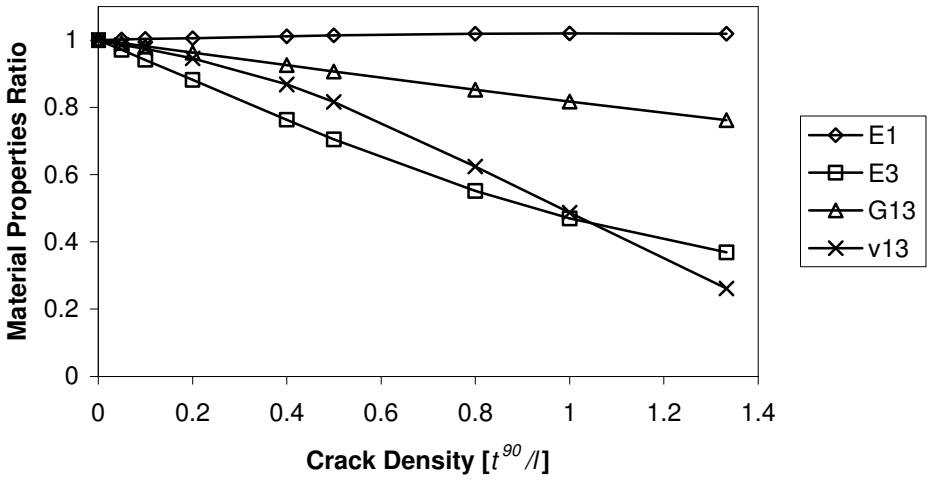

Fig. 3.4. Elastic moduli and Poisson's ratio reduction of the cracked ply in $[90/0]_s$ laminate

The homogenized material stiffness coefficients of the cracked (90°) ply are computed by making use of equation (16) from the homogenized material stiffness coefficients of the total laminate. Fig. 3.3 displays the decrease of material stiffness coefficients in the cracked ply with increasing the crack density. Note that the material direction of the 90° ply is marked in the graph so that C_{22}^D indicates the stiffness coefficient in the direction that is parallel to the fiber direction of the 0° ply.

The effective engineering constants, that is, Young's moduli (E_1^D, E_2^D), shear modulus (G_{12}^D), and Poisson's ratio (ν_{12}^D) of the cracked ply are shown in Fig. 3.4. It is worth pointing that the effective Young's modulus in the axial direction E_1^D of the 90° ply changes very little whereas the modulus in the transverse direction E_2^D is reduced drastically as the crack density increases. This result matches the observation reported in the literature that the presence of transverse cracks does not affect the effective Young's modulus along the fibers in the cracked lamina [66].

3.2.2 Macroscale Analysis

Having the effective elastic moduli and Poisson's ratio of the cracked lamina facilitates the analysis on the bending behavior of transversely cracked laminated beams. Here, the laminated beam is a macroscale structure and the effect of cracks in the individual lamina is treated as homogenized material characteristics in the cracked lamina. Again, the laminated beam is modeled with the finite elements developed from LWT. Fig. 3.5 presents the configuration of the clamped-clamped boundary conditions and the load

applied to the laminated beam. The clamped boundary conditions at both ends of the beam are chosen so that the effect of nonlinearity in LWT can be prominent. Since the geometric symmetry of the beam is obvious, one half of the full length of beam is modeled using symmetry boundary condition at $x = L/2$. Total 50 linear elements along the beam length and 4 quadratic interpolation functions through the thickness are used. The uniformly distributed load q_0 is applied and a constant load increment Δq is added at every load step until the uniformly distributed load reaches q_1 so that the composite laminated beam will carry increasingly varying loads and the transverse cracks will start forming in the 90° lamina. The critical load of forming the transverse cracks is determined by the critical axial normal stress at which the composite material fails. When the maximum stress in a 90° lamina reaches the critical stress, the material stiffness coefficients of the lamina in the associate finite element is replaced with the homogenized damaged material stiffness coefficients. The length of a single finite element is chosen such that the normalized crack density equals one, which is assumed to be a crack saturation state. That is, the 90° lamina in an element of which the maximum stress gets to the critical stress is considered as the fully cracked material and thus, no more transverse cracks can form in the same lamina of the same element.

The sequential progress of cracked finite element according to increasing load is depicted in Fig. 3.6. The area filled with black color represents the cracked element in the lamina. The first crack appears at the clamped end and the cracked elements are multiplied from the clamped end to the center of the beam. Then, the cracks near the center of the beam start developing and they progressed toward the clamped end.

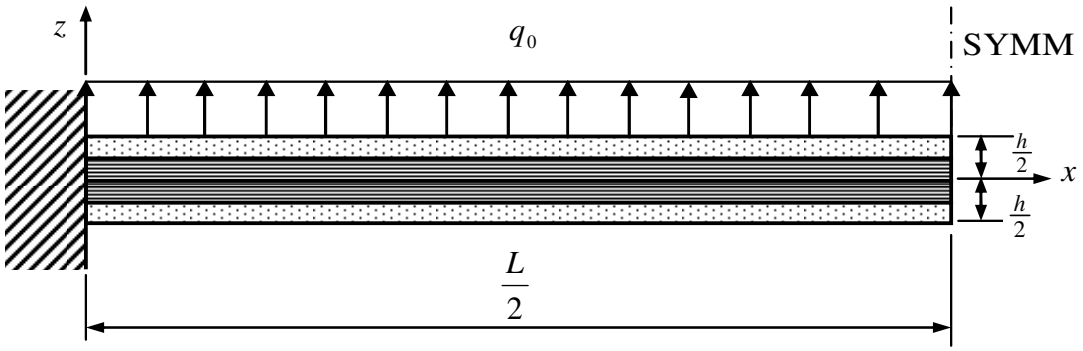

Fig. 3.5. Macroscale $[90/0]_s$ laminated beam model under a uniformly distributed load with clamped-clamped boundary conditions using geometric symmetry

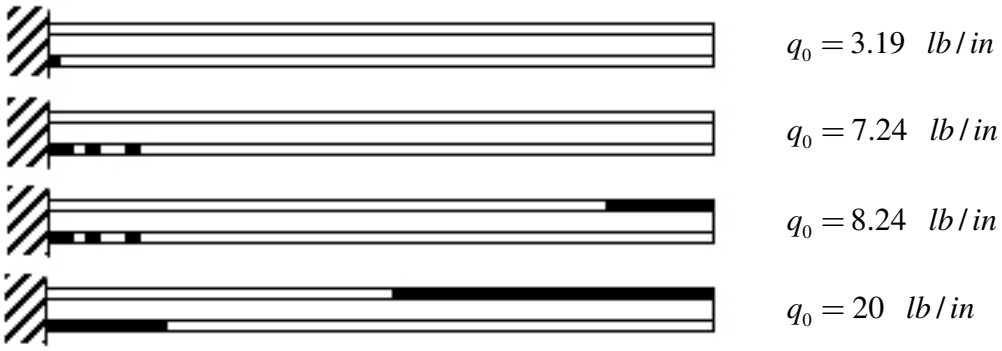

Fig. 3.6. The multiplication of cracks in a clamped-clamped $[90/0]_s$ laminated beam subjected to a uniformly distributed load

The maximum transverse deflection at the top surface of the center of the beam is plotted at each load step in Fig. 3.7 and Fig. 3.8 presents deformed shapes of the laminated beam under bending when the load $q_0 = 20\,(\text{lb/in})$ where many elements in the model have damaged. The damaged bending beams show larger transverse deflections as expected. It can be also seen that the effect of transverse cracks in the 90° ply is more prominent for the linear beam than the nonlinear case.

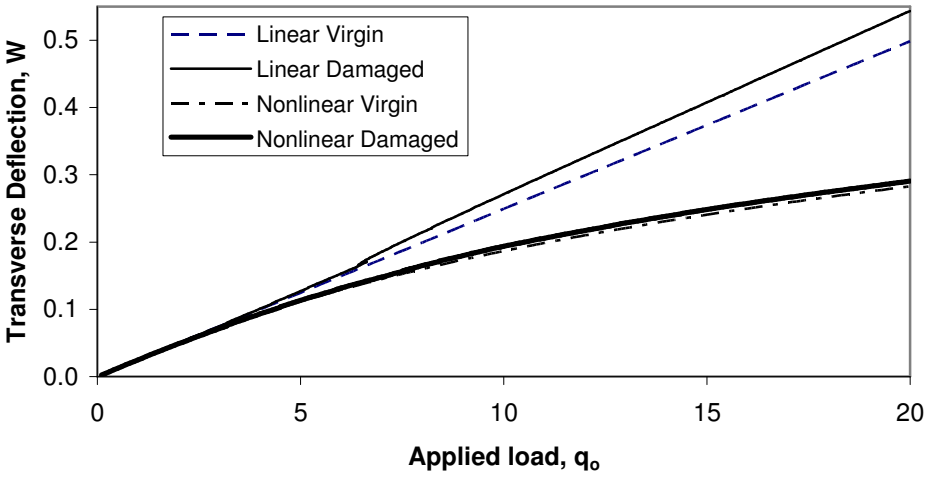

Fig. 3.7. Transverse deflection $w(\frac{L}{2},\frac{h}{2})$ versus the applied load of a clamped-clamped $[90/0]_s$ laminated beam

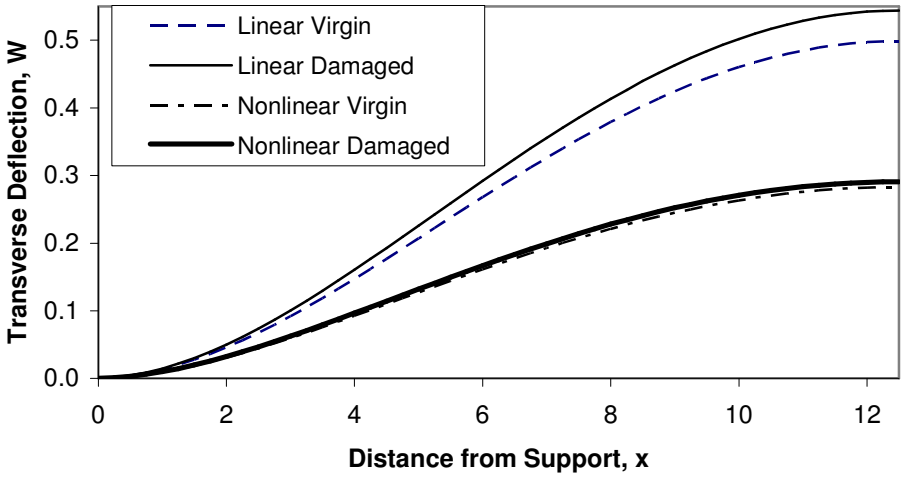

Fig. 3.8. Transverse deflection $w(x,\frac{h}{2})$ under $q_o = 4$ (lb/in) along the length of a clamped-clamped $[90/0]_s$ laminated beam

However, the nonlinear curve diverges from the linear curve before the linear beam is damaged, which implies that the nonlinearity develops before the cracks start forming in the bending beam. In this case, the bending beam analysis based on linear strain fields can result in an erroneous damage prediction, and thus the nonlinear beam model is required to take this account.

The axial normal stress σ_{xx} on the tensile surface is plotted in Fig. 3.9 and Fig. 3.10. As shown in Fig. 3.8, the bottom 90° layer near the clamped end is expected to be damaged due to the tensile stress under bending and the top 90° layer near the center of the beam is expected to crack. Thus, the stresses are computed at the nearest Gauss point to the bottom surface ($z = -h/2$) of the clamped end ($x = 0$) in Fig. 3.9 and the top

surface ($z = h/2$) of the center of beam ($x = L/2$) in Fig. 3.10. In this figure, the capacity to carry the axial load in the damaged lamina can be shown and the damage seems to diminish it radically. According to these figures, the initial crack is found at the clamped end first and the center of the beam is damaged later. The initial crack at the clamped end is formed at a relatively low applied load ($q_o = 3.16$ for linear beam and $q_o = 3.19$ for nonlinear beam) and the linear and the nonlinear beam show almost same stress change at this moment because the crack starts forming before the nonlinearity appears in the bending beam (Fig. 3.9).

On the other hand, it can be appreciated from Fig. 3.10 that the nonlinear beam sustains a higher applied load before the cracks are formed at the center of the laminated beam. Another interesting finding is that the second stress drop is observed in Fig. 3.9 at the same applied load of forming cracks at the center of the beam. On the contrary, no stress drop is found in Fig. 3.10 when the clamped boundary end is damaged. Only one big stress drop is found commonly in the linear and the nonlinear beam when the center of the beam itself is damaged. One can draw a conclusion from this observation that the damage around the clamped boundary area has little influence on the stress field of the center of the beam in an experiment on damaged laminated beam under bending.

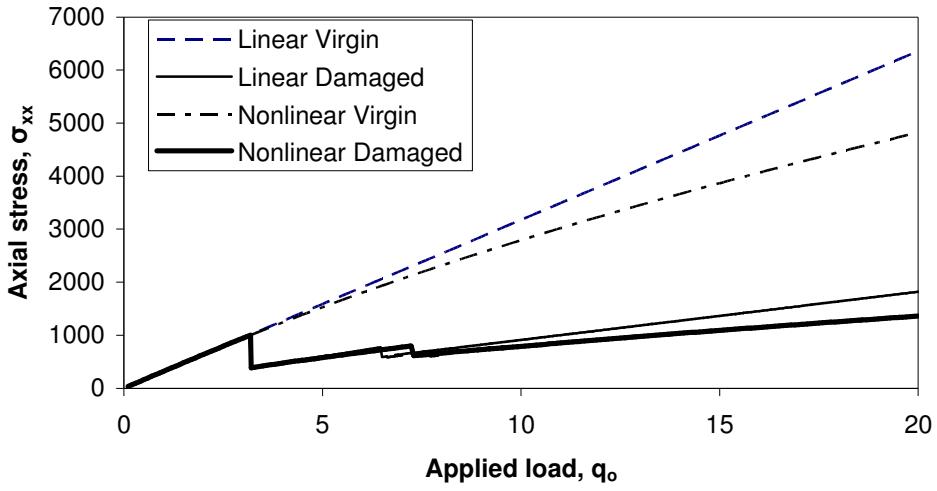

Fig. 3.9. Axial stress at the clamped end $\sigma_{xx}(0,-\frac{h}{2})$ versus the applied load in a clamped-clamped $[90/0]_s$ laminated beam

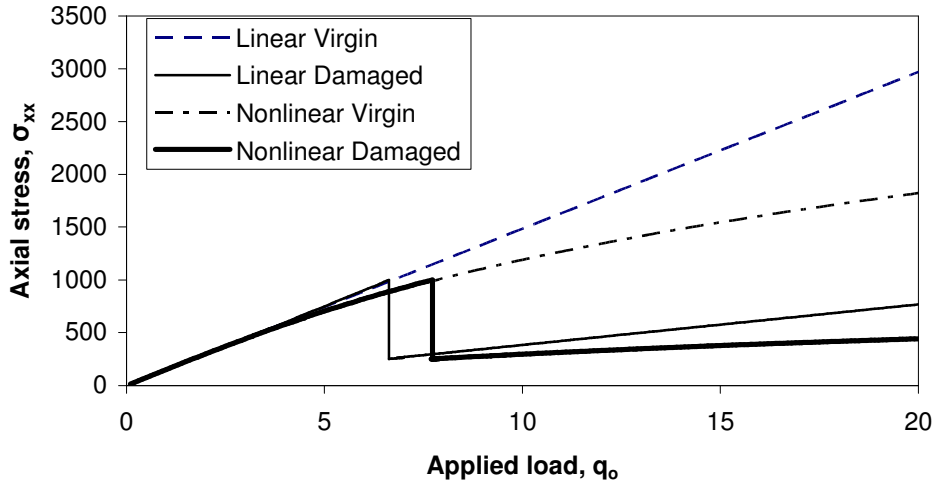

Fig. 3.10. Axial stress at the center of the beam $\sigma_{xx}(\frac{L}{2},\frac{h}{2})$ versus the applied load in a clamped-clamped $[90/0]_s$ laminated beam

Figs. 3.11 through 3.13 show the stress distributions through the thickness of the laminate near the center of the beam under the applied load $q_o = 20$ (lb/in). In Fig. 3.11, the axial normal stress is reduced through the thickness when the damage is considered in the laminated beam. The damaged 90° ply shows little capacity to carry the axial load. More importantly, the neutral axis, at which the axial normal stress $\sigma_{xx} = 0$, lies departing from $z = 0$ axis for the nonlinear beam case whereas the linear beam shows a symmetric stress distribution about $z = 0$ axis.

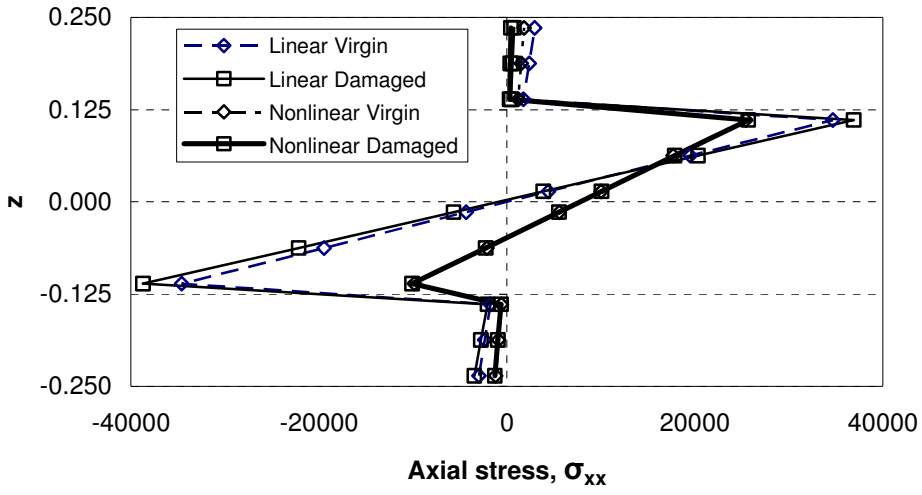

Fig. 3.11. Axial stress distribution $\sigma_{xx}(\frac{L}{2}, z)$ through the thickness of a clamped-clamped $[90/0]_s$ laminated beam

Considering that the cracking starts after the kinematic nonlinearity develops, the nonlinear beam model is suitable for this problem because its capability to capture the

shift of neutral axis to the compressive side under a large deformation appears to give more practical solutions.

Fig. 3.12 displays the transverse normal stress distribution through the thickness The bending beam shows a large compressive stress in the 90° plies when the damage is taken into account although the stress change in the core (0° plies) of the laminate is not noticeable.

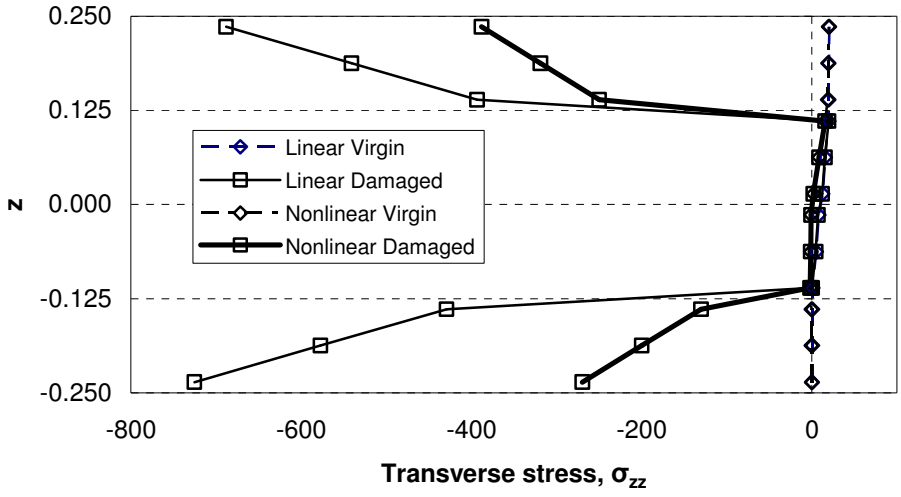

Fig. 3.12. Transverse stress distribution $\sigma_{zz}(\frac{L}{2}, z)$ through the thickness of a clamped-clamped $[90/0]_s$ laminated beam

The shear stress distribution through the thickness is shown in Fig. 3.13. The significant change of shear stress at the center of the beam is not found when the effect of damage is imposed in the clamped-clamped model.

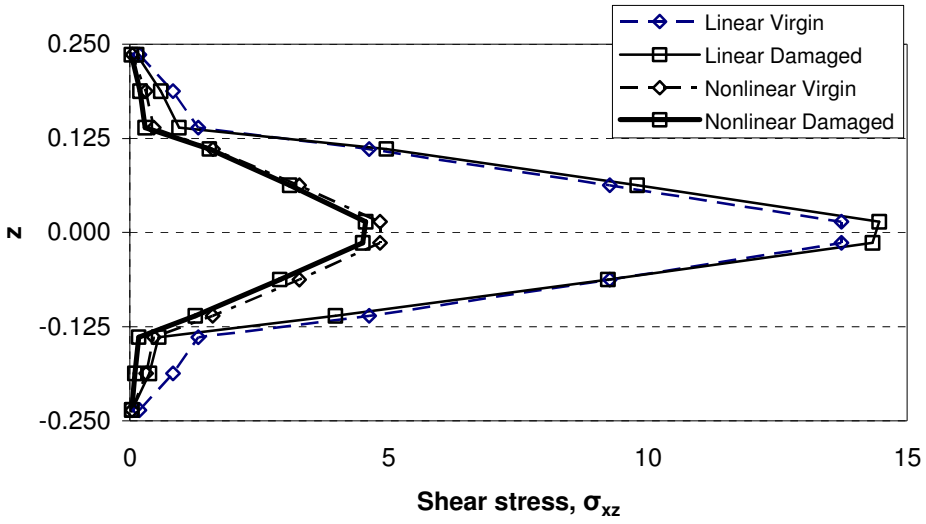

Fig. 3.13. Shear stress distribution $\sigma_{xz}(\frac{L}{2}, z)$ through the thickness of a clamped-clamped $[90/0]_s$ laminated beam

CHAPTER IV

DELAMINATION ANALYSIS USING THE LAYER-WISE THEORY

4.1. Outline

A beam model using layer-wise theory was formulated and implemented in a finite element model to analyze delamination phenomena in laminated composite beams. The Heaviside step function was adopted to express the discontinuous interlaminar displacement field of the delaminated layer. To verify the solutions obtained from the numerical analysis, a benchmark test was performed by comparing with the solutions available in the literature.

4.2. Formulation

4.2.1 Layer-wise Theory with Heaviside Step Function

The total displacement fields of the laminated beam are assumed to be written as

$$u(x,z) = u^{LWT}(x,z) + u^{DEL}(x,z) \tag{4.1a}$$

$$v(x,z) = 0 \tag{4.1b}$$

$$w(x,z) = w^{LWT}(x,z) + w^{DEL}(x,z) \tag{4.1c}$$

where u^{LWT} and w^{LWT} are the longitudinal and the transverse displacement fields using the layer-wise theory expressed as

$$u^{LWT}(x,z)=\sum_{I=1}^{N}U_I(x)\Phi^I(z) \tag{4.2a}$$

$$w^{LWT}(x,z)=\sum_{I=1}^{M}W_I(x)\Psi^I(z)\,. \tag{4.2b}$$

In equations (4.2a)-(4.2b), Φ^I and Ψ^I are generally different 1-D Lagrangian polynomials with C^0 continuity across the layers so that the strain field through the thickness can be discontinuous and that, in turn, the stress field can have the possibility to be continuous.

On the other hand, u^{DEL} and w^{DEL} in equations (4.1a) and (4.1c) denote the discontinuous longitudinal and transverse displacement due to delamination, respectively, which can be expressed as

$$u^{DEL}(x,z)=\sum_{I=1}^{ND}{}^{D}U_I(x)H^I(z) \tag{4.3a}$$

$$w^{DEL}(x,z)=\sum_{I=1}^{ND}{}^{D}W_I(x)H^I(z) \tag{4.3b}$$

where ND indicates the number of delaminated interfaces and $H^I(z)$ is defined using the Heaviside step function such that

$$H^I(z)=\hat{H}^I(z-z_\mu)=\begin{cases}1 & , \quad z\geq z_\mu \\ 0 & , \quad z<z_\mu\end{cases}. \tag{4.4}$$

It should be noted that the *I*th nodal values of (u, w) are the combination of (U_I, W_I) and $({}^{D}U_I, {}^{D}W_I)$.

To accommodate moderately large deformations, the von Kármán type nonlinear strains are employed as follows

$$\varepsilon_{xx} = \frac{\partial u}{\partial x} + \frac{1}{2}\left(\frac{\partial w}{\partial x}\right)^2$$

$$= \sum_{I=1}^{N} \frac{dU_I(x)}{dx}\Phi^I(z) + \sum_{I=1}^{ND} \frac{d\,{}^{D}U_I(x)}{dx} H^I(z)$$

$$+ \frac{1}{2}\left(\sum_{I=1}^{M} \frac{dW_I(x)}{dx}\Psi^I(z) + \sum_{I=1}^{ND} \frac{d\,{}^{D}W_I(x)}{dx} H^I(z)\right)$$

$$\times\left(\sum_{J=1}^{M} \frac{dW_J(x)}{dx}\Psi^J(z) + \sum_{J=1}^{ND} \frac{d\,{}^{D}W_J(x)}{dx} H^J(z)\right) \tag{4.5a}$$

$$\varepsilon_{zz} = \frac{\partial w}{\partial z} = \sum_{I=1}^{M} W_I(x)\frac{d\Psi^I(z)}{dz} \tag{4.5b}$$

$$\gamma_{xz} = \frac{\partial w}{\partial x} + \frac{\partial u}{\partial z}$$

$$= \sum_{I=1}^{M} \frac{dW_I(x)}{dx}\Psi^I(z) + \sum_{I=1}^{N} U_I(x)\frac{d\Phi^I(z)}{dx} + \sum_{I=1}^{ND} \frac{d\,{}^{D}W_I(x)}{dx} H^I(z) \tag{4.5c}$$

$$\varepsilon_{yy} = \gamma_{xy} = \gamma_{yz} = 0. \tag{4.5d}$$

For the *k*th orthotropic lamina, the reduced stresses can be obtained from the plane strain using the following constitutive equations,

$$\begin{Bmatrix} \sigma_{xx} \\ \sigma_{zz} \\ \sigma_{xz} \end{Bmatrix}^{(k)} = \begin{bmatrix} \overline{C}_{11} & \overline{C}_{13} & 0 \\ \overline{C}_{31} & \overline{C}_{33} & 0 \\ 0 & 0 & \overline{C}_{55} \end{bmatrix}^{(k)} \begin{Bmatrix} \varepsilon_{xx} \\ \varepsilon_{zz} \\ \gamma_{xz} \end{Bmatrix}^{(k)} \tag{4.6}$$

where $\overline{C}_{ij}^{(k)}$ are the transformed elastic coefficients of which are symmetric for orthotropic materials.

The governing equations of the layer-wise beam depicted in Fig. 2.1 are derived from the principle of virtual displacements,

$$0 = \delta U + \delta V \tag{4.7}$$

where the virtual strain energy δU and the virtual work done δV are given by

$$\delta U = \int_{x_a}^{x_b} \int_{-\frac{h}{2}}^{\frac{h}{2}} \left(\sigma_{xx} \delta \varepsilon_{xx} + \sigma_{zz} \delta \varepsilon_{zz} + \sigma_{xz} \delta \gamma_{xz} \right) dz dx \tag{4.8a}$$

$$\delta V = -\int_{x_a}^{x_b} \left(f_b(x) \delta u(x, -\tfrac{h}{2}) + f_t(x) \delta u(x, \tfrac{h}{2}) \right) dx$$

$$- \int_{x_a}^{x_b} \left(q_b(x) \delta w(x, -\tfrac{h}{2}) + q_t(x) \delta w(x, \tfrac{h}{2}) \right) dx . \tag{4.8b}$$

Applying the stress-strain relations in equation (4.6) and strain-displacement relations in equations (4.5) to (4.8a) and (4.8b), the virtual energy and the virtual work done can be described in terms of the nodal displacements as follows

$$\delta U = \int_{x_a}^{x_b} \left[\sum_{I=1}^{N} \left(N_{xx}^{I} \frac{d\delta U_I}{dx} + Q_x^I \delta U_I \right) + \sum_{I=1}^{N} \left(\sum_{J=1}^{M} N_{xx}^{IJ} \frac{d\delta W_I}{dx} \frac{dW_J}{dx} + Q_z^I \delta W_I + \tilde{Q}_x^I \frac{d\delta W_I}{dx} \right) \right.$$

$$+ \int_{x_a}^{x_b} \sum_{I=1}^{M} \sum_{J=1}^{ND} {}^{D}N_{xx}^{IJ} \frac{d\delta W_I}{dx} \frac{d\,{}^{D}W_J}{dx} dx$$

$$+ \int_{x_a}^{x_b} \sum_{I=1}^{ND} \left(\sum_{J=1}^{M} {}^{D}N_{xx}^{JI} \frac{d\delta\,{}^{D}W_I}{dx} \frac{dW_J}{dx} + \sum_{J=1}^{ND} {}^{D}\hat{N}_{xx}^{IJ} \frac{d\delta\,{}^{D}W_I}{dx} \frac{d\,{}^{D}W_J}{dx} \right) dx$$

$$\left. + \int_{x_a}^{x_b} \left(\sum_{I=1}^{ND} {}^{D}N_{xx}^{I} \frac{d\delta\,{}^{D}U_I}{dx} + \sum_{I=1}^{ND} {}^{D}Q_x^I \frac{d\delta\,{}^{D}W_I}{dx} \right) dx \right. \tag{4.9a}$$

$$\delta V = -\int_{x_a}^{x_b} \left(f_b \delta U_1 + f_t \delta U_N \right) dx - \int_{x_a}^{x_b} \left(q_b \delta W_1 + q_t \delta W_M \right) dx \tag{4.9b}$$

where

$$N_{xx}^{I} = \sum_{J=1}^{N} A_{11}^{IJ} \frac{dU_J}{dx} + \frac{1}{2} \sum_{J=1}^{M} \sum_{K=1}^{M} B_{11}^{IJK} \frac{dW_J}{dx} \frac{dW_K}{dx} + \sum_{J=1}^{M} \tilde{A}_{13}^{IJ} W_J + \sum_{J=1}^{ND} {}^{D}A_{11}^{IJ} \frac{d\,{}^{D}U_J}{dx}$$

$$+ \sum_{J=1}^{M} \sum_{K=1}^{ND} {}^{D}B_{11}^{IJK} \frac{dW_J}{dx} \frac{d\,{}^{D}W_K}{dx} + \frac{1}{2} \sum_{J=1}^{ND} \sum_{K=1}^{ND} {}^{D}\bar{B}_{11}^{IJK} \frac{d\,{}^{D}W_J}{dx} \frac{d\,{}^{D}W_K}{dx} \tag{4.10a}$$

$$N_{xx}^{IJ} = \sum_{K=1}^{N} B_{11}^{KIJ} \frac{dU_K}{dx} + \frac{1}{2} \sum_{K=1}^{M} \sum_{L=1}^{M} D_{11}^{IJKL} \frac{dW_K}{dx} \frac{dW_L}{dx} + \sum_{K=1}^{M} \tilde{B}_{13}^{IJK} W_K + \sum_{K=1}^{ND} {}^{D}\hat{B}_{11}^{IJK} \frac{d\,{}^{D}U_K}{dx}$$

$$+\sum_{K=1}^{M}\sum_{L=1}^{ND} {}^{D}D_{11}^{IJKL}\frac{dW_K}{dx}\frac{d\,{}^{D}W_L}{dx}+\frac{1}{2}\sum_{K=1}^{ND}\sum_{L=1}^{ND} {}^{D}\bar{D}_{11}^{IJKL}\frac{d\,{}^{D}W_K}{dx}\frac{d\,{}^{D}W_L}{dx} \tag{4.10b}$$

$${}^{D}N_{xx}^{I}=\sum_{J=1}^{N} {}^{D}A_{11}^{JI}\frac{dU_J}{dx}+\frac{1}{2}\sum_{J=1}^{M}\sum_{K=1}^{M} {}^{D}\hat{B}_{11}^{JKI}\frac{dW_J}{dx}\frac{dW_K}{dx}+\sum_{J=1}^{M} {}^{D}\tilde{A}_{13}^{IJ}W_J+\sum_{J=1}^{ND} {}^{D}\bar{\bar{A}}_{11}^{IJ}\frac{d\,{}^{D}U_J}{dx}$$

$$+\sum_{J=1}^{M}\sum_{K=1}^{ND} {}^{D}\hat{\hat{B}}_{11}^{JIK}\frac{dW_J}{dx}\frac{d\,{}^{D}W_K}{dx}+\frac{1}{2}\sum_{J=1}^{ND}\sum_{K=1}^{ND} {}^{D}\bar{\bar{B}}_{11}^{IJK}\frac{d\,{}^{D}W_J}{dx}\frac{d\,{}^{D}W_K}{dx} \tag{4.10c}$$

$${}^{D}N_{xx}^{IJ}=\sum_{K=1}^{N} {}^{D}B_{11}^{KIJ}\frac{dU_K}{dx}+\frac{1}{2}\sum_{K=1}^{M}\sum_{L=1}^{M} {}^{D}D_{11}^{IKLJ}\frac{dW_K}{dx}\frac{dW_L}{dx}+\sum_{K=1}^{M} {}^{D}\tilde{B}_{13}^{IJK}W_K+\sum_{K=1}^{ND} {}^{D}\hat{\hat{B}}_{11}^{IJK}\frac{d\,{}^{D}U_K}{dx}$$

$$+\sum_{K=1}^{M}\sum_{L=1}^{ND} {}^{D}\bar{D}_{11}^{IKJL}\frac{dW_K}{dx}\frac{d\,{}^{D}W_L}{dx}+\frac{1}{2}\sum_{K=1}^{ND}\sum_{L=1}^{ND} {}^{D}\bar{\bar{D}}_{11}^{IJKL}\frac{d\,{}^{D}W_K}{dx}\frac{d\,{}^{D}W_L}{dx} \tag{4.10d}$$

$${}^{D}\hat{N}_{xx}^{IJ}=\sum_{K=1}^{N} {}^{D}\bar{B}_{11}^{KIJ}\frac{dU_K}{dx}+\frac{1}{2}\sum_{K=1}^{M}\sum_{L=1}^{M} {}^{D}\bar{D}_{11}^{KLIJ}\frac{dW_K}{dx}\frac{dW_L}{dx}+\sum_{K=1}^{M} {}^{D}\tilde{\tilde{B}}_{13}^{IJK}W_K+\sum_{K=1}^{ND} {}^{D}\bar{\bar{B}}_{11}^{IJK}\frac{d\,{}^{D}U_K}{dx}$$

$$+\sum_{K=1}^{M}\sum_{L=1}^{ND} {}^{D}\bar{\bar{D}}_{11}^{KIJL}\frac{dW_K}{dx}\frac{d\,{}^{D}W_L}{dx}+\frac{1}{2}\sum_{K=1}^{ND}\sum_{L=1}^{ND} {}^{D}\bar{\bar{D}}_{11}^{IJKL}\frac{d\,{}^{D}W_K}{dx}\frac{d\,{}^{D}W_L}{dx} \tag{4.10e}$$

$$Q_x^I=\sum_{J=1}^{N}\bar{A}_{55}^{IJ}U_J+\sum_{J=1}^{M}\bar{B}_{55}^{IJ}\frac{dW_J}{dx}+\sum_{J=1}^{ND} {}^{D}\bar{B}_{55}^{IJ}\frac{d\,{}^{D}W_J}{dx} \tag{4.10f}$$

$$\tilde{Q}_x^I=\sum_{J=1}^{N}\bar{B}_{55}^{JI}U_J+\sum_{J=1}^{M}\bar{D}_{55}^{IJ}\frac{dW_J}{dx}+\sum_{J=1}^{ND} {}^{D}\bar{A}_{55}^{IJ}\frac{d\,{}^{D}W_J}{dx} \tag{4.10g}$$

$$Q_z^I=\sum_{J=1}^{N}\tilde{A}_{31}^{JI}\frac{dU_J}{dx}+\frac{1}{2}\sum_{J=1}^{M}\sum_{K=1}^{M}\tilde{B}_{31}^{JKI}\frac{dW_J}{dx}\frac{dW_K}{dx}+\sum_{J=1}^{M}\hat{A}_{33}^{IJ}W_J+\sum_{J=1}^{ND} {}^{D}\tilde{A}_{31}^{JI}\frac{d\,{}^{D}U_J}{dx}$$

$$+\sum_{J=1}^{M}\sum_{K=1}^{ND} {}^{D}\tilde{B}_{31}^{JKI}\frac{dW_J}{dx}\frac{d\,{}^{D}W_K}{dx}+\frac{1}{2}\sum_{J=1}^{ND}\sum_{K=1}^{ND} {}^{D}\tilde{\tilde{B}}_{31}^{JKI}\frac{d\,{}^{D}W_J}{dx}\frac{d\,{}^{D}W_K}{dx} \tag{4.10h}$$

$${}^{D}Q_x^I=\sum_{J=1}^{N} {}^{D}\bar{B}_{55}^{JI}U_J+\sum_{J=1}^{M} {}^{D}\bar{A}_{55}^{JI}\frac{dW_J}{dx}+\sum_{J=1}^{ND} {}^{D}\bar{\bar{A}}_{55}^{IJ}\frac{d\,{}^{D}W_J}{dx} \tag{4.10i}$$

and

$$A_{ij}^{IJ} = \sum_{k=1}^{Ne} \int_{z_k}^{z_{k+1}} \overline{C}_{ij}^{(k)} \Phi^I \Phi^J dz \tag{4.11a}$$

$$\tilde{A}_{ij}^{IJ} = \sum_{k=1}^{Ne} \int_{z_k}^{z_{k+1}} \overline{C}_{ij}^{(k)} \Phi^I \frac{d\Psi^J}{dz} dz \tag{4.11b}$$

$$\overline{A}_{ij}^{IJ} = \sum_{k=1}^{Ne} \int_{z_k}^{z_{k+1}} \overline{C}_{ij}^{(k)} \frac{d\Phi^I}{dz} \frac{d\Phi^J}{dz} dz \tag{4.11c}$$

$$\hat{A}_{ij}^{IJ} = \sum_{k=1}^{Ne} \int_{z_k}^{z_{k+1}} \overline{C}_{ij}^{(k)} \frac{d\Psi^I}{dz} \frac{d\Psi^J}{dz} dz \tag{4.11d}$$

$$\overline{B}_{ij}^{IJ} = \sum_{k=1}^{Ne} \int_{z_k}^{z_{k+1}} \overline{C}_{ij}^{(k)} \frac{d\Phi^I}{dz} \Psi^J dz \tag{4.11e}$$

$$\overline{D}_{ij}^{IJ} = \sum_{k=1}^{Ne} \int_{z_k}^{z_{k+1}} \overline{C}_{ij}^{(k)} \Psi^I \Psi^J dz \tag{4.11f}$$

$$B_{ij}^{IJK} = \sum_{k=1}^{Ne} \int_{z_k}^{z_{k+1}} \overline{C}_{ij}^{(k)} \Phi^I \Psi^J \Psi^K dz \tag{4.11g}$$

$$\tilde{B}_{ij}^{IJK} = \sum_{k=1}^{Ne} \int_{z_k}^{z_{k+1}} \overline{C}_{ij}^{(k)} \Psi^I \Psi^J \frac{d\Psi^K}{dz} dz \tag{4.11h}$$

$$D_{ij}^{IJKL} = \sum_{k=1}^{Ne} \int_{z_k}^{z_{k+1}} \overline{C}_{ij}^{(k)} \Psi^I \Psi^J \Psi^K \Psi^L dz \tag{4.11i}$$

$${}^{D}A_{ij}^{IJ} = \sum_{k=1}^{Ne} \int_{z_k}^{z_{k+1}} \overline{C}_{ij}^{(k)} \Phi^I H^J dz \tag{4.11j}$$

$${}^{D}\overline{A}_{ij}^{IJ} = \sum_{k=1}^{Ne} \int_{z_k}^{z_{k+1}} \overline{C}_{ij}^{(k)} \Psi^I H^J dz \tag{4.11k}$$

$$ {}^{D}\tilde{A}_{ij}^{IJ} = \sum_{k=1}^{Ne} \int_{z_k}^{z_{k+1}} \bar{C}_{ij}^{(k)} H^I \frac{d\Psi^J}{dz} dz \tag{4.11l} $$

$$ {}^{D}\bar{\bar{A}}_{ij}^{IJ} = \sum_{k=1}^{Ne} \int_{z_k}^{z_{k+1}} \bar{C}_{ij}^{(k)} H^I H^J dz \tag{4.11m} $$

$$ {}^{D}\bar{B}_{ij}^{IJ} = \sum_{k=1}^{Ne} \int_{z_k}^{z_{k+1}} \bar{C}_{ij}^{(k)} \frac{d\Phi^I}{dz} H^J dz \tag{4.11n} $$

$$ {}^{D}B_{ij}^{IJK} = \sum_{k=1}^{Ne} \int_{z_k}^{z_{k+1}} \bar{C}_{ij}^{(k)} \Phi^I \Psi^J H^K dz \tag{4.11o} $$

$$ {}^{D}\bar{B}_{ij}^{IJK} = \sum_{k=1}^{Ne} \int_{z_k}^{z_{k+1}} \bar{C}_{ij}^{(k)} \Phi^I H^J H^K dz \tag{4.11p} $$

$$ {}^{D}\bar{\bar{B}}_{ij}^{IJK} = \sum_{k=1}^{Ne} \int_{z_k}^{z_{k+1}} \bar{C}_{ij}^{(k)} H^I H^J H^K dz \tag{4.11q} $$

$$ {}^{D}\hat{B}_{ij}^{IJK} = \sum_{k=1}^{Ne} \int_{z_k}^{z_{k+1}} \bar{C}_{ij}^{(k)} \Psi^I \Psi^J H^K dz \tag{4.11r} $$

$$ {}^{D}\hat{\hat{B}}_{ij}^{IJK} = \sum_{k=1}^{Ne} \int_{z_k}^{z_{k+1}} \bar{C}_{ij}^{(k)} \Psi^I H^J H^K dz \tag{4.11s} $$

$$ {}^{D}\tilde{B}_{ij}^{IJK} = \sum_{k=1}^{Ne} \int_{z_k}^{z_{k+1}} \bar{C}_{ij}^{(k)} \Psi^I H^J \frac{d\Psi^K}{dz} dz \tag{4.11t} $$

$$ {}^{D}\tilde{\tilde{B}}_{ij}^{IJK} = \sum_{k=1}^{Ne} \int_{z_k}^{z_{k+1}} \bar{C}_{ij}^{(k)} H^I H^J \frac{d\Psi^K}{dz} dz \tag{4.11u} $$

$$ {}^{D}D_{ij}^{IJKL} = \sum_{k=1}^{Ne} \int_{z_k}^{z_{k+1}} \bar{C}_{ij}^{(k)} \Psi^I \Psi^J \Psi^K H^L dz \tag{4.11v} $$

$$ {}^{D}\bar{D}_{ij}^{IJKL} = \sum_{k=1}^{Ne} \int_{z_k}^{z_{k+1}} \bar{C}_{ij}^{(k)} \Psi^I \Psi^J H^K H^L dz \tag{4.11w} $$

$$ {}^{D}\bar{\bar{D}}_{ij}^{IJKL} = \sum_{k=1}^{Ne} \int_{z_k}^{z_{k+1}} \bar{C}_{ij}^{(k)} \Psi^I H^J H^K H^L dz \tag{4.11x} $$

$$ {}^{D}\overline{\overline{\overline{D}}}_{ij}^{IJKL} = \sum_{k=1}^{Ne} \int_{z_k}^{z_{k+1}} \overline{C}_{ij}^{(k)} H^I H^J H^K H^L dz \,. \tag{4.11y} $$

In euqtions (4.11a)-(4.11y), Ne is the number of physical layers in the laminate and the laminate stiffness coefficients with three or four superscripts are introduced due to the nonlinearity of von Kármán type strain. The superscript D in front of the laminate stiffness coefficients indicates the terms induced by delamination.

4.2.2 Finite Element Model

The displacement fields (4.2a)-(4.3b) are interpolated by appropriate approximation functions in order to represent a finite element model for a layer-wise beam as follows

$$ U_I(x) = \sum_{j=1}^{p} U_I^j \varphi_j^{(1)}(x) \tag{4.12a} $$

$$ W_I(x) = \sum_{j=1}^{q} W_I^j \varphi_j^{(2)}(x) \tag{4.12b} $$

$$ {}^{D}U_I(x) = \sum_{j=1}^{r} {}^{D}U_I^j \varphi_j^{(3)}(x) \tag{4.12c} $$

$$ {}^{D}W_I(x) = \sum_{j=1}^{s} {}^{D}W_I^j \varphi_j^{(4)}(x) \tag{4.12d} $$

where p and q are the number of nodes per 1-D element used to approximate the longitudinal and transverse deflections, respectively, and r and s are the number of

nodes per 1-D element used to approximate the discontinuous longitudinal and transverse deflections due to delamination, respectively. U_I^j, W_I^j, ${}^DU_I^j$ and ${}^DW_I^j$ are the displacement values at the *j*th node along the longitudinal (x) direction of *I*th beam element. The interpolation functions $\varphi_j^{(m)}$ are the 1-D Lagrangian polynomials with respect to the longitudinal and transverse deflections at the *j*th node of each beam element.

Substituting the approximated displacement fields (4.12a)-(4.12d) in the longitudinal direction and their variational forms into the energy equation (4.9a) and (4.9b) yields the finite element equations for an element as

$$\begin{bmatrix} [K^{(11)}] & [K^{(12)}] & [K^{(13)}] & [K^{(14)}] \\ [K^{(21)}] & [K^{(22)}] & [K^{(23)}] & [K^{(24)}] \\ [K^{(31)}] & [K^{(32)}] & [K^{(33)}] & [K^{(34)}] \\ [K^{(41)}] & [K^{(42)}] & [K^{(43)}] & [K^{(44)}] \end{bmatrix}^e \begin{Bmatrix} \{U\} \\ \{W\} \\ \{{}^DU\} \\ \{{}^DW\} \end{Bmatrix}^e = \begin{Bmatrix} \{{}^1F\} \\ \{{}^2F\} \\ \{0\} \\ \{0\} \end{Bmatrix}^e \tag{4.13}$$

where

$$K_{ij}^{(11)IJ} = \int_{x_a}^{x_b} \left(A_{11}^{IJ} \frac{d\varphi_i^{(1)}}{dx} \frac{d\varphi_j^{(1)}}{dx} + \bar{A}_{55}^{IJ} \varphi_i^{(1)} \varphi_j^{(1)} \right) dx \tag{4.14a}$$

$$K_{ij}^{(12)IJ} = \int_{x_a}^{x_b} \left[\frac{1}{2} \left(\sum_{K=1}^{M} B_{11}^{IJK} \frac{dW_K}{dx} \right) \frac{d\varphi_i^{(1)}}{dx} \frac{d\varphi_j^{(2)}}{dx} + \tilde{A}_{13}^{IJ} \frac{d\varphi_i^{(1)}}{dx} \varphi_j^{(2)} + \bar{B}_{55}^{IJ} \varphi_i^{(1)} \frac{d\varphi_j^{(2)}}{dx} \right] dx$$

$$+\int_{x_a}^{x_b}\left(\sum_{K=1}^{ND} {}^{D}B_{11}^{IJK}\,\frac{d\,{}^{D}W_K}{dx}\right)\frac{d\varphi_i^{(1)}}{dx}\frac{d\varphi_j^{(2)}}{dx}\,dx \tag{4.14b}$$

$$K_{ij}^{(13)IJ} = \int_{x_a}^{x_b} {}^{D}A_{11}^{IJ}\,\frac{d\varphi_i^{(1)}}{dx}\frac{d\varphi_j^{(3)}}{dx}\,dx \tag{4.14c}$$

$$K_{ij}^{(14)IJ} = \int_{x_a}^{x_b}\left[\frac{1}{2}\left(\sum_{K=1}^{ND} {}^{D}B_{11}^{IJK}\,\frac{d\,{}^{D}W_K}{dx}\right)\frac{d\varphi_i^{(1)}}{dx}\frac{d\varphi_j^{(4)}}{dx} + {}^{D}\overline{B}_{55}^{IJ}\varphi_i^{(1)}\,\frac{d\varphi_j^{(4)}}{dx}\right]dx \tag{4.14d}$$

$$K_{ij}^{(21)IJ} = \int_{x_a}^{x_b}\left[\left(\sum_{K=1}^{M} B_{11}^{JIK}\,\frac{dW_K}{dx}\right)\frac{d\varphi_i^{(2)}}{dx}\frac{d\varphi_j^{(1)}}{dx} + \tilde{A}_{31}^{JI}\varphi_i^{(2)}\,\frac{d\varphi_j^{(1)}}{dx} + \overline{B}_{55}^{JI}\,\frac{d\varphi_i^{(2)}}{dx}\varphi_j^{(1)}\right]dx$$

$$+\int_{x_a}^{x_b}\left(\sum_{K=1}^{ND} {}^{D}B_{11}^{JIK}\,\frac{d\,{}^{D}W_K}{dx}\right)\frac{d\varphi_i^{(2)}}{dx}\frac{d\varphi_j^{(1)}}{dx}\,dx \tag{4.14e}$$

$$K_{ij}^{(22)IJ} = \int_{x_a}^{x_b}\left[\frac{1}{2}\left(\sum_{K=1}^{M}\sum_{L=1}^{M} D_{11}^{IJKL}\,\frac{dW_K}{dx}\frac{dW_L}{dx}\right)\frac{d\varphi_i^{(2)}}{dx}\frac{d\varphi_j^{(2)}}{dx}\right]dx$$

$$+\int_{x_a}^{x_b}\left[\left(\sum_{K=1}^{M}\tilde{B}_{13}^{IKJ}\,\frac{dW_K}{dx}\right)\frac{d\varphi_i^{(2)}}{dx}\varphi_j^{(2)}dx + \frac{1}{2}\left(\sum_{K=1}^{M}\tilde{B}_{31}^{JKI}\,\frac{dW_K}{dx}\right)\varphi_i^{(2)}\,\frac{d\varphi_j^{(2)}}{dx}\right]dx$$

$$+\int_{x_a}^{x_b}\left[\hat{A}_{33}^{IJ}\varphi_i^{(2)}\varphi_j^{(2)} + \overline{D}_{55}^{IJ}\,\frac{d\varphi_i^{(2)}}{dx}\frac{d\varphi_j^{(2)}}{dx}\right]dx$$

$$+\int_{x_a}^{x_b}\left[\frac{3}{2}\left(\sum_{K=1}^{M}\sum_{L=1}^{ND} {}^{D}D_{11}^{IJKL}\,\frac{dW_K}{dx}\frac{d\,{}^{D}W_L}{dx}\right)\frac{d\varphi_i^{(2)}}{dx}\frac{d\varphi_j^{(2)}}{dx}\right]dx$$

$$+\int_{x_a}^{x_b}\left[\left(\sum_{K=1}^{ND} {}^{D}\tilde{B}_{13}^{JKI}\,\frac{d\,{}^{D}W_K}{dx}\right)\varphi_i^{(2)}\,\frac{d\varphi_j^{(2)}}{dx} + \left(\sum_{K=1}^{ND} {}^{D}\tilde{B}_{13}^{IKJ}\,\frac{d\,{}^{D}W_K}{dx}\right)\frac{d\varphi_i^{(2)}}{dx}\varphi_j^{(2)}\right]dx$$

$$+\int_{x_a}^{x_b}\left[\left(\sum_{K=1}^{ND}\sum_{L=1}^{ND} {}^{D}\overline{D}_{11}^{IJKL}\,\frac{d\,{}^{D}W_K}{dx}\frac{d\,{}^{D}W_L}{dx}\right)\frac{d\varphi_i^{(2)}}{dx}\frac{d\varphi_j^{(2)}}{dx}\right]dx \tag{4.14f}$$

$$K_{ij}^{(23)IJ} = \int_{x_a}^{x_b} \left[\left(\sum_{K=1}^{M} {}^{D}\hat{B}_{11}^{IKJ} \frac{dW_K}{dx} \right) \frac{d\varphi_i^{(2)}}{dx} \frac{d\varphi_j^{(3)}}{dx} + {}^{D}\tilde{A}_{31}^{JI} \varphi_i^{(2)} \frac{d\varphi_j^{(3)}}{dx} \right] dx$$

$$+ \left(\sum_{K=1}^{ND} {}^{D}\hat{\hat{B}}_{55}^{IKJ} \frac{d\,{}^{D}W_K}{dx} \right) \frac{d\varphi_i^{(2)}}{dx} \frac{d\varphi_j^{(3)}}{dx} \Bigg] dx \tag{4.14g}$$

$$K_{ij}^{(24)IJ} = \int_{x_a}^{x_b} \left[\frac{1}{2} \left(\sum_{K=1}^{M} \sum_{L=1}^{ND} {}^{D}\bar{D}_{11}^{IKJL} \frac{dW_K}{dx} \frac{d\,{}^{D}W_L}{dx} \right) \frac{d\varphi_i^{(2)}}{dx} \frac{d\varphi_j^{(4)}}{dx} \right] dx$$

$$+ \int_{x_a}^{x_b} \left[\frac{1}{2} \left(\sum_{K=1}^{ND} {}^{D}\tilde{\tilde{B}}_{31}^{JKI} \frac{d\,{}^{D}W_K}{dx} \right) \varphi_i^{(2)} \frac{d\varphi_j^{(4)}}{dx} + {}^{D}\bar{A}_{55}^{IJ} \frac{d\varphi_i^{(2)}}{dx} \frac{d\varphi_j^{(4)}}{dx} \right] dx$$

$$+ \int_{x_a}^{x_b} \left[\frac{1}{2} \left(\sum_{K=1}^{ND} \sum_{L=1}^{ND} {}^{D}\bar{\bar{D}}_{11}^{IJKL} \frac{d\,{}^{D}W_K}{dx} \frac{d\,{}^{D}W_L}{dx} \right) \frac{d\varphi_i^{(2)}}{dx} \frac{d\varphi_j^{(4)}}{dx} \right] dx \tag{4.14h}$$

$$K_{ij}^{(31)IJ} = \int_{x_a}^{x_b} {}^{D}A_{11}^{JI} \frac{d\varphi_i^{(3)}}{dx} \frac{d\varphi_j^{(1)}}{dx} dx \tag{4.14i}$$

$$K_{ij}^{(32)IJ} = \int_{x_a}^{x_b} \left[\frac{1}{2} \left(\sum_{K=1}^{M} {}^{D}\hat{B}_{11}^{JKI} \frac{dW_K}{dx} \right) \frac{d\varphi_i^{(3)}}{dx} \frac{d\varphi_j^{(2)}}{dx} + {}^{D}\tilde{A}_{13}^{IJ} \frac{d\varphi_i^{(3)}}{dx} \varphi_j^{(2)} \right] dx \tag{4.14j}$$

$$+ \int_{x_a}^{x_b} \left(\sum_{K=1}^{ND} {}^{D}\hat{\hat{B}}_{11}^{JKI} \frac{d\,{}^{D}W_K}{dx} \right) \frac{d\varphi_i^{(3)}}{dx} \frac{d\varphi_j^{(2)}}{dx} dx \tag{4.14k}$$

$$K_{ij}^{(33)IJ} = \int_{x_a}^{x_b} {}^{D}\bar{\bar{A}}_{11}^{IJ} \frac{d\varphi_i^{(3)}}{dx} \frac{d\varphi_j^{(3)}}{dx} dx \tag{4.14l}$$

$$K_{ij}^{(34)IJ} = \int_{x_a}^{x_b} \frac{1}{2} \left(\sum_{K=1}^{ND} {}^{D}\bar{\bar{B}}_{11}^{IJK} \frac{d\,{}^{D}W_K}{dx} \right) \frac{d\varphi_i^{(3)}}{dx} \frac{d\varphi_j^{(4)}}{dx} dx \tag{4.14m}$$

$$K_{ij}^{(41)IJ} = \int_{x_a}^{x_b} \left[\left(\sum_{K=1}^{ND} {}^{D}B_{11}^{JIK} \frac{d\,{}^{D}W_K}{dx} \right) \frac{d\varphi_i^{(4)}}{dx} \frac{d\varphi_j^{(1)}}{dx} + {}^{D}\bar{B}_{55}^{JI} \frac{d\varphi_i^{(4)}}{dx} \varphi_j^{(1)} \right] dx \tag{4.14n}$$

$$K_{ij}^{(42)IJ} = \int_{x_a}^{x_b} \left[\frac{1}{2} \left(\sum_{K=1}^{M} \sum_{L=1}^{M} {}^{D}D_{11}^{JKLI} \frac{dW_K}{dx} \frac{dW_L}{dx} \right) \frac{d\varphi_i^{(4)}}{dx} \frac{d\varphi_j^{(2)}}{dx} \right] dx$$

$$+ \int_{x_a}^{x_b} \left[\left(\sum_{K=1}^{M} {}^{D}\tilde{B}_{13}^{JIK} W_K \right) \frac{d\varphi_i^{(4)}}{dx} \frac{d\varphi_j^{(2)}}{dx} + \left(\sum_{K=1}^{ND} {}^{D}\tilde{\tilde{B}}_{13}^{IKJ} \frac{d\,{}^{D}W_K}{dx} \right) \frac{d\varphi_i^{(4)}}{dx} \varphi_j^{(2)} \right] dx$$

$$+ \int_{x_a}^{x_b} \left[\left(\sum_{K=1}^{ND} \sum_{L=1}^{ND} {}^{D}\bar{\bar{D}}_{11}^{JIKL} \frac{d\,{}^{D}W_K}{dx} \frac{d\,{}^{D}W_L}{dx} \right) \frac{d\varphi_i^{(4)}}{dx} \frac{d\varphi_j^{(2)}}{dx} + {}^{D}\bar{A}_{55}^{JI} \frac{d\varphi_i^{(4)}}{dx} \frac{d\varphi_j^{(2)}}{dx} \right] dx$$

$$+ \int_{x_a}^{x_b} \left[\left(\sum_{K=1}^{N} {}^{D}B_{11}^{KJI} \frac{dU_K}{dx} \right) \frac{d\varphi_i^{(4)}}{dx} \frac{d\varphi_j^{(2)}}{dx} + \left(\sum_{K=1}^{ND} {}^{D}\hat{\hat{B}}_{11}^{JIK} \frac{d\,{}^{D}U_K}{dx} \right) \frac{d\varphi_i^{(4)}}{dx} \frac{d\varphi_j^{(2)}}{dx} \right] dx$$

$$+ \int_{x_a}^{x_b} \frac{1}{2} \left(\sum_{K=1}^{M} \sum_{L=1}^{ND} {}^{D}\bar{D}_{11}^{KJIL} \frac{dW_K}{dx} \frac{d\,{}^{D}W_L}{dx} \right) \frac{d\varphi_i^{(4)}}{dx} \frac{d\varphi_j^{(2)}}{dx} dx \tag{4.14o}$$

$$K_{ij}^{(43)IJ} = \int_{x_a}^{x_b} \left(\sum_{K=1}^{ND} {}^{D}\bar{\bar{B}}_{11}^{IJK} \frac{d\,{}^{D}W_K}{dx} \right) \frac{d\varphi_i^{(4)}}{dx} \frac{d\varphi_j^{(3)}}{dx} dx \tag{4.14p}$$

$$K_{ij}^{(44)IJ} = \int_{x_a}^{x_b} \left[\left(\sum_{K=1}^{M} \sum_{L=1}^{M} {}^{D}\bar{D}_{11}^{LKIJ} \frac{dW_K}{dx} \frac{dW_L}{dx} \right) \frac{d\varphi_i^{(4)}}{dx} \frac{d\varphi_j^{(4)}}{dx} + {}^{D}\bar{\bar{A}}_{55}^{IJ} \frac{d\varphi_i^{(4)}}{dx} \frac{d\varphi_j^{(4)}}{dx} \right.$$

$$+ \frac{1}{2} \left(\sum_{K=1}^{M} \sum_{L=1}^{ND} {}^{D}\bar{\bar{D}}_{11}^{KIJL} \frac{dW_K}{dx} \frac{d\,{}^{D}W_L}{dx} \right) \frac{d\varphi_i^{(4)}}{dx} \frac{d\varphi_j^{(4)}}{dx}$$

$$\left. + \frac{1}{2} \left(\sum_{K=1}^{ND} \sum_{L=1}^{ND} {}^{D}\bar{\bar{\bar{D}}}_{11}^{IJKL} \frac{d\,{}^{D}W_K}{dx} \frac{d\,{}^{D}W_L}{dx} \right) \frac{d\varphi_i^{(4)}}{dx} \frac{d\varphi_j^{(4)}}{dx} \right] dx \tag{4.14q}$$

and

$$ {}^{1}F_i^I = \begin{cases} \int_{x_a}^{x_b} f_b(x)\varphi_i^{(1)} dx & \left(I = 1\right) \\ \int_{x_a}^{x_b} f_t(x)\varphi_i^{(1)} dx & \left(I = N\right) \\ 0 & \left(I = 2,3,\cdots,N-1\right) \end{cases} \tag{4.15a} $$

$$ {}^{2}F_i^I = \begin{cases} \int_{x_a}^{x_b} q_b(x)\varphi_i^{(2)} dx & \left(I = 1\right) \\ \int_{x_a}^{x_b} q_t(x)\varphi_i^{(2)} dx & \left(I = M\right) \\ 0 & \left(I = 2,3,\cdots,M-1\right) \end{cases} \tag{4.15b} $$

Note that the coefficient matrices contain nonlinearity in such a way that they are functions of the unknowns $U(x)$, $W(x)$, ${}^{D}U(x)$ and ${}^{D}W(x)$.

The equations (4.13) through (4.15b) are used to compute the nonlinear responses based on the direct iteration scheme. The solution obtained from direct iteration converges if the nonlinearity is not very prominent but it tends to diverge if the nonlinearity is severe. Divergence is more likely for hardening type nonlinearity. In this study, the nonlinearity is strongly involved in the formulation due to the von Kármán type strain field. Thus, another numerical iteration scheme known as the Newton-Raphson method is employed. The Newton-Raphson method makes use of the residual vector of the finite element equations (4.15a) and (4.15b), and its Taylor's series about the solution from the previous iteration. Here, the details of the Newton-Raphson

method are omitted and, instead, the components of the tangent matrix for the nonlinear layer-wise beam model are listed as follows

$$T_{ij}^{(11)IJ} = K_{ij}^{(11)IJ} \tag{4.16a}$$

$$T_{ij}^{(12)IJ} = \int_{x_a}^{x_b} \frac{1}{2}\left(\sum_{K=1}^{M} B_{11}^{IKJ} \frac{dW_K}{dx}\right)\frac{d\varphi_i^{(1)}}{dx}\frac{d\varphi_j^{(2)}}{dx}dx + K_{ij}^{(12)IJ} \tag{4.16b}$$

$$T_{ij}^{(13)IJ} = K_{ij}^{(13)IJ} \tag{4.16c}$$

$$T_{ij}^{(14)IJ} = \int_{x_a}^{x_b} \left[\left(\sum_{K=1}^{M} {}^{D}B_{11}^{IKJ} \frac{dW_K}{dx}\right)\frac{d\varphi_i^{(1)}}{dx}\frac{d\varphi_j^{(4)}}{dx} + \frac{1}{2}\left(\sum_{K=1}^{ND} {}^{D}\bar{B}_{11}^{IJK} \frac{d\,{}^{D}W_K}{dx}\right)\frac{d\varphi_i^{(1)}}{dx}\frac{d\varphi_j^{(4)}}{dx}\right]dx$$

$$+K_{ij}^{(14)IJ} \tag{4.16d}$$

$$T_{ij}^{(21)IJ} = K_{ij}^{(21)IJ} \tag{4.16e}$$

$$\begin{aligned} T_{ij}^{(22)IJ} = \int_{x_a}^{x_b} \Bigg[& \left(\sum_{K=1}^{N} B_{11}^{KIJ} \frac{dU_K}{dx}\right)\frac{d\varphi_i^{(2)}}{dx}\frac{d\varphi_j^{(2)}}{dx} + \left(\sum_{K=1}^{M}\sum_{L=1}^{M} D_{11}^{IKJL} \frac{dW_K}{dx}\frac{dW_L}{dx}\right)\frac{d\varphi_i^{(2)}}{dx}\frac{d\varphi_j^{(2)}}{dx} \\ & + \left(\sum_{K=1}^{M} \tilde{B}_{13}^{IJK} W_K\right)\frac{d\varphi_i^{(2)}}{dx}\frac{d\varphi_j^{(2)}}{dx} + \frac{1}{2}\left(\sum_{K=1}^{M} \tilde{B}_{31}^{KJI} \frac{dW_K}{dx}\right)\varphi_i^{(2)}\frac{d\varphi_j^{(2)}}{dx} \\ & + \frac{3}{2}\left(\sum_{K=1}^{M}\sum_{L=1}^{ND} {}^{D}D_{11}^{IKJL} \frac{dW_K}{dx}\frac{d\,{}^{D}W_L}{dx}\right)\frac{d\varphi_i^{(2)}}{dx}\frac{d\varphi_j^{(2)}}{dx} + \left(\sum_{K=1}^{ND} {}^{D}\hat{B}_{13}^{IJK} \frac{d\,{}^{D}U_K}{dx}\right)\frac{d\varphi_i^{(2)}}{dx}\frac{d\varphi_j^{(2)}}{dx} \\ & + \frac{1}{2}\left(\sum_{K=1}^{ND}\sum_{L=1}^{ND} {}^{D}\bar{D}_{11}^{IJKL} \frac{d\,{}^{D}W_K}{dx}\frac{d\,{}^{D}W_L}{dx}\right)\frac{d\varphi_i^{(2)}}{dx}\frac{d\varphi_j^{(2)}}{dx}\Bigg]dx + K_{ij}^{(22)IJ} \end{aligned} \tag{4.16f}$$

$$T_{ij}^{(23)IJ} = K_{ij}^{(23)IJ} \tag{4.16g}$$

$$T_{ij}^{(24)IJ} = \int_{x_a}^{x_b} \left[\left(\sum_{K=1}^{N} {}^{D}B_{11}^{KIJ} \frac{dU_K}{dx}\right)\frac{d\varphi_i^{(2)}}{dx}\frac{d\varphi_j^{(4)}}{dx} + \frac{3}{2}\left(\sum_{K=1}^{M}\sum_{L=1}^{M} {}^{D}D_{11}^{ILKJ} \frac{dW_K}{dx}\frac{dW_L}{dx}\right)\frac{d\varphi_i^{(2)}}{dx}\frac{d\varphi_j^{(4)}}{dx}\right.$$

$$+\left(\sum_{K=1}^{M} {}^{D}\tilde{B}_{31}^{KJI}\frac{dW_K}{dx}\right)\varphi_i^{(2)}\frac{d\varphi_j^{(4)}}{dx}+\left(\sum_{K=1}^{M} {}^{D}\tilde{B}_{13}^{IJK}W_K\right)\frac{d\varphi_i^{(2)}}{dx}\frac{d\varphi_j^{(4)}}{dx}$$

$$+2\left(\sum_{K=1}^{M}\sum_{L=1}^{ND} {}^{D}\bar{D}_{11}^{IKJL}\frac{dW_K}{dx}\frac{d\,{}^{D}W_L}{dx}\right)\frac{d\varphi_i^{(2)}}{dx}\frac{d\varphi_j^{(4)}}{dx}+\left(\sum_{K=1}^{ND} {}^{D}\hat{\hat{B}}_{11}^{IJK}\frac{d\,{}^{D}U_K}{dx}\right)\frac{d\varphi_i^{(2)}}{dx}\frac{d\varphi_j^{(4)}}{dx}$$

$$+\frac{1}{2}\left(\sum_{K=1}^{M}\sum_{L=1}^{ND} {}^{D}\bar{D}_{11}^{IKLJ}\frac{dW_K}{dx}\frac{d\,{}^{D}W_L}{dx}\right)\frac{d\varphi_i^{(2)}}{dx}\frac{d\varphi_j^{(4)}}{dx}+\frac{1}{2}\left(\sum_{K=1}^{ND} {}^{D}\tilde{\tilde{B}}_{31}^{KJI}\frac{d\,{}^{D}W_K}{dx}\right)\varphi_i^{(2)}\frac{d\varphi_j^{(4)}}{dx}$$

$$+\left(\sum_{K=1}^{ND}\sum_{L=1}^{ND} {}^{D}\bar{\bar{D}}_{11}^{IKJL}\frac{d\,{}^{D}W_K}{dx}\frac{d\,{}^{D}W_L}{dx}\right)\frac{d\varphi_i^{(2)}}{dx}\frac{d\varphi_j^{(4)}}{dx}\Bigg]dx+K_{ij}^{(24)IJ} \tag{4.16h}$$

$$T_{ij}^{(31)IJ}=K_{ij}^{(31)IJ} \tag{4.16i}$$

$$T_{ij}^{(32)IJ}=\int_{x_a}^{x_b}\frac{1}{2}\left(\sum_{K=1}^{M} {}^{D}\hat{B}_{11}^{KJI}\frac{dW_K}{dx}\right)\frac{d\varphi_i^{(3)}}{dx}\frac{d\varphi_j^{(2)}}{dx}dx+K_{ij}^{(32)IJ} \tag{4.16j}$$

$$T_{ij}^{(33)IJ}=K_{ij}^{(33)IJ} \tag{4.16k}$$

$$T_{ij}^{(34)IJ}=\int_{x_a}^{x_b}\left[\left(\sum_{K=1}^{M} {}^{D}\hat{\hat{B}}_{11}^{KJI}\frac{dW_K}{dx}\right)\frac{d\varphi_i^{(3)}}{dx}\frac{d\varphi_j^{(4)}}{dx}+\frac{1}{2}\left(\sum_{K=1}^{ND} {}^{D}\bar{\bar{B}}_{11}^{IKJ}\frac{d\,{}^{D}W_K}{dx}\right)\frac{d\varphi_i^{(3)}}{dx}\frac{d\varphi_j^{(4)}}{dx}\right]dx$$

$$+K_{ij}^{(34)IJ} \tag{4.16l}$$

$$T_{ij}^{(41)IJ}=\int_{x_a}^{x_b}\left(\sum_{K=1}^{M} {}^{D}B_{11}^{JKI}\frac{dW_K}{dx}\right)\frac{d\varphi_i^{(4)}}{dx}\frac{d\varphi_j^{(1)}}{dx}dx+K_{ij}^{(41)IJ} \tag{4.16m}$$

$$T_{ij}^{(42)IJ}=\int_{x_a}^{x_b}\left[\left(\sum_{K=1}^{M}\sum_{L=1}^{M} {}^{D}D_{11}^{JKLI}\frac{dW_K}{dx}\frac{dW_L}{dx}\right)\frac{d\varphi_i^{(4)}}{dx}\frac{d\varphi_j^{(2)}}{dx}+\left(\sum_{K=1}^{M} {}^{D}\tilde{B}_{13}^{KIJ}\frac{dW_K}{dx}\right)\frac{d\varphi_i^{(4)}}{dx}\varphi_j^{(2)}\right.$$

$$+\frac{5}{2}\left(\sum_{K=1}^{M}\sum_{L=1}^{ND} {}^{D}\bar{D}_{11}^{JKIL}\frac{dW_K}{dx}\frac{d\,{}^{D}W_L}{dx}\right)\frac{d\varphi_i^{(4)}}{dx}\frac{d\varphi_j^{(2)}}{dx} \tag{4.16n}$$

$$\left.+\frac{1}{2}\left(\sum_{K=1}^{ND}\sum_{L=1}^{ND} {}^{D}\bar{\bar{D}}_{11}^{JIKL}\frac{d\,{}^{D}W_K}{dx}\frac{d\,{}^{D}W_L}{dx}\right)\frac{d\varphi_i^{(4)}}{dx}\frac{d\varphi_j^{(2)}}{dx}\right]dx+K_{ij}^{(42)IJ} \tag{4.16o}$$

$$T_{ij}^{(43)IJ} = \int_{x_a}^{x_b} \left(\sum_{K=1}^{M} {}^{D}\hat{\hat{B}}_{11}^{KIJ} \frac{dW_K}{dx} \right) \frac{d\varphi_i^{(4)}}{dx} \frac{d\varphi_j^{(3)}}{dx} dx + K_{ij}^{(43)IJ} \tag{4.16p}$$

$$\begin{aligned} T_{ij}^{(44)IJ} = \int_{x_a}^{x_b} \Bigg[& \left(\sum_{K=1}^{N} {}^{D}\bar{B}_{11}^{KIJ} \frac{dU_K}{dx} \right) \frac{d\varphi_i^{(4)}}{dx} \frac{d\varphi_j^{(4)}}{dx} + \frac{1}{2} \left(\sum_{K=1}^{M} \sum_{L=1}^{M} {}^{D}\bar{D}_{11}^{LKIJ} \frac{dW_K}{dx} \frac{dW_L}{dx} \right) \frac{d\varphi_i^{(4)}}{dx} \frac{d\varphi_j^{(4)}}{dx} \\ & + 2 \left(\sum_{K=1}^{M} \sum_{L=1}^{ND} {}^{D}\bar{\bar{D}}_{11}^{KIJL} \frac{dW_K}{dx} \frac{d\,{}^{D}W_L}{dx} \right) \frac{d\varphi_i^{(4)}}{dx} \frac{d\varphi_j^{(4)}}{dx} + \left(\sum_{K=1}^{M} {}^{D}\tilde{\tilde{B}}_{13}^{IJK} W_K \right) \frac{d\varphi_i^{(4)}}{dx} \frac{d\varphi_j^{(4)}}{dx} \\ & + \left(\sum_{K=1}^{ND} {}^{D}\bar{\bar{B}}_{11}^{IKJ} \frac{d\,{}^{D}U_K}{dx} \right) \frac{d\varphi_i^{(4)}}{dx} \frac{d\varphi_j^{(4)}}{dx} + \frac{1}{2} \left(\sum_{K=1}^{M} \sum_{L=1}^{ND} {}^{D}\bar{\bar{D}}_{11}^{KILJ} \frac{dW_K}{dx} \frac{d\,{}^{D}W_L}{dx} \right) \frac{d\varphi_i^{(4)}}{dx} \frac{d\varphi_j^{(4)}}{dx} \\ & + \left(\sum_{K=1}^{ND} \sum_{L=1}^{ND} {}^{D}\bar{\bar{\bar{D}}}_{11}^{IJKL} \frac{d\,{}^{D}W_K}{dx} \frac{d\,{}^{D}W_L}{dx} \right) \frac{d\varphi_i^{(4)}}{dx} \frac{d\varphi_j^{(4)}}{dx} \Bigg] dx + K_{ij}^{(44)IJ} \end{aligned} \tag{4.16q}$$

Unlike the unsymmetric coefficient matrix in the direct iteration method, the tangent stiffness matrix is symmetric in the Newton-Raphson method for the nonlinear case.

4.3 Numerical Examples

4.3.1 Mid-plane Delamination

A laminated beam of $[90_m / 0_n / 90_m / 0_n]_s$ lay-ups with pre-delamination through the width in the mid-plane is considered for an example to demonstrate the accuracy of solutions using the current layer-wise theory taking into account delamination (LWTDEL). The laminated beam is subjected to three-point-bending and the problem definitions are taken from Zhao *et al.*[67]. The configurations and the boundary conditions of the problem are displayed in Fig. 4.1.

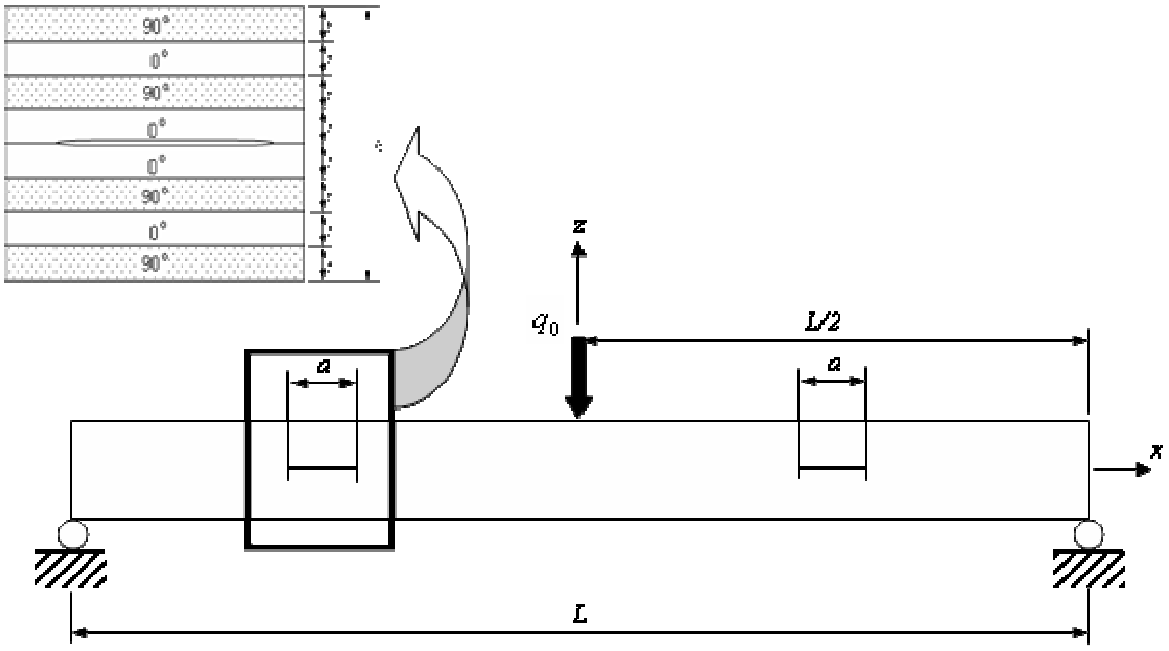

Fig. 4.1. Configurations of laminated beam under three-point bending

The material properties of NCT-301 graphite/epoxy composite used in this numerical example are same as in [67], which are

$$E_1 = 145\,\text{GPa} \qquad E_2 = E_3 = 10.7\,\text{GPa}$$

$$G_{12} = G_{13} = 4.5\,\text{GPa} \qquad G_{23} = 3.6\,\text{GPa}$$

$$\nu_{12} = \nu_{13} = 0.3 \qquad \nu_{23} = 0.49\,.$$

The result of the numerical example is shown through the interlaminar shear stress distribution near the delaminated mid-plane along the beam length for the case of $m = n = 4$ and the static bending load q_0 applied at the beam center. Noting the beam is symmetric about the beam center, half of the beam is modeled. The stress values are normalized by τ_0 defined as $3q_0 / 4h$ where h is the total thickness (4mm) of the laminated beam. In discretization, 36 linear beam elements are used along the beam length direction. Since each angle ply's thickness is uniform in this case, the physical 4 layers of each 0° ply and 90° ply are modeled as a single numerical layer using one quadratic interpolation function through the numerical layer's thickness direction respectively. In the aspect of the numerical solutions, the selective reduced numerical integration scheme [63] is used for the transverse shear and transverse normal components of the coefficients in equations (4.14a)-(4.14q) and (4.16a)-(4.16q) to avoid shear locking. The solutions are obtained at the Gauss points nearest to the mid-plane of beam elements along the beam length.

As can be seen in Fig. 4.2, a very good agreement can be found between the solutions of LWTDEL and that of Zhao *et al*. [67]. The solution based on the linear strain fields and the solution of Zhao et al show a symmetric stress distribution about the interlaminar crack center, whereas the nonlinear solution of LWTDEL shows an unsymmetric stress distribution owing to the hardening effect caused by the nonlinearity in strain field.

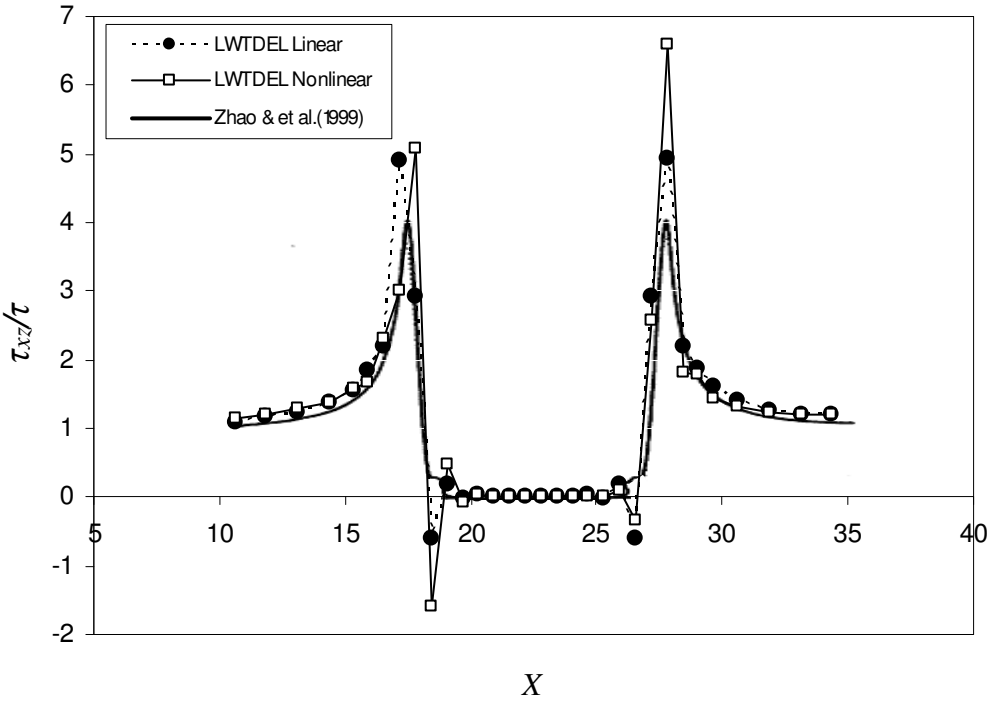

Fig. 4.2. Nondimensionalized interlaminar shear stress $\overline{\tau}_{xz} = \dfrac{\tau_{xz}}{3q_0/4h}$ distribution near the delaminated mid-plane along the simply supported beam length ($\overline{\tau}_{xz}(x,-0.014088)$ when $q_0 = 400N/mm$)

Zhao *et al.* [67] was interested in the concentration of shear stress around the interlaminar crack tips but they did not provide other stress components along the beam length nor the stress distribution through the thickness direction. Fig. 4.3 and Fig. 4.4 display the axial normal stress and the interlaminar normal stress distribution along the mid-plane of the delaminated beam near the tips of interlaminar crack. The stress distributions through the thickness of the linear beams are shown in Fig. 4.5 through 4.7.

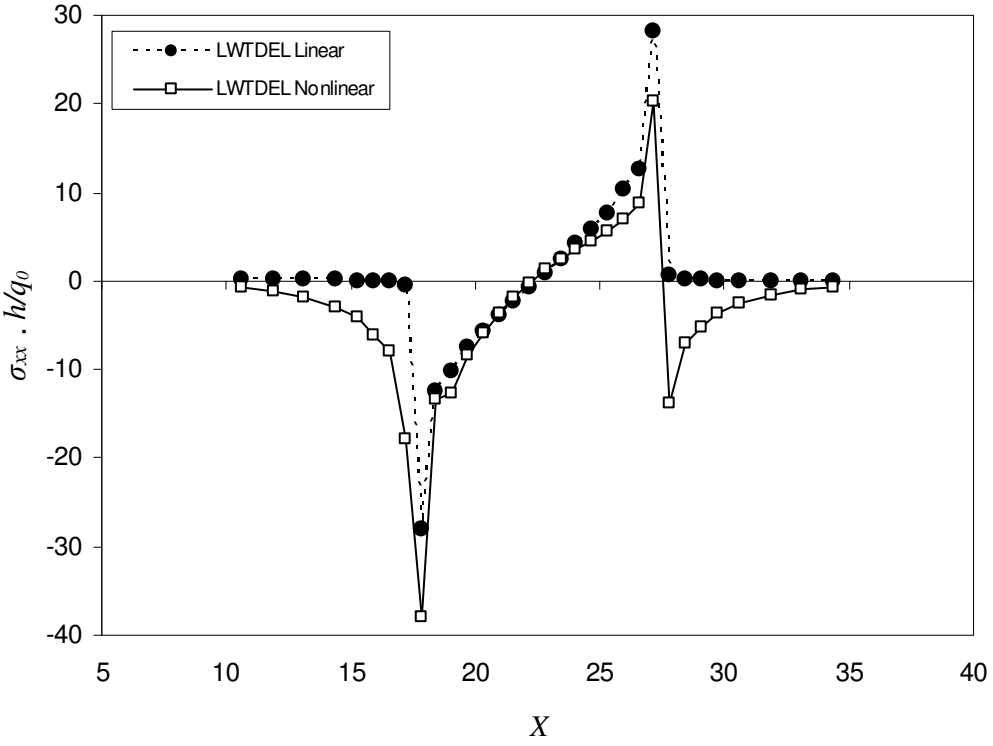

Fig. 4.3. Nondimensional axial stress $\bar{\sigma}_{xx} = \dfrac{\sigma_{xx}}{q_0 / h}$ distribution near the delaminated mid-plane along the simply supported beam length ($\bar{\sigma}_{xx}(x, -0.014088)$ when $q_0 = 400N / mm$)

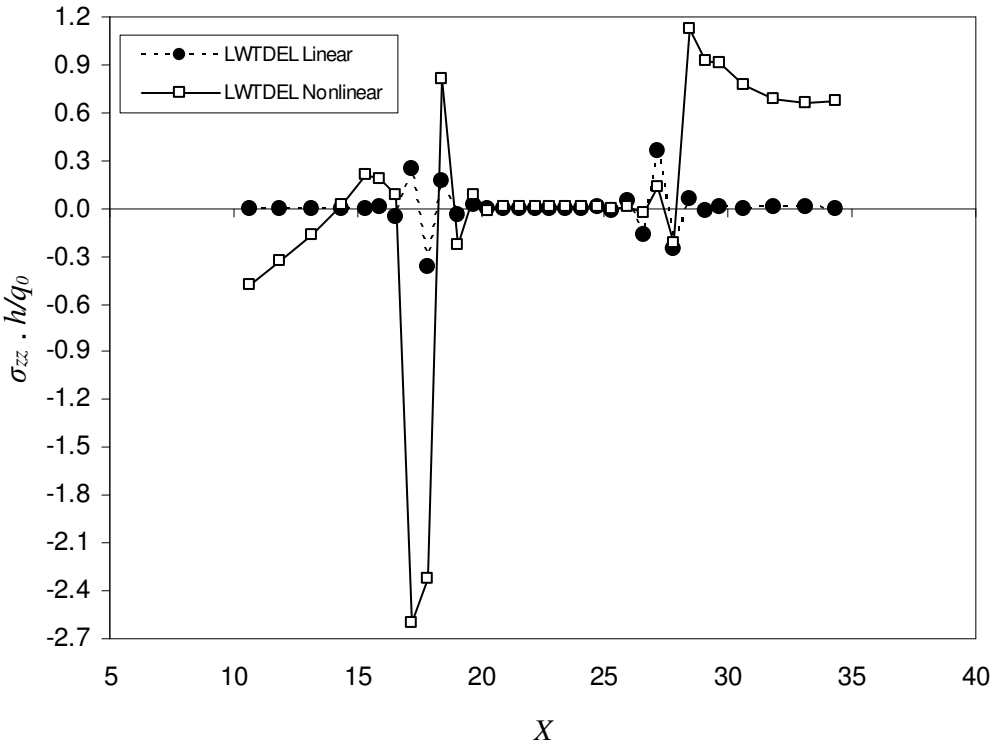

Fig. 4.4. Nondimensional interlaminar normal stress $\bar{\sigma}_{zz} = \dfrac{\sigma_{zz}}{q_0 / h}$ distribution near the delaminated mid-plane along the simply supported beam length ($\bar{\sigma}_{zz}(x, -0.014088)$ when $q_0 = 400N / mm$)

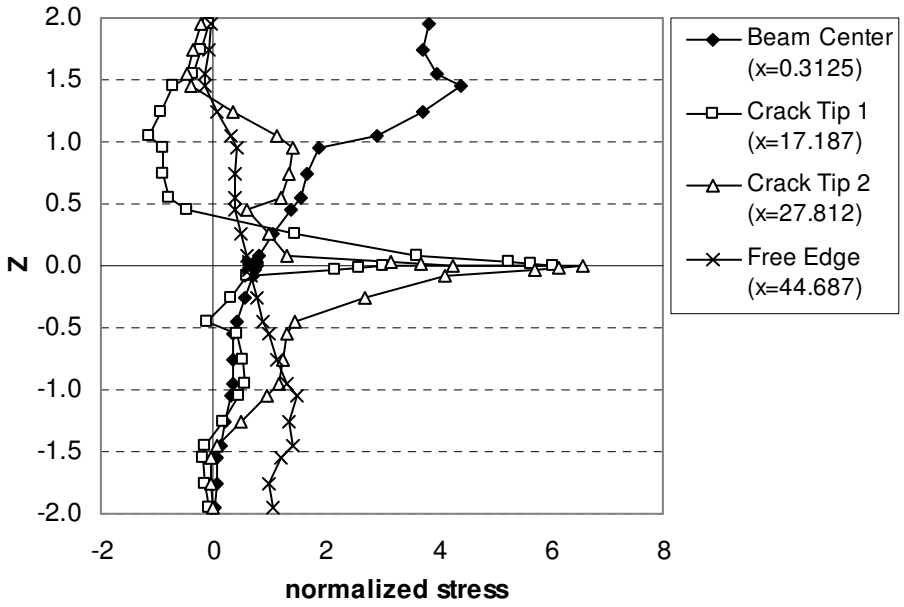

Fig. 4.5. Nondimensionalized interlaminar shear stress $\bar{\tau}_{xz} = \dfrac{\tau_{xz}}{3q_0 / 4h}$ distribution through the thickness of the simply supported beam length ($\bar{\tau}_{xz}(x, z)$ when $q_0 = 400N / mm$)

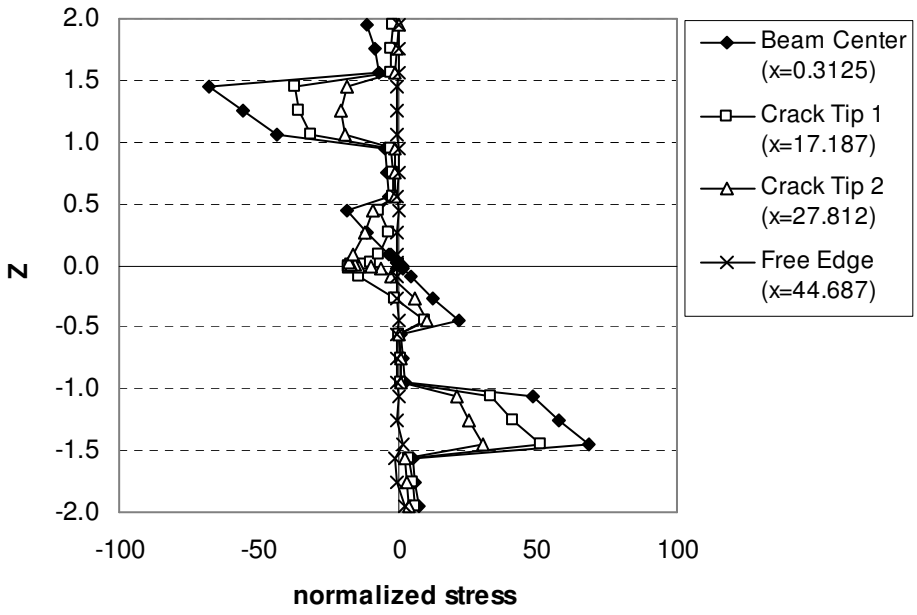

Fig. 4.6. Nondimensionalized axial normal stress $\bar{\sigma}_{xx} = \dfrac{\sigma_{xx}}{q_0 / h}$ distribution through the thickness of the simply supported beam length ($\bar{\sigma}_{xx}(x, z)$ when $q_0 = 400N / mm$)

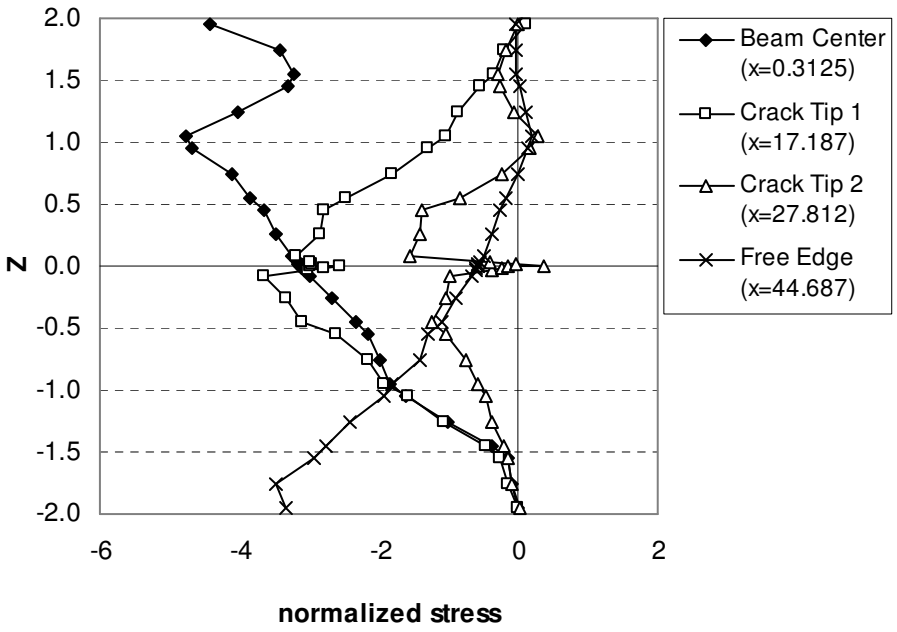

Fig. 4.7. Nondimensionalized interlaminar normal stress $\bar{\sigma}_{zz} = \dfrac{\sigma_{zz}}{q_0 / h}$ distribution through the thickness of the simply supported beam length ($\bar{\sigma}_{zz}(x, z)$ when $q_0 = 400N / mm$)

4.3.2 Free Edge Delamination

In a number of works [32, 33, 68-71], stress concentration at the free-edge of composite laminates was reported. This phenomenon was often attributed to the delamination formed from the free-edge of the laminate structure. Many of the free-edge delamination

phenomena were investigated under the axial extension load [32, 33, 69, 70]. The interlaminar normal and shear stress were commonly pointed as the main contribution to onset of the free-edge delamination under the axial load. Some of the researchers studied the free-edge delamination under bending loads[68, 71]. Among those, Feraboli and Kedward [71] proposed a four-point bending test method to study the interlaminar shear strength of the composite laminate with various configurations. They examined the shear stress distribution in the composite laminates and observed the interlaminar crack forming near the support during the bending test. When the failure was detected, the interlaminar shear stress was recorded as the interlaminar shear strength of the composite laminates. Here, a stress analysis on the same configuration of composite laminates as in Feraboli and Kedward [71] is conducted using LWTDEL.

The material properties of the carbon fiber reinforced epoxy used in this section are as follows

$$E_1 = 18\,\text{Msi} \qquad E_2 = E_3 = 1.5\,\text{Msi}$$

$$G_{12} = G_{13} = 0.8\,\text{Msi} \qquad G_{23} = 0.6\,\text{Msi}$$

$$\nu_{12} = \nu_{13} = 0.3 \qquad \nu_{23} = 0.35\,.$$

Fig. 4.8 displays the configuration of the composite laminated beam under four-point bending load as in [71]. The bold letters A, B and C in Fig. 4.8 indicates the locations of loading, mid-span between loading and support, and support, respectively. The applied forces q_o are 1027.5 lb/in for the lay-ups of $[0]_s$ and 1206.0 lb/in for

$[0/90]_s$, which are equivalent to the experimental values measured as the maximum load in [71].

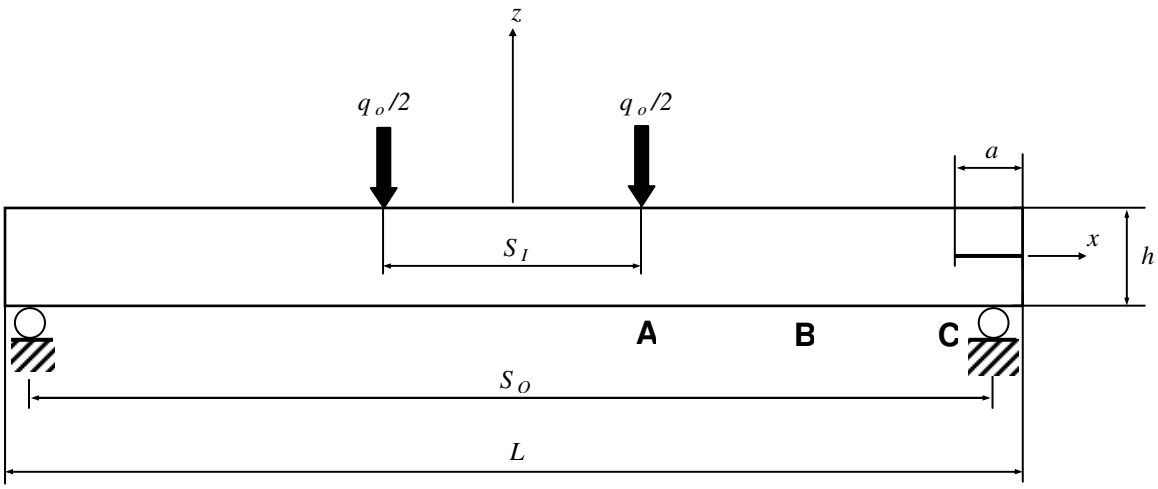

Fig. 4.8. Configurations of laminated beam under four-point bending

The dimensional values described in Fig. 4.8 are listed in Table 1.1 for the two cases of $[0]_s$ and $[0/90]_s$ lay-up configurations.

Table 1.1. Dimensions of laminated beam under four-point bending

(unit = inch)

	S_I	S_O	L	h	a	*width*
$[0]_s$	0.5	1.25	1.3	0.139	0.177	0.236
$[0/90]_s$	0.5	1.25	1.3	0.163	0.177	0.284

Making use of the symmetry condition about the z-axis, 32 linear elements with 12 numerical layers were modeled in the finite element analysis using LWTDEL. The interlaminar shear stress distributions through the thickness computed at the nearest Gauss points to the locations A, B and C in Fig. 4.9 are depicted in Fig. 4.10. The maximum shear stress was found at the mid-plane of the beam between loading and support points.

Fig. 4.11 displays the shear stress distribution along the beam length evaluated at the nearest Gauss points to the mid-plane. The maximum shear stress was found at a region near the support and this coincides with the experimental observation of Feraboli and Kedward [71] that the interlaminar failure propagated from a region located about one thickness away from the support, usually at the axis of symmetry. They also suspected that the interlaminar crack initiated from the location showing the maximum interlaminar shear stress.

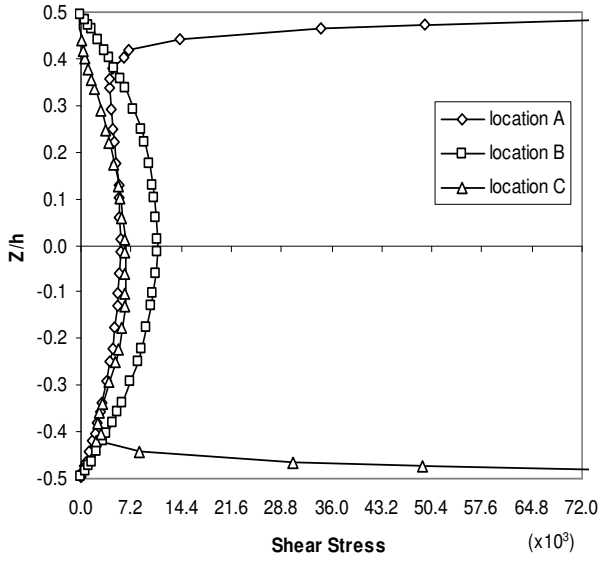

(a)

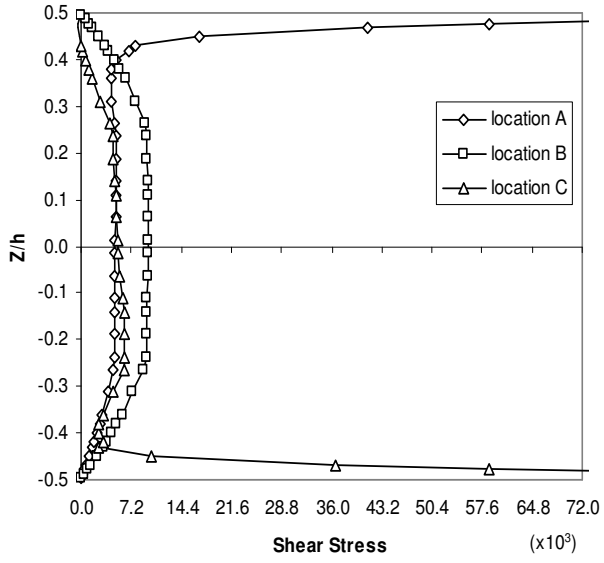

(b)

Fig. 4.9. Interlaminar shear stress distribution through the thickness ($\tau_{xz}(x_i, z)$) for the lay-ups of (a) $[0]_s$ (b) $[0/90^\circ]_s$

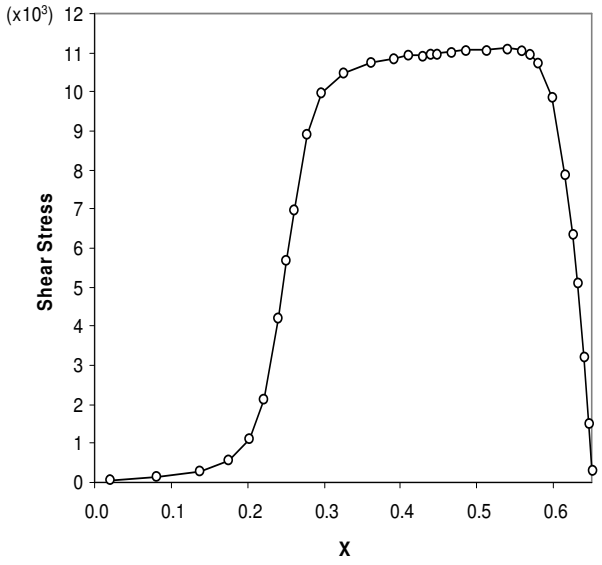

(a)

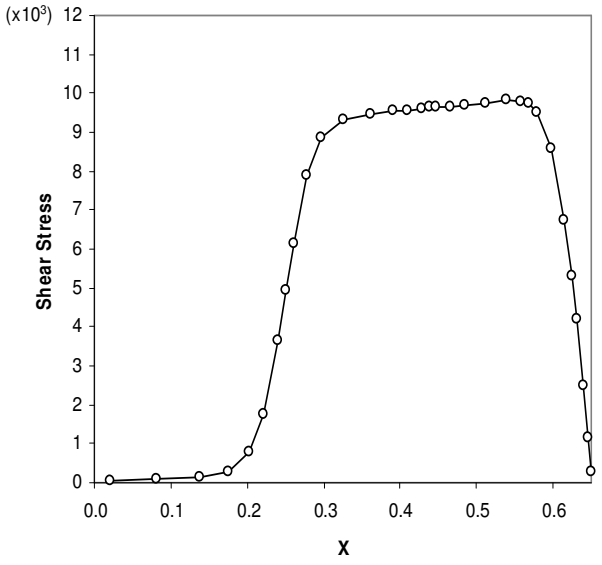

(b)

Fig. 4.10. Interlaminar shear stress distribution along the beam ($\tau_{xz}(x, 0.0033445h)$) for the lay-ups of (a) $[0]_s$ (b) $[0/90^\circ]_s$

The maximum shear stress obtained from LWTDEL for $[0]_s$ lay-ups shows a less value than the case of $[0/90]_s$, mainly due to the lower axial material stiffness in 90° plies.

The graphs of interlaminar shear stress distribution shown in Fig. 4.9 to 4.10 are based on the results before the delamination failure occurs in the beam and the values show an excellent agreement with the experimental results as well as the numerical solutions using three dimensional elements reported in [71]. According to the experimental discovery of Feraboli and Kedward [71], the failure occurs suddenly in a macroscopically brittle mode. Assuming the initial crack completely propagates toward the free-edge, redistribution of the interlaminar shear stress is displayed in Figs. 4.11 to 4.12, under the same load. From Fig. 4.11, the compressive side of the bending beam seems to lose the capacity to carry the shear load near the crack tip after the delamination failure. Whereas, the tensile side of the bending beam shows higher interlaminar shear stress values through the thickness. A sharp increase of stress at the crack tip is commonly seen in Fig. 4.11 and 4.12 for $[0]_s$ and $[0/90^\circ]_s$ configurations when the interlaminar failure occurs, as expected.

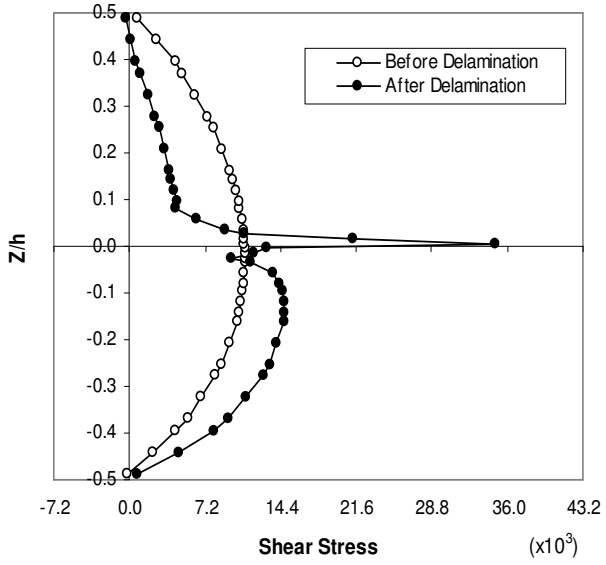

(a)

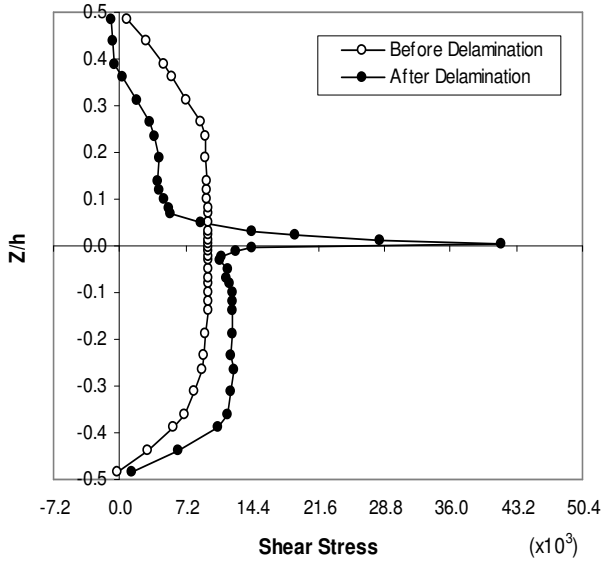

(b)

Fig. 4.11. Redistribution of interlaminar shear stress through the thickness at the crack tip ($\tau_{xz}(x_i, z)$) for the lay-ups of (a) $[0]_s$ (b) $[0/90^\circ]_s$

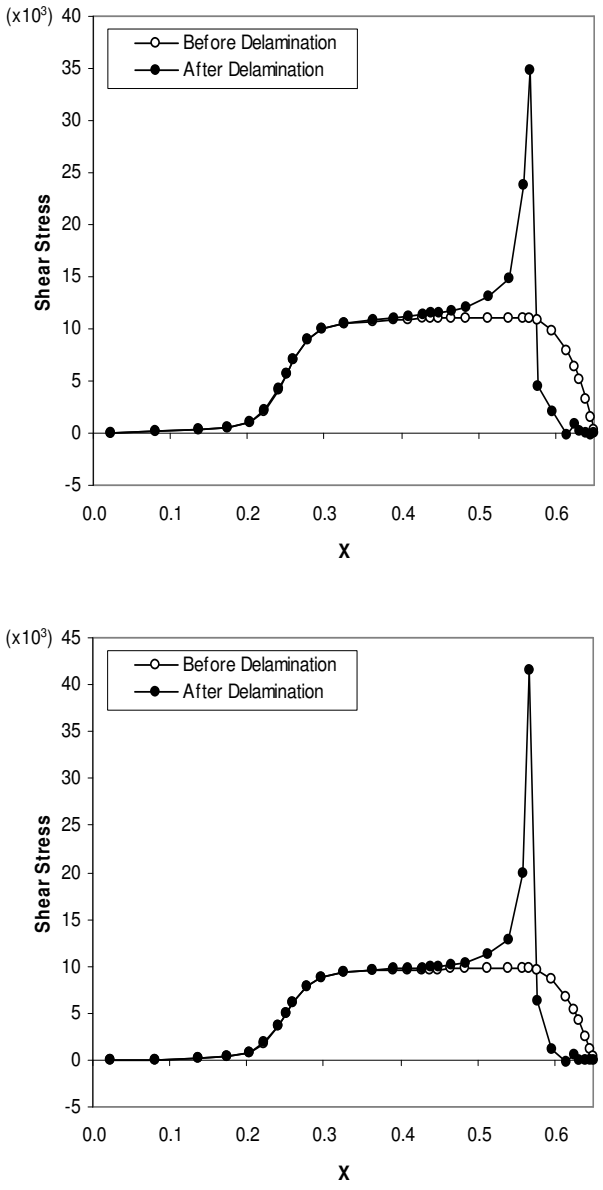

Fig. 4.12. Redistribution of interlaminar shear stress along the beam length ($\tau_{xz}(x, 0.0033445h)$) due to delamination for the lay-ups of (a) $[0]_s$ (b) $[0/90^\circ]_s$

CHAPTER V

PROGRESSIVE DELAMINATION

5.1 Fracture Mechanics

Once the delamination occurs in the composite laminate structure, its growth is predicted by the fracture criterion such as the energy required to create the new surface in the structure. In the frame work of fracture mechanics, the strain energy release rate is often used to judge the growth of the existing crack.

Using the theorem of minimum potential energy, Griffith[28] proposed the condition for a crack to extend by equating the rate of strain energy increase required for forming new surfaces with the rate of potential energy of the crack surface. This idea inspired a number of researchers to form the concept of the strain energy release rate in the fracture mechanics framework. Irwin [72] pointed out that the strain energy release rate and the stress intensity factor as fracture parameters. He made use of the method of Westergaard [73] to show the singular part of any stress component near the crack tip as

$$\sigma_{ij} = \sqrt{GE}\,\frac{1}{\sqrt{2\pi r}}\,f_{ij}(\theta) \tag{5.1}$$

where the stress component σ_{ij} was described by the strain energy release rate G, Young's modulus E, the radius of the location from the crack tip r and a function of the angle θ (see Fig. 5. 1).

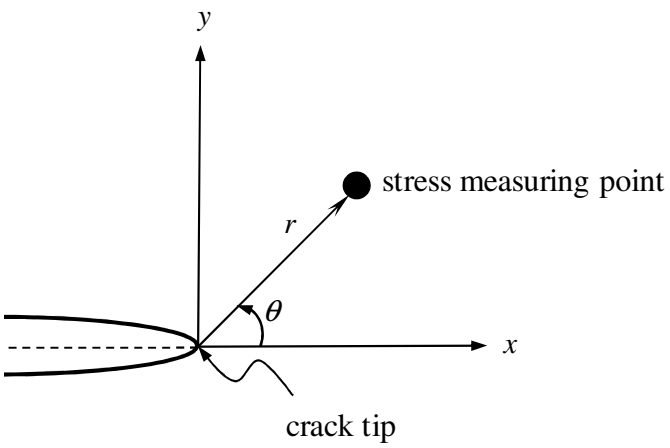

Fig. 5.1. General fracture problem

The stress intensity factor is invoked in his work for the plane stress case, and the relationship with the strain energy release rate has been shown as

$$G = \frac{K^2}{E} \tag{5.2}$$

where K indicates the stress intensity factor. It is shown that Poisson's ratio ν has to be taken into account for the case of plane strain [74], and thus,

$$G = \frac{K^2}{E}(1-\nu^2)\,. \tag{5.3}$$

More importantly, Irwin postulated the idea of crack closure technique to compute the strain energy release rate for Mode I, which turns out

$$\frac{1}{2}\int_0^{\alpha} \sigma_y(\alpha) v(0) dp = \alpha G \tag{5.4}$$

where α is the distance of the virtual crack extension, $\sigma_y(\alpha)$ is the stress component in y-direction at $x = \alpha$ and $v(0)$ denotes the deformation of the point at $x = 0$ in y-direction(see Fig. 5.2).

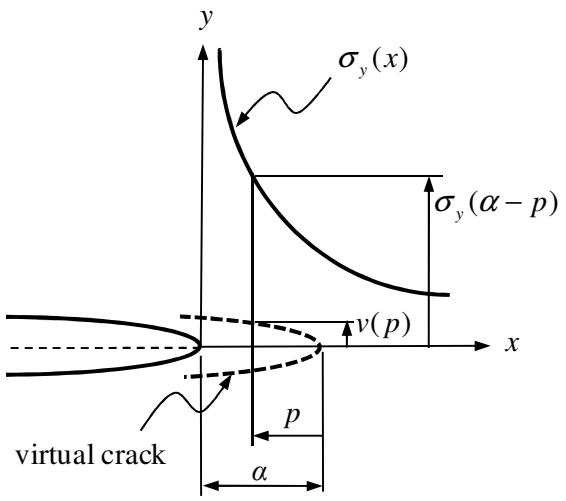

Fig. 5.2. Virtual crack closure technique

Since Irwin introduced the virtual crack closure technique, there have been many attempts to compute the strain energy release rate by finding the analytical solutions[75-77]. Paris and Sih [75] summarized the stress distribution near the crack tip for various configurations of cracks in 2-D homogeneous materials. They also compared the stress intensity factors and its correction factors by giving the solutions of different approaches. Fedderson [76] discussed about the analytical solutions for the finite width correction of the stress intensity factor($K/\sigma_0\sqrt{\pi a}$). He compared the various analytical solutions side by side in the form of table and considered the solution of Isida [77] as the most precise expression.

5.2 Computing Strain Energy Release Rate

The finite element methods were adopted by some researchers [78-83] to compute the strain energy release rate or the stress intensity factors. Some researchers [79, 80] have attempted to compute directly from two computations of two configurations with different crack lengths and others [78, 81-83] came up with methods to calculate with a single computation. In particular, Rybicki and Kanninen [78] modified Irwin's crack closure integral in terms of the nodal forces and displacements at the crack tip elements. They evaluated the strain energy release rate to compute the stress intensity factor using 4-node 2-D finite elements. That is,

$$G = \frac{1}{2\alpha} F_c (v_c - v_d) \tag{5.5}$$

where v_c and v_d represent the y-directional crack opening displacements at nodes *c* and *d*, respectively, and F_c is a force in y-direction to hold the nodes *c* and *d* together (see Fig. 5.3).

Rybicki and Kanninen [78] suggested that F_c be evaluated as the y-directional force at the node *e* for the case of the same element lengths of α and l in Fig 5.3. Later on, Raju [83] employed the higher order and singular elements for the crack tip elements to improve the accuracy of solutions.

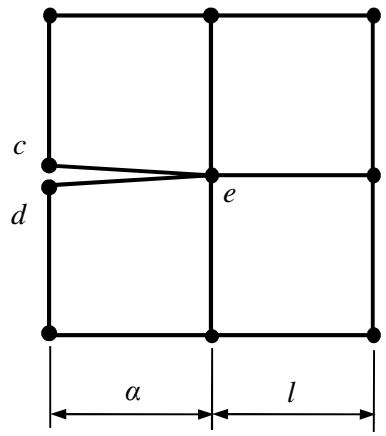

Fig. 5.3. Fintie elements and nodes at the crack tip

In the current work, the computation of strain energy release rate based on the virtual crack closure technique is taken into account by applying to the beamfiniteelement using the layerwise theory. Since the layerwise beam model is able to

describe the full 2-D behaviors of the beam structure in terms of the longitudinal and transverse displacements, the virtual crack closure method is completely applicable to give the nodal forces and displacements that are required to compute the strain energy release rate given in (5.5)

The displacement fields in the layer-wise beam model are approximated by the quadratic shape functions, and following Raju[83], the strain energy release rate can be accordingly computed as

$$G_I = -\frac{1}{2\Delta}\left[F_{yi}(v_m - v_{m'}) + F_{yj}(v_n - v_{n'}) \right] \tag{5.6a}$$

$$G_{II} = -\frac{1}{2\Delta}\left[F_{xi}(u_m - u_{m'}) + F_{xj}(u_n - u_{n'}) \right] \tag{5.6b}$$

where G_I and G_{II} indicate the strain energy release rate for the fracture Mode I and II, respectively, Δ is the length of the beam element at the crack tip, F_{yi} and F_{xi} are the forces in y and x direction, respectively at the node i, and v_m and u_m are the nodal displacements in y and x direction, respectively at the node m(see Fig. 5.4). From the formula given in (5.6a)-(5.6b), the accuracy of the strain energy release rate appears to be dependent upon the size of the element as well as the accuracy of the nodal forces and displacements. The dependency of the numerical values on the element size will be examined in the following section through some examples.

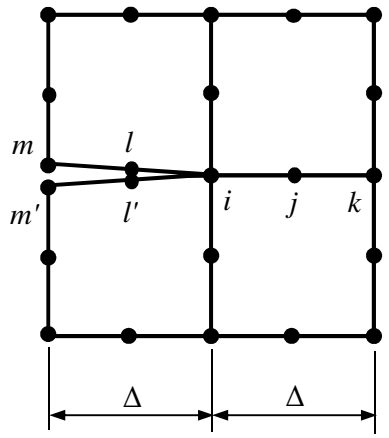

Fig. 5.4. 8-node parabolic element (Raju, 1987)

5.3 Numerical Examples for Verification

5.3.1 Single Edge Crack

The single edge crack model is depicted in Fig. 5.5 and the length of the crack a is varying in the computation from $0.2b$ to $1.0b$ while b and L are fixed to be same ($b = L$). As for the mesh using the layer-wise beam finite element model, the smallest elements are placed at the crack tip and the thickness of the layer which includes the crack face is set as same as the smallest element length. The thickness of the layers and the size of the elements are varying in the computation in order to see how the numerical values are dependent on the mesh size. The quadratic shape functions are used for each beam element and also the quadratic approximation functions are used for computing the coefficients through the thickness [14].

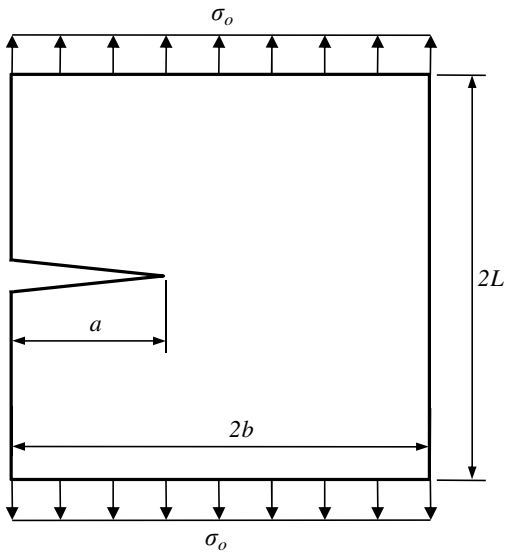

Fig. 5.5. Single edge crack model

Table 5.1 compares the results obtained from layer-wise beam finite element model with the ones available from the literature. The strain energy release rate has been converted to the stress intensity factor using equation (5.2), and again the stress intensity factor is nondimensionalized.

Comparing to the analytical solutions of Gross and Bowie[84], the stress intensity factors computed based on the virtual crack closure technique using the layer-wise beam model shows only less than 6% or 8% of discrepancy, for all cases of the element size at the crack tip. Overall, the numerical values of the present method tend to overestimate slightly more than the analytical values except for the case of $a/b = 0.2$.

Further, the sensitivity of the stress intensity factor to the finite element size does not appear significant.

Table 5.1. Finite width corrections of stress intensity factor $\frac{K}{\sigma_0\sqrt{\pi a}}$ for a single edge crack

a/b	Virtual Crack Closure Using Layerwise Beam FEM					Gross	Bowie
	Δ=0.1b	Δ=0.05b	Δ=0.02b	Δ=0.01b	Δ=0.001b		
0.2	1.14	1.16	1.17	1.17	1.17	1.19	1.20
0.4	1.39	1.40	1.41	1.41	1.42	1.37	1.37
0.6	1.73	1.75	1.76	1.76	1.76	1.66	1.68
0.8	2.18	2.20	2.21	2.21	2.21	2.12	2.14
1.0	2.82	2.84	2.86	2.86	2.86	2.82	2.86

The numerical values show a good agreement with the analytical values within 5% of error even with the same length for all elements including the crack tip region. However the relationship between the crack tip element length (Δ) with the crack length ratio to the total length of the model (a/b) is worth studying in order to find a criterion for constructing the meshes. When the ratio of $\Delta/(a/b)$ is around 0.1, the computed values show a good agreement with the results from the literature. Hence, the effort to build extremely fine meshes does not seem to be required to obtain satisfying values of the strain energy release rate or the stress intensity factor.

5.3.2 Center Crack

Fig. 5.6 shows the center crack model of a finite strip under plane stress state. In a similar way to the single edge crack model, the length of the crack a is varying in the computation from $0.1b$ to $0.5b$ while b and L are fixed to be same (b=L).

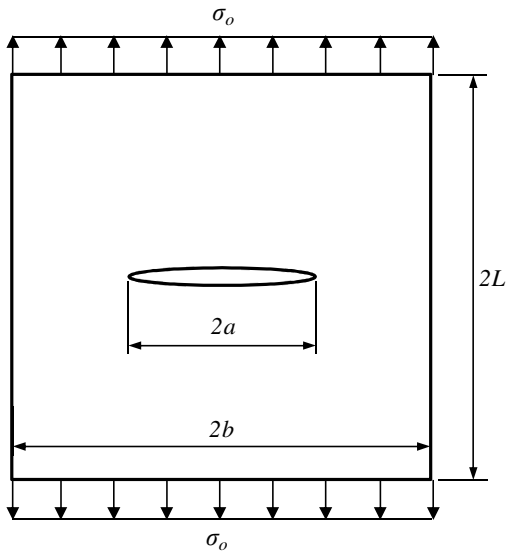

Fig. 5.6. Center crack model

Basically the same idea for building meshes as the single edge crack model is employed for the center crack model.

Comparison between the stress intensity factors computed from layer-wise beam finite element model with the ones available from the literature [84] is presented in Table 5.2.

The analytical solutions for the center crack in a strip with infinitely long L are found in most of the works and the solution of Isida was tabulated in Table 5.2 as the representative analytical solution. As for an finite L, Hellen [82] obtained the numerical solutions for the case of $b = L$ based on the virtual crack extension method and his solutions are compared in Table 5.2. The present analysis shows underestimated values relative to the solutions of Hellen by about 4 to 8% except for a/b=0.2. Considering that

Table 5.2. Finite width corrections of stress intensity factor $\frac{K}{\sigma_0\sqrt{\pi a}}$ for a center crack

a/b	Virtual Crack Closure Using Layerwise Beam FEM					Hellen	Isida
	Δ=0.1b	Δ=0.05b	Δ=0.02b	Δ=0.01b	Δ=0.001b		
0.1	0.90	0.95	0.96	0.96	0.97	1.02	1.00
0.2	0.98	1.00	1.00	1.00	1.01	1.05	1.03
0.3	1.05	1.06	1.07	1.07	1.07	1.15	1.06
0.4	1.14	1.15	1.16	1.16	1.16	1.21	1.13
0.5	1.25	1.27	1.27	1.27	1.27	1.33	1.27

the numerical solutions in the literature calculated with a different ratio of *L/b* and they are often compared to the analytical solutions which are based on the case of $L \to \infty$, the discrepancy of the present analysis appears to be accurate enough to be used for computing the strain energy release rate or the stress intensity factors. In addition, underestimation of the stress intensity factor using the virtual crack closure technique has been also observed by Raju in his study and his optimized meshes shows about 4% discrepancy [83]. The size of the crack tip elements, again, does not appear to affect the numerical values drastically when the crack tip element size is relatively small enough. In the present study, the optimal size of the crack tip element appears to be $0.1a$ and the smaller element size makes little change in the stress intensity factors.

5.4 Influence of Bending Boundary Conditions

In many practical cases, a bending test of beam structure is conducted under a transverse

load with some boundary conditions. The combination of load type and boundary condition appears to affect the response of delamination analysis under bending loads. Four types of bending tests will be considered to evaluate the influence of boundary conditions on the delamination behavior in the composite laminated beams. The beams are composed of $[90_m / 0_n]_S$ cross ply laminates and a interlaminar crack with length a is assumed to exist at the tip of pre-existing transverse crack (see Fig. 5.7).

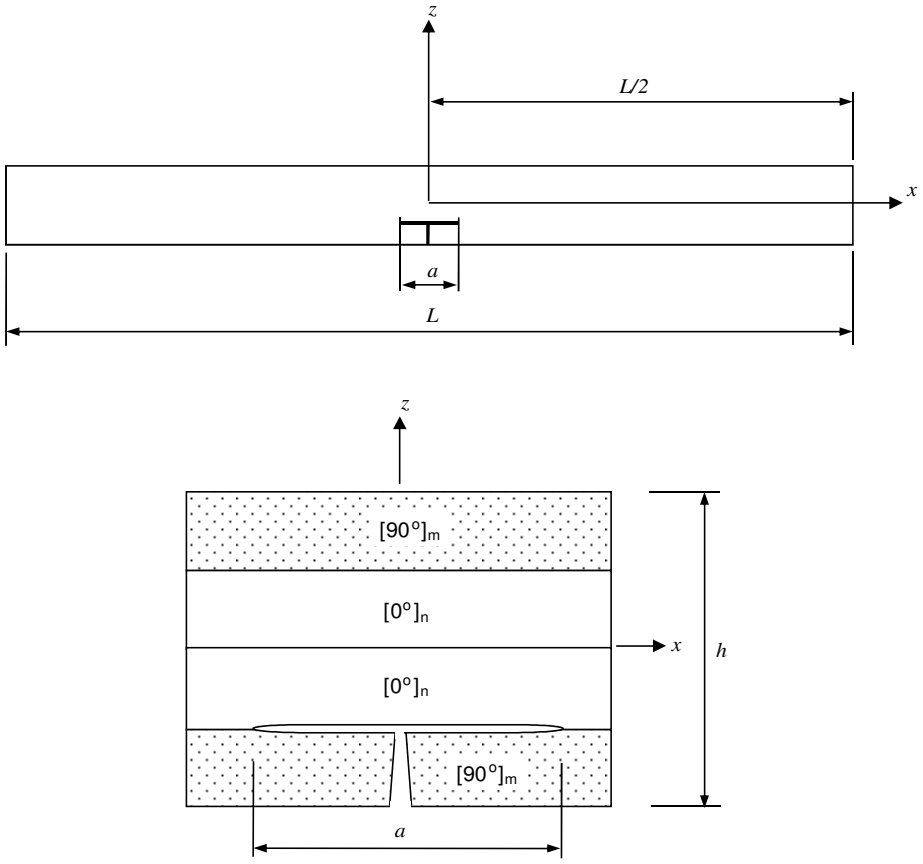

Fig. 5.7.. Laminated beam with a delamination originated from a transverse crack

The single transverse crack is assumed to be aligned with the z-axis in the 90-degree layers on the tensile side of the beam and it is also assumed to run through the width of the beam completely. As shown in Fig. 5.6, an interlaminar crack at the interface of the cracked 90-degree layer and the adjacent 0-degree layer is assumed to locate symmetrically about the z-axis. One can expect to simulate a crack similar to the delamination originated from a free edge of the beam under bending.

Four different boundary conditions are considered to impose bending loads on the specimen: a) 3-point bending , b) clamped-ends with center load, c) distributed load with simply supported ends and d) 4-point bending (Fig. 5.8). The applied load is given to each case of boundary condition in such a way that the maximum bending moment along the beam can be the same for all four boundary conditions. For the lay-ups of $[90_2/0_2]_S$ with the thickness of one ply being 0.5mm, the total thickness of the beam, h is 4mm and the length of the beam, L is 150mm. The moment arm S for the case of 4-point bending is given as 5mm.

The material properties of the composite are taken from the reference [51] and listed as follows

$$E_1 = 156\,\text{GPa} \qquad E_2 = E_3 = 9.09\,\text{GPa}$$

$$G_{12} = G_{13} = 6.96\,\text{GPa} \qquad G_{23} = 3.24\,\text{GPa}$$

$$\nu_{12} = \nu_{13} = 0.228 \qquad \nu_{23} = 0.4\,.$$

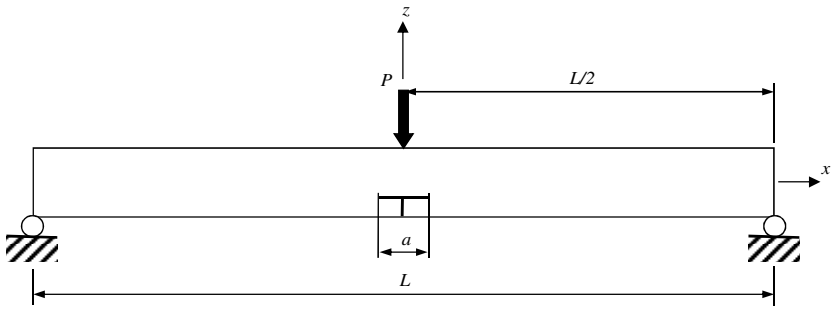

(a)

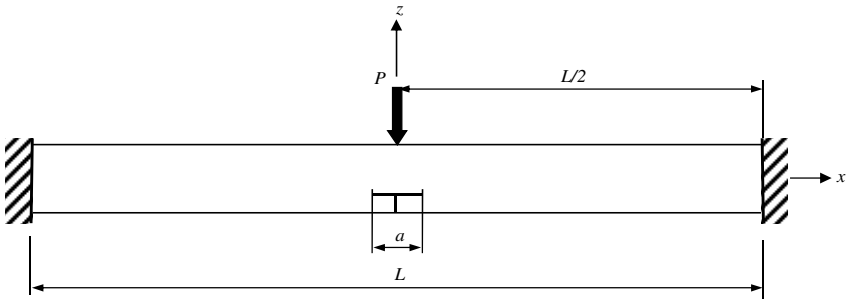

(b)

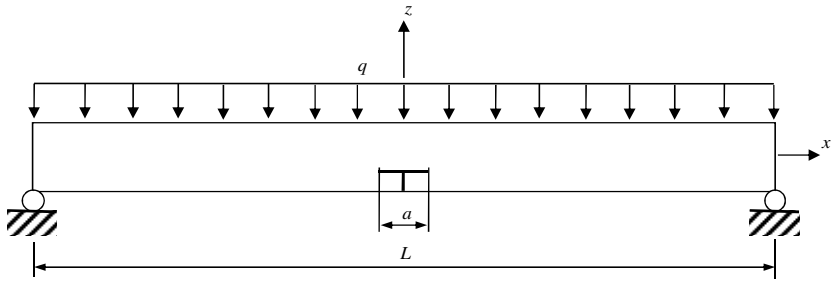

(c)

Fig. 5.8. Four boundary conditions (a) 3-point bending (b) clamped-ends with center load (c) distributed load with simply supported ends (d) 4-point bending

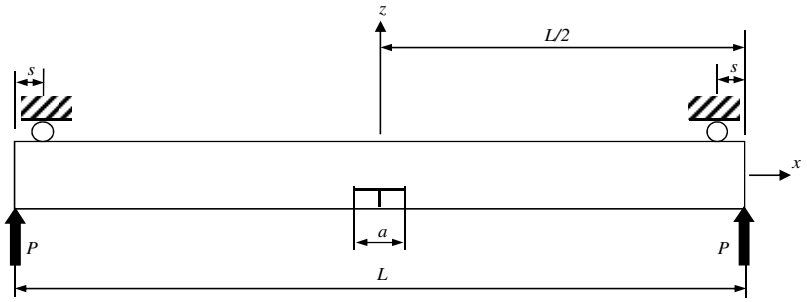

(d)

Fig. 5.8. (Continued)

The numerical computation to obtain the strain energy release rate for each boundary condition is performed using the LWTDEL code, which has been developed based on the layer-wise beam theory including delamination. In the numerical model, half of the beam is modeled using the geometric symmetry and the assumption of symmetric crack growth.

5.4.1 Role of Bending Moment

Fig. 5.9 presents the strain energy release rate versus the delamination length for each boundary condition. Unlike the axial extension test in which the strain energy release rate usually increases and approaches an asymptotic value as the delamination length increases[27, 36, 38, 41], the strain energy release rate shows different patterns in the bending test according to the boundary condition types.

For the case of distributed load with simply supported ends and 3-point bending, the strain energy release rate keeps decreasing as the delamination length grows. For the

case of clamped ends, the strain energy decreases until the delamination length reaches a little less than half of the beam length, then it starts increases again. Only for the case of 4-point bending, the strain energy remains almost constant except for the very short delamination length. Based on this observation, the length of the delamination crack does not seem to directly contribute to the variation of strain energy release rate. Rather, the strain energy release rate is governed by the location of the delamination crack tip at which the amount of bending moment is determined by the boundary condition.

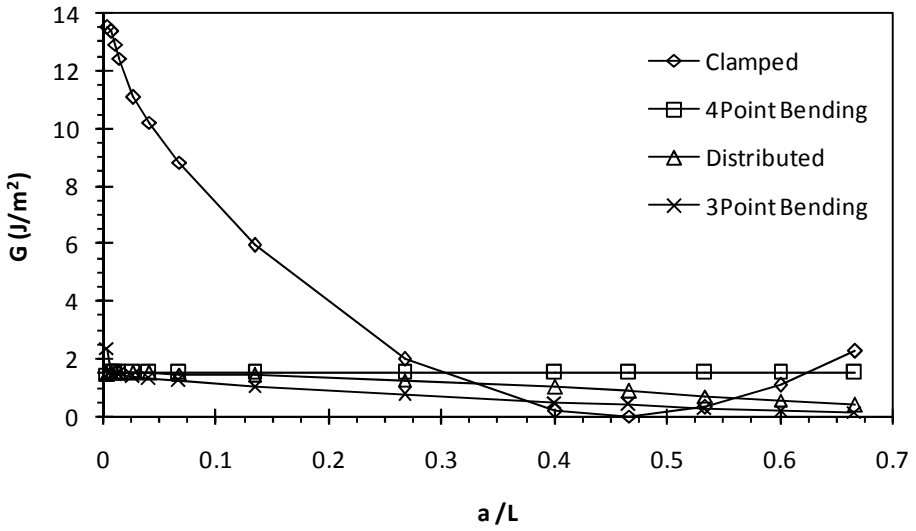

Fig. 5.9. Strain energy release rate versus nondimensional delamination length

From Fig. 5.9, a fact that the strain energy curve pattern resembles the bending moment along the beam can be found. As the crack tip moves from the beam center toward the beam ends, the bending moment at the position of the crack tip varies and the

strain energy release rate is varying proportionally to the bending moment. In particular, the bending moment for the case of four-point bending is uniform in between the inner supports, which gives the uniform strain energy release rate throughout the range of delamination length. In that perspective, the four-point bending test can be seen as a method to provide the boundary condition in which the delamination under bending can be analyzed without the boundary effect. Another interesting observation in Fig. 5.9 is that the maximum value of the strain energy release rate obtained for the clamped ends is significantly larger than those of other three boundary conditions even though the vertical loads are applied so that the maximum bending moment can be the same for all four boundary conditions.

5.4.2 Fracture Modes

Mixture of fracture Mode I and II in delamination are observed and analyzed in the literature[26, 27, 43]. In order to make a distinction between the two modes, the strain energy components G_I and G_{II} are separately computed at a crack tip and then the total strain energy release rate G is obtained by the summation of G_I and G_{II} as follows.

$$G = G_I + G_{II} . \tag{5.3}$$

Depending on the configuration of the laminate lay-ups or the loading conditions, a predominant mode is considered as the main mechanism to drive the delamination in the situation. More often than not, the total strain energy release rate is replaced by the

predominant mode's strain energy release rate[37, 43, 49]. This simplification can be made to save the computational effort when the contribution of the other mode is negligibly small. To investigate the possibility of applying this simplification to the bending case, the following results are discussed.

For the four boundary conditions given in Fig. 5.8, the fraction of the fracture modes to the total strain energy release rate is quantified in Fig. 5.10. As seen in Fig. 5.10, the fracture Mode I appears to be the main mechanism of the delamination for the given situation. Except for the case of clamped ends, G_I commonly takes up about 78% of the total strain energy release rate regardless of the delamination length. The remaining 22% of the total strain energy release rate can be seen as a contribution of the fracture Mode II. In this case, whether G_{II} is negligible is questionable. The error of 22% in evaluating the total strain energy release rate to predict the growth of delamination can result in a considerable underestimation. Thus, the mixture of Mode I and II should be taken into account to compute G at the delamination crack tip under the given bending loads. A similar observation has been made by Murri and Huynn[49]. In their work, they tried to find the critical strain energy release rate at which the growth of delamination occurs, under different bending test conditions. However, they failed to relate the strain energy release rate to the bending moment. More importantly, the contribution of fracture Mode II to the total strain energy release rate was underestimated and they argued that the critical strain energy release rate could be regarded as the value of Mode I.

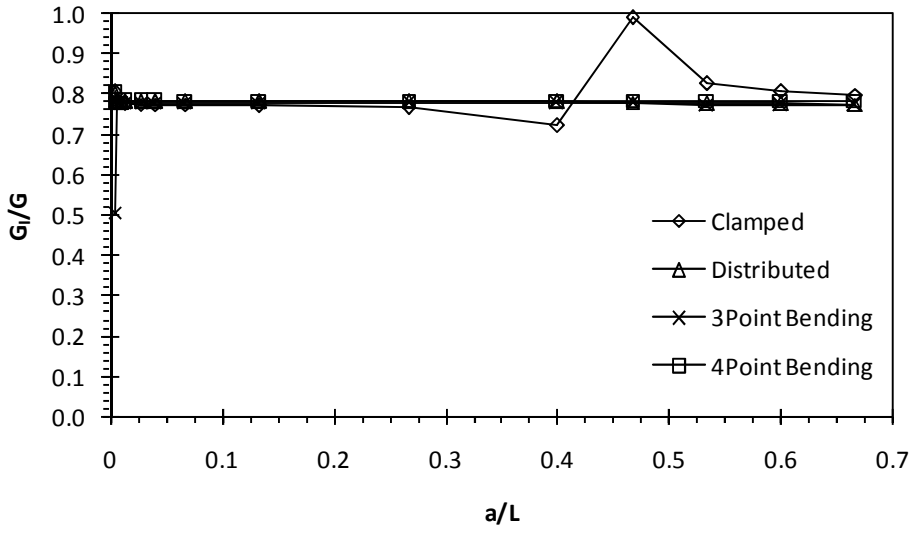

(a)

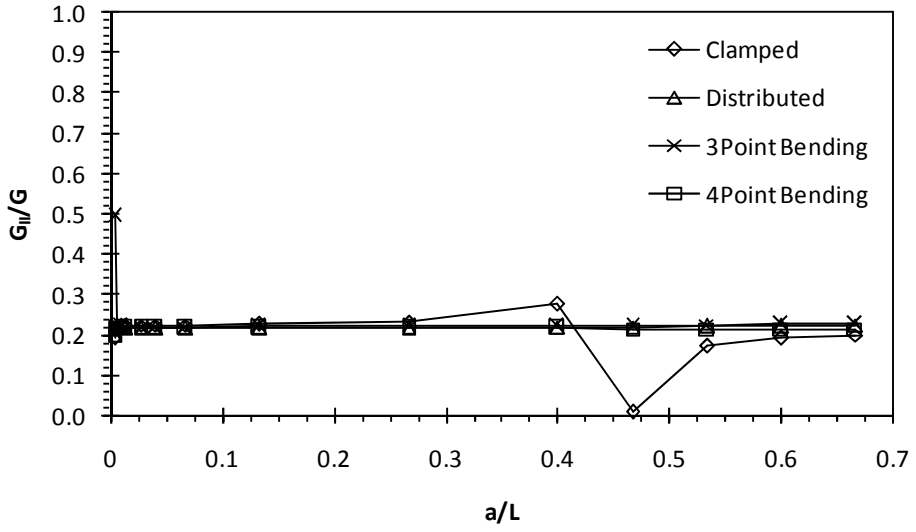

(b)

Fig. 5.10. Strain energy release rate fraction of (a) Mode I (b) Mode II

5.5 Geometric Nonlinearity

In most of the studies related to the delamination damage, geometric nonlinearity in the specimen is neglected. The effect of the von Kármán type nonlinear strain field will be examined in this section by comparing the analysis based on the conventional linear strain fields. Since the computer code LWTDEL has been developed in a way that the nonlinear strain fields can be included in the delamination analysis, the influence of the geometric nonlinearity on the interlaminar cracks will be considered. In this study, the linear analysis refers to the numerical analysis based on the linear strain fields and the nonlinear analysis refers to the one based on the von Kármán type nonlinear strain fields. Also, as seen in the previous section, the four-point bending appears to be the boundary condition that can simulate the behavior of delaminated beam under the pure bending load. Based on these ideas, the lay-ups of $[90_2/0_2]_S$ are employed to model the laminated beams and the pre-existing interlaminar crack with length a is assumed at the interface of 90-degree and 0-degree on the tension side.

5.5.1 Delamination Growth

The change of strain energy release rate is presented in Fig. 5.11 as the delamination length increases. The solid lines indicate the values computed from linear analysis and the dotted lines indicate the results from nonlinear analysis. As seen in the figure, the difference between the linear and nonlinear analysis can be hardly found. Taking into account the von Kármán type nonlinearity in the delamination growth has little influence on the strain energy release rate G for the given numerical examples.

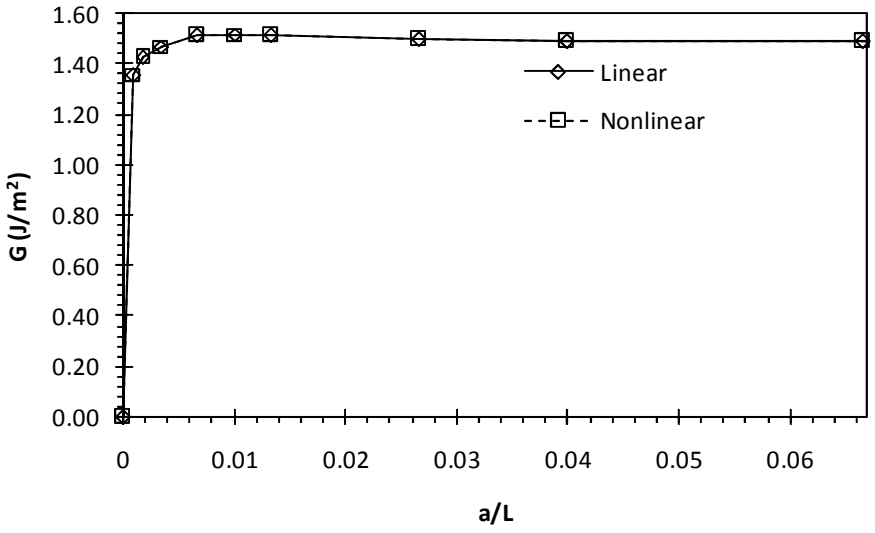

Fig. 5.11. Strain energy release rate VS delamination growth under pure bending

When the delamination length a is less than $0.05L$, the strain energy release rate sharply decreases until it reaches a certain bounded value. The interlaminar crack length 0.05L is also approximately same as twice the thickness of one ply. Wang et al.[38] introduced the concept of effective flaw for analysis of the delamination onset in the axial tensile test and they made use of the asymptotic value that the strain energy release rate reaches, to determine the minimum size of the embedded delamination crack as the effective flaw in the analysis. Wang *et al.* [27] suggested twice the ply thickness as the size of effective flaw. The size of crack at which the strain energy release rate reaches a certain asymptotic value coincides with the present result under the bending load.

The primary fracture mode leading the delamination growth can be found in Fig. 5.12 displaying the strain energy release rate fraction of Mode I and Mode II. Mode I has been identified as the primary fracture mode responsible for the delamination with

transverse crack in 90-degree layer in the previous section. The strain energy release rate fractions remain constant even the interlaminar crack runs more than half of the total beam length.

In order to quantify the role of nonlinearity, if any, developed in the laminated beam under bending loads, an attempt is made. The strain energy release rate ratios are defined as the ratios of the strain energy release rate from the linear analysis to the strain energy release rate from the nonlinear analysis. That is

$$R = \frac{G^N}{G^L} \tag{5.4a}$$

$$R_I = \frac{G_I^N}{G_I^L} \tag{5.4b}$$

$$R_{II} = \frac{G_{II}^N}{G_{II}^L} \tag{5.4c}$$

where the superscript L and N stand for the values from the linear and the nonlinear analysis, respectively.

The strain energy release rate ratios for the two cases of delamination are plotted in Fig. 5.13, as a function of delamination length. The strain energy release rate ratio of the primary fracture mode is decreasing as the delamination length advances. On the other hand, the strain energy release rate ratio of the other fracture mode is increasing while the total strain energy release rate ratio is kept almost unchanged. This result implies that the nonlinearity is developed in the bending beam as the delamination crack

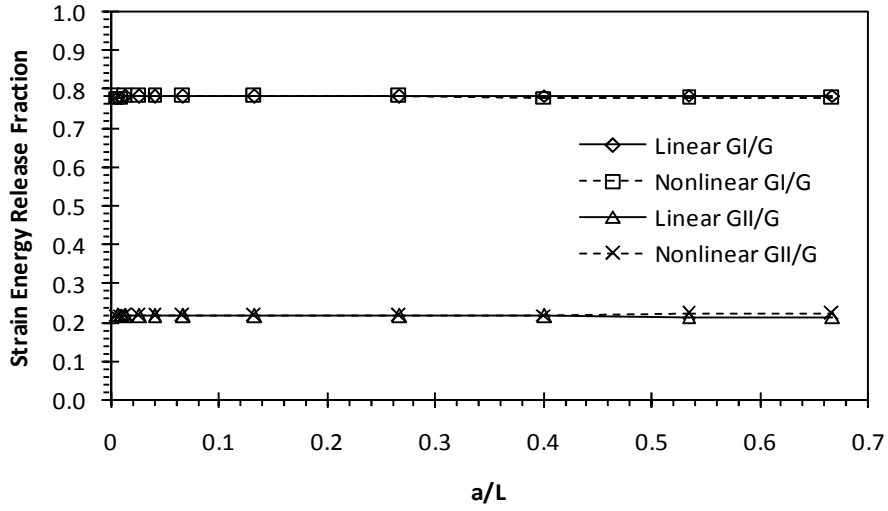

Fig. 5.12. Strain energy release rate fraction VS delamination growth under pure bending

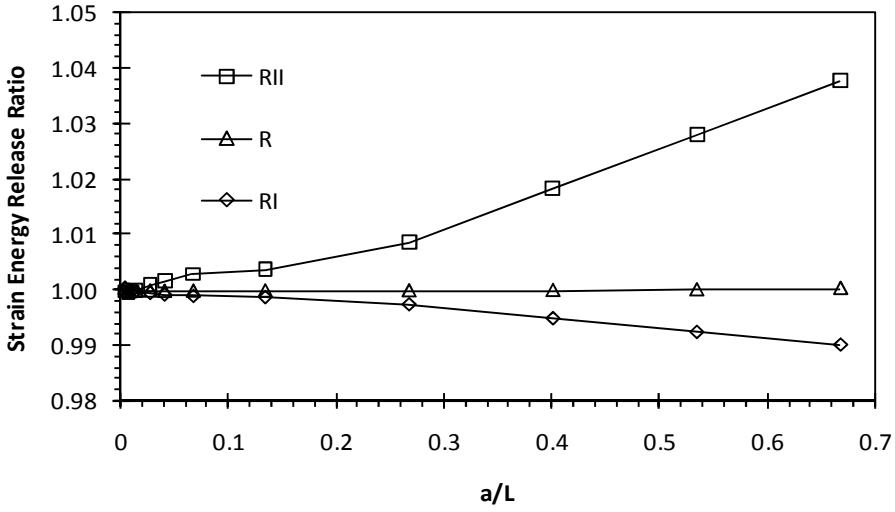

Fig. 5.13. Strain energy release rate ratio VS delamination growth under pure bending

grows, even if the change in the strain energy release rate due to nonlinearity is less than 5% for each fracture mode. However, the total strain energy release rate is found to be nearly unchanged for the effect of nonlinearity during the delamination growth.

5.5.2 Applied Bending Moment

Fig. 5.14 presents the relationship between the strain energy release rate and the applied bending moment when the interlaminar crack length is fixed. Again, the difference between the linear and nonlinear analysis appear negligible even when the strain energy release rate reaches a considerably high value. The strain energy release rate G is not much affected by including the nonlinearity throughout the whole range of the applied bending moment. This result can be related to the previous observation that the total strain energy release rate is little changed by the nonlinearity developed in the beam even though the strain energy release rate ratios of Mode I and Mode II are slightly changed. In that regard, the general perception that the delamination analysis is performed using the linear elasticity theory can be justified.

Fig. 5.15 gives information about the main fracture mode to drive the delamination as increasing the applied bending moment by displaying the strain energy release rate fraction of Mode I and Mode II. As seen previously, the primary fracture mode for the delamination is found to be Mode I throughout the range of applied bending moment for a fixed delamination length a=10mm.

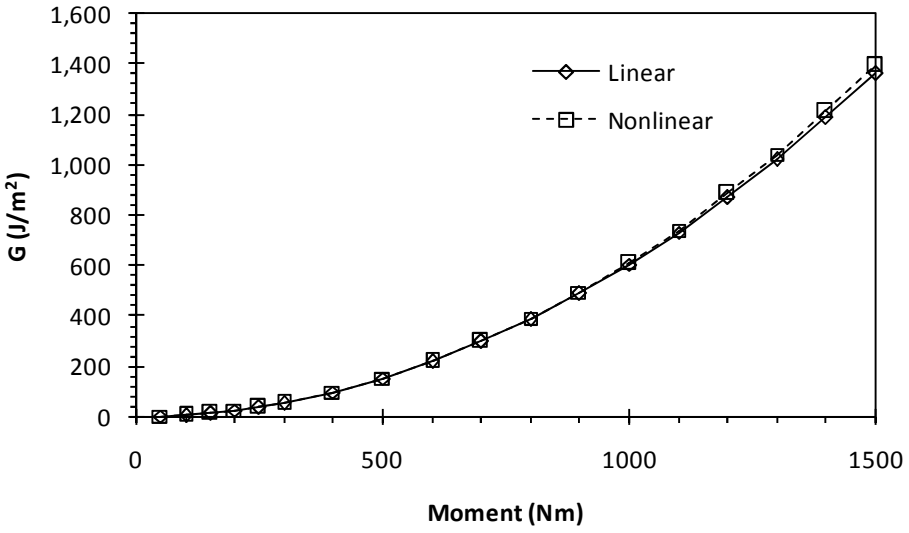

Fig. 5.14. Strain energy release rate VS applied moment under pure bending (*a*=10mm)

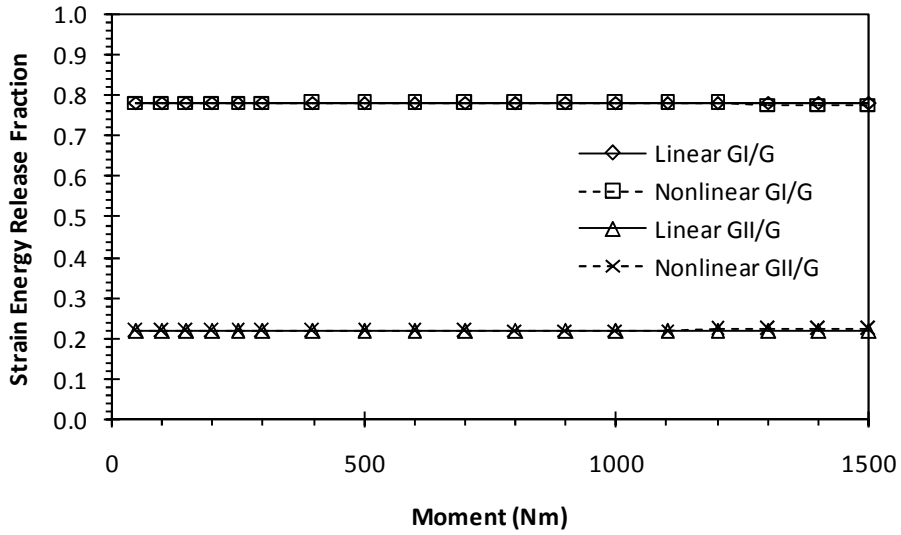

Fig. 5.15. Strain energy release rate fraction VS applied moment crack under pure bending (*a*=10mm)

The contribution of the minor fracture mode to the whole delamination mechanism is not negligible. It deserves an attention that the strain energy release rate fraction is nearly constant for any value of applied bending moment if the delamination length is fixed.

The strain energy release rate ratio is plotted in Fig. 5.16. Even though the change is small, it can be noticed that the strain energy release rate ratios increase as more bending moment is applied to the beam. This is due to the fact that the nodal force at the crack tip is increasing as the nonlinearity is introduced in the stiffness. It is worth remarking that the minor fracture mode, i.e. Mode II, shows more increase than the primary fracture mode, i.e. Mode I, as the applied moment increases.

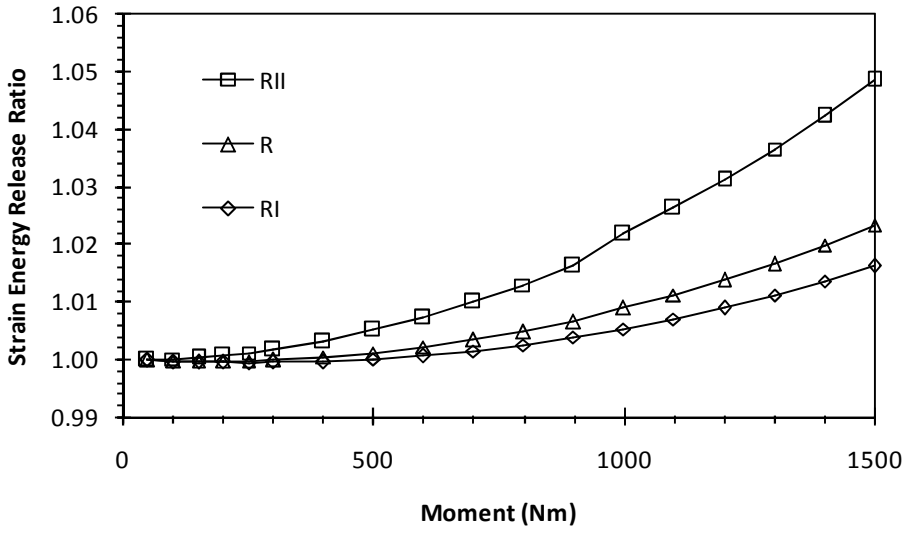

Fig. 5.16. Strain energy release rate ratio VS applied moment under pure bending (*a*=10mm)

Overall, very little geometric nonlinearity in the beam is developed under the given bending load until the strain energy release rate reaches a very high value. The material used in this analysis is T300/976 graphite-epoxy composite and its critical strain energy release rate is reported in the range of $87.5\,J/m^2$ (for Mode I) to $282.6\,J/m^2$ (for Mode II) [54]. Although the strain energy release rate computed is well above these values, the nonlinear analysis shows almost the same G values as the linear analysis. Therefore, the interlaminar crack under a pure bending load is expected to grow before the applied bending moment gets large enough for the significant geometric nonlinearity to be prominent.

CHAPTER VI

DELAMINATION ORIGINATED FROM TRANSVERSE CRACKS

6.1. Outline

The interactions between the interlaminar cracks and the transverse cracks are examined for a cross-ply laminate with various lay-ups under bending loads. The exemplary cross-ply configurations considered here is $[90_m / 0_n]_S$ where $m+n=4$ and $m,n=1,2,3$. One ply thickness, i.e. for m or $n=1$, is given $0.1mm$ in the numerical models throughout the analyses. The material is T300/976 graphite epoxy composite and its material properties used in the numerical computation are given, following the reference [54], by

$$E_1 = 121.3\,\text{GPa} \qquad E_2 = E_3 = 9.72\,\text{GPa}$$

$$G_{12} = G_{13} = 5.58\,\text{GPa} \qquad G_{23} = 3.45\,\text{GPa}$$

$$\nu_{12} = \nu_{13} = 0.29 \qquad \nu_{23} = 0.4\,.$$

The outer layers are 90-degree plies in $[90_m / 0_n]_S$ and only one side of the 90-degree plies in tensile state is assumed to develop the uniformly distributed transverse cracks in it. The interlaminar crack at the interface of the cracked 90-degree layer and the adjacent 0-degree layer is assumed to be symmetric about the transverse crack. Further, the delamination cracks are also assumed to have the same length at each transverse crack tip so that a unit cell can be considered in the model (see Fig. 6.1).

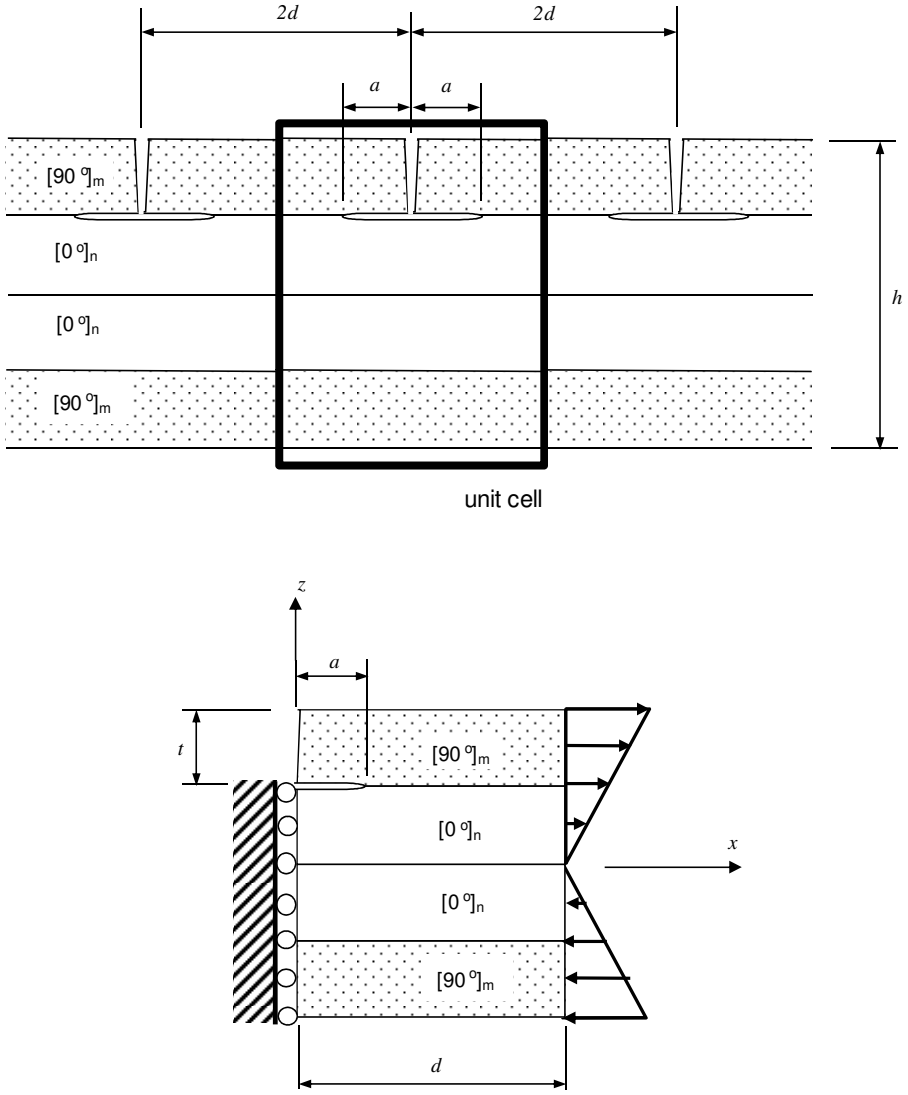

Fig. 6.1. Laminated beam of $[90_m / 0_n]_S$ lay-up with delamination originated from uniformly distributed transverse cracks under plane strain bending

Only half of the unit cell is modeled using the geometric symmetry and the plane strain bending load is applied as depicted in Fig. 6.1. The thickness of the transversely cracked 90-degree layer is denoted by *t*. The magnitude of the maximum strain value at the top and bottom surface of the laminate is set to 1% in all computation for each different lay-up.

The finite element code LWTDEL based on the layer-wise beam theory is used to build the numerical model and to investigate the influence of the two damage modes on each other.

6.2. Influence of Transverse Cracking on Delamination

6.2.1. Delamination Length, Transverse Crack Density and 90-degree Plies

The strain energy release rates, G for various transverse crack densities, $t/2d$ are presented in Fig. 6.2 through Fig. 6.4 as the dimensionless delamination length, $2a/t$ increases. When the delamination length relative to the cracked 90-degree ply's thickness is very short, the strain energy release rate increases until it reaches a certain maximum value. Once the maximum values are achieved, the strain energy release rates start decreasing as the delamination length increases. It can be noted that the decreasing slope of G curve after its maximum value is varying according to the transverse crack density, $t/2d$ as well as the number of 90 and 0-egree plies. When the dimensionless crack density $t/2d$ is low, the strain energy release rate is not significantly affected by the growing delamination length after G reaches the maximum, even though the magnitude of the strain energy release rate can be recognized to be decreasing slowly.

On the other hand, the strain energy release rate shows a rapid decease as soon as it gets to the maximum at the high crack densities. Further, the maximum value of strain energy release rate itself decreases as the transverse crack density becomes higher.

A physical meaning of this varying strain energy release rate can be found regarding the delamination crack growth hindered by the transverse crack density. In other words, it becomes harder for the interlaminar crack to grow further as the crack density increases or the delamination length approaches the transverse crack spacing.

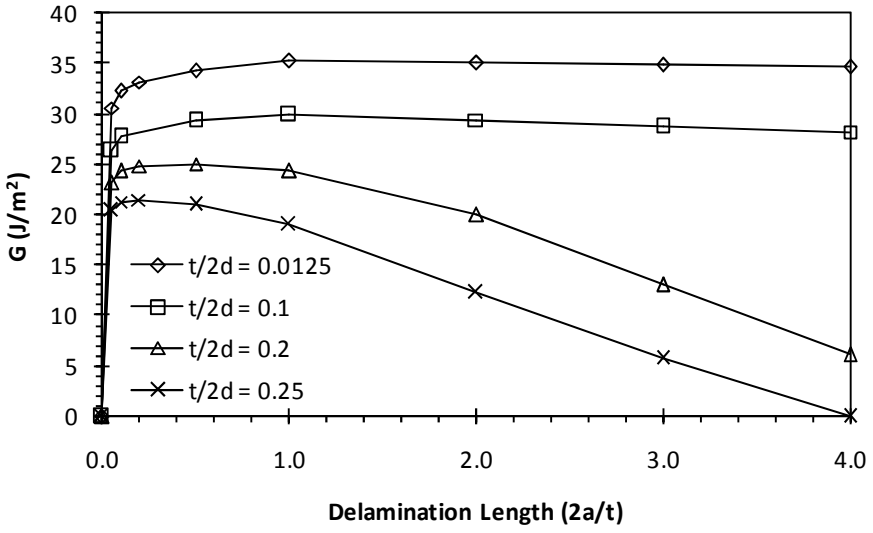

Fig. 6.2. Strain energy release rate VS delamination length ($2a/t$) for $[90_1 / 0_3]_S$

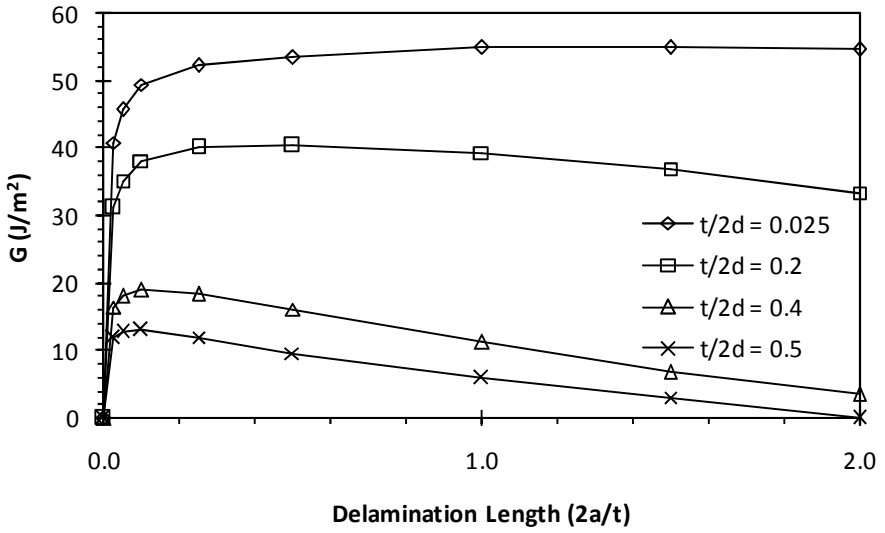

Fig. 6.3. Strain energy release rate VS delamination length (2*a/t*) for $[90_2 / 0_2]_S$

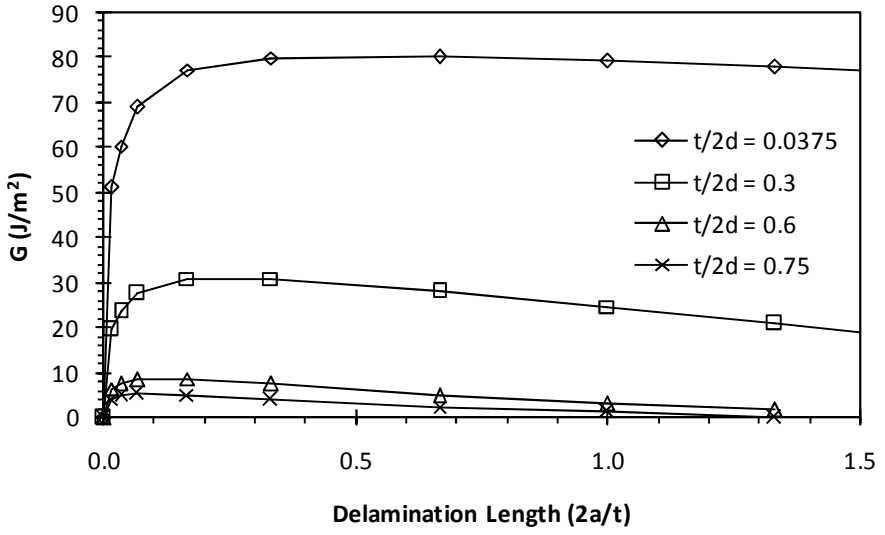

Fig. 6.4. Strain energy release rate VS delamination length (2*a/t*) for $[90_3 / 0_1]_S$

Since the strain energy release rate computed here indicates the energy required for the delamination crack to grow, the delamination is unlikely to progress when the magnitude of the strain energy release rate is below the critical value. From that perspective, the delamination crack is expected to occur and grow more easily at low transverse crack density. This consequence can be found under the tensile load condtion[36].

It should be also noted that the early stage of delamination growth, i.e. until the strain energy release rate reaches a maximum value, at the low transverse crack density shows a good agreement with the result of axial tension tests[27, 38]. Wang et al.[38] performed the axial tension test and they reported that the strain energy release rate reached an asymptotic value. Wang et al. [27] also observed the asymptotic G value was achieved at about twice the ply thickness and they suggested this characteristic delamination length should be the size of effective flaw to predict the delamination growth. In the present examples with the uniformly distributed transverse cracks under the bending load, however, the characteristic delamination length appears to be dependent upon the crack density and the lay-up configuration.

To demonstrate the effect of 90-degree plies, the strain energy release rates for the different lay-up configuration are presented in Fig. 6.5 and 6.6 as the delamination length, a/d increases under the same applied plane bending strain. Note that the delamination length is displayed in terms of the ratio to the crack spacing because the thickness of the cracked 90-degree plies are varying.

As shown in Fig. 6.5, the thicker the 90-degree layer is, the higher the maximum

strain energy release rate is marked when the transverse crack density is low ($1/2d = 0.125/mm$). However, the strain energy release rate is showing a rapider decrease as the delamination progresses when the number of 90-degree plies increases in the laminate lay-ups. Especially, the strain energy release rate for $[90_3/0_1]_S$ configuration becomes lower than that of $[90_2/0_2]_S$ after the interlaminar crack grows over a certain length. Thus, the delamination is expected to grow easily when the more 90-dgree plies compose the laminate for a low crack density until the delamination crack reaches a certain length.

Fig. 6.6 displays a contrasting result for a high transverse crack density, $1/2d = 2.5/mm$. The strain energy release rate of the thicker 90-degree plies is lower, which indicates that it is required more bending strain in order for the delamination to grow further when the crack density is high. The strain energy release rate is consistently showing a lower value when the number of 90-degree plies increases throughout the growing delamination length.

To compare the delamination growth under the several chosen crack densities with three different lay-up configurations, the strain energy release rates are depicted in Fig. 6.7 through 6.9. It can be seen that the strain energy release rate is strongly depending on the thickness of 90-degree ply even for the same transverse crack density. When the crack density is low, the strain energy release rate is higher than that of a high crack density case for all configurations of lay-ups, which means that the interlaminar crack is more likely to grow when the crack density is low.

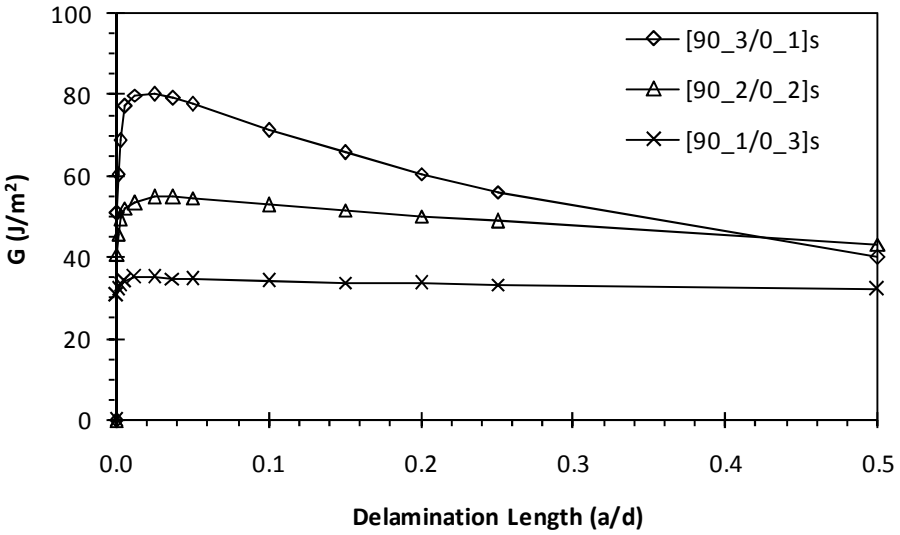

Fig. 6.5. Strain energy release rate VS delamination length for various lay-ups at low crack density ($1/2d = 0.125/mm$)

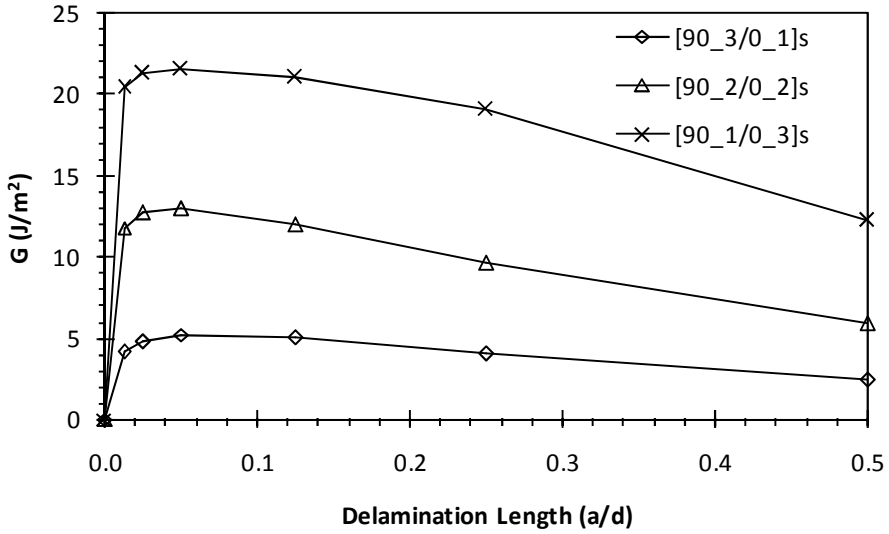

Fig. 6.6. Strain energy release rate VS delamination length for various lay-ups at high crack density ($1/2d = 2.5/mm$)

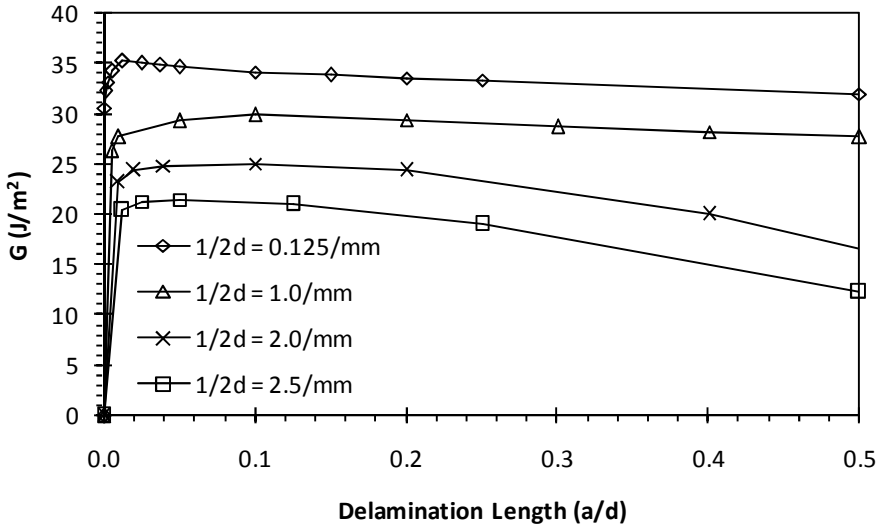

Fig. 6.7. Strain energy release rate VS delamination length (*a/d*) for $[90_1/0_3]_S$

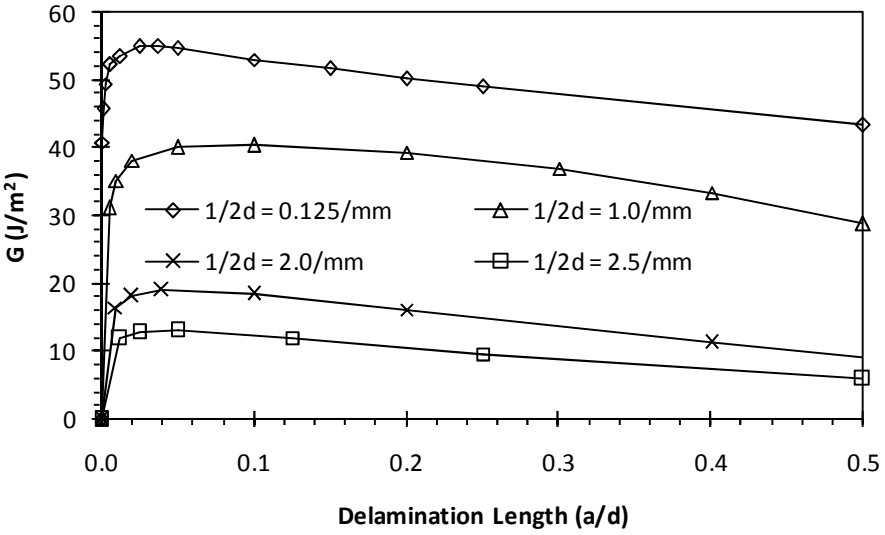

Fig. 6.8. Strain energy release rate VS delamination length (*a/d*) for $[90_2/0_2]_S$

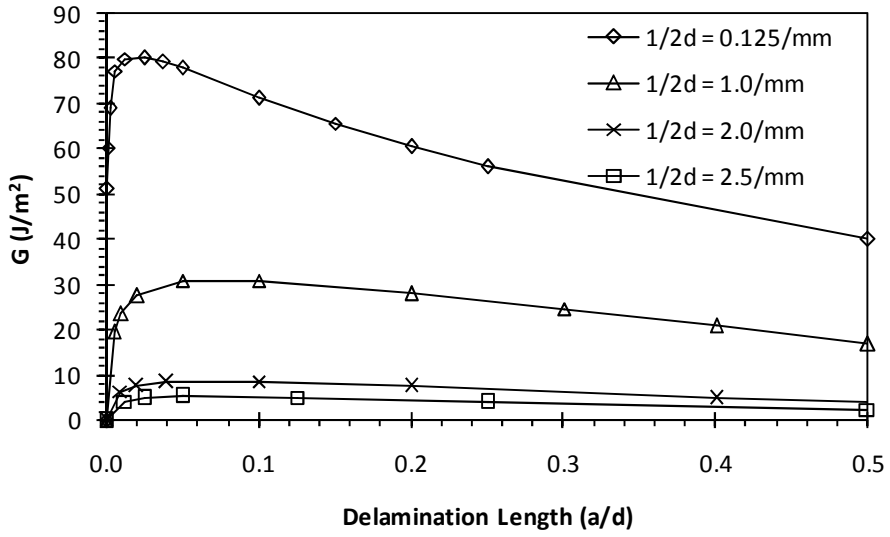

Fig. 6.9. Strain energy release rate VS delamination length (*a/d*) for $[90_3/0_1]_S$

6.2.2 Mode Contribution

The fracture modes in delamination are usually mixed under the bending load and the delamination growth is driven by the combination of the fracture modes. Again, Mode I and II are considered for the responsible fracture modes in delamination of the laminated beam. The contribution of Mode I and II is presented in Fig. 6.10 through 6.12 in terms of the crack density. The contribution of each mode is measured by the strain energy release rate fraction of the mode to the total strain energy release rate.

The primary fracture mode responsible for the delamination originated from uniformly distributed transverse cracks is found to be Mode I, when the crack density is low for all three lay-ups of $[90_m/0_n]_S$. The strain energy release rate fraction is nearly constant until the crack density becomes large and after the crack density reaches a

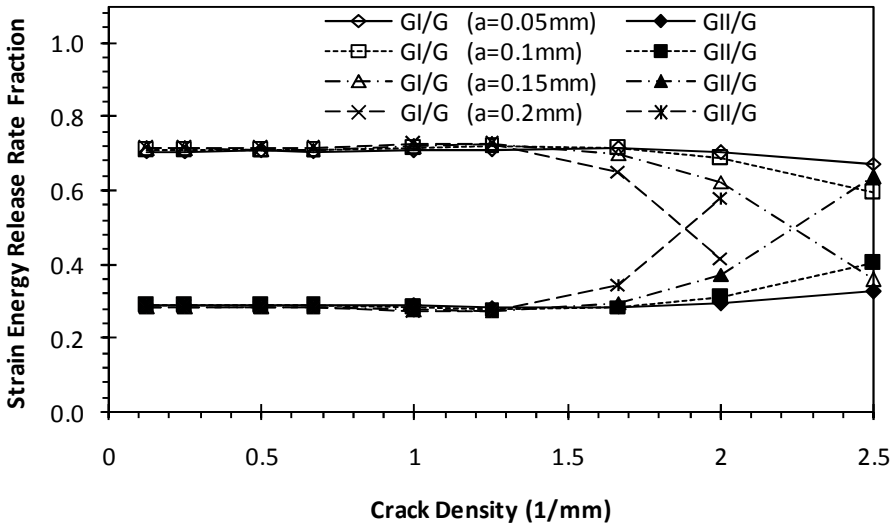

Fig. 6.10. Strain energy release rate fraction VS crack density for $[90_1/0_3]_S$

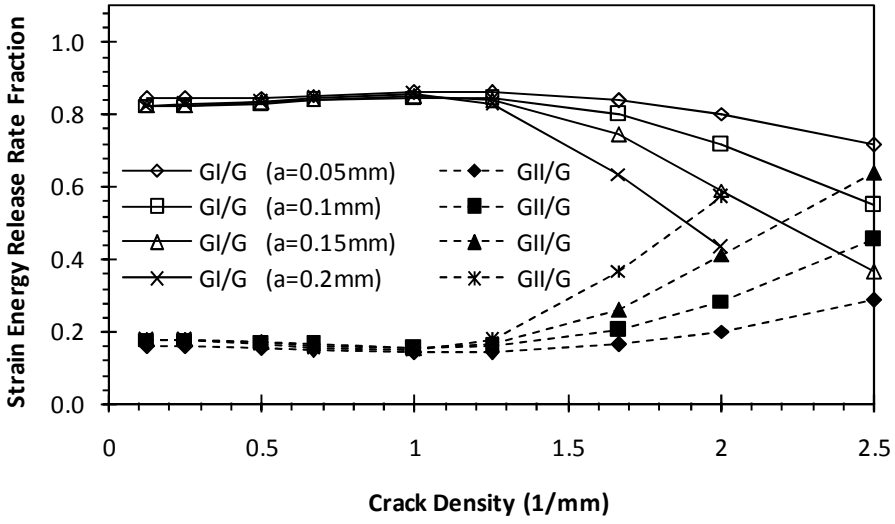

Fig. 6.11. Strain energy release rate fraction VS crack density for $[90_2/0_2]_S$

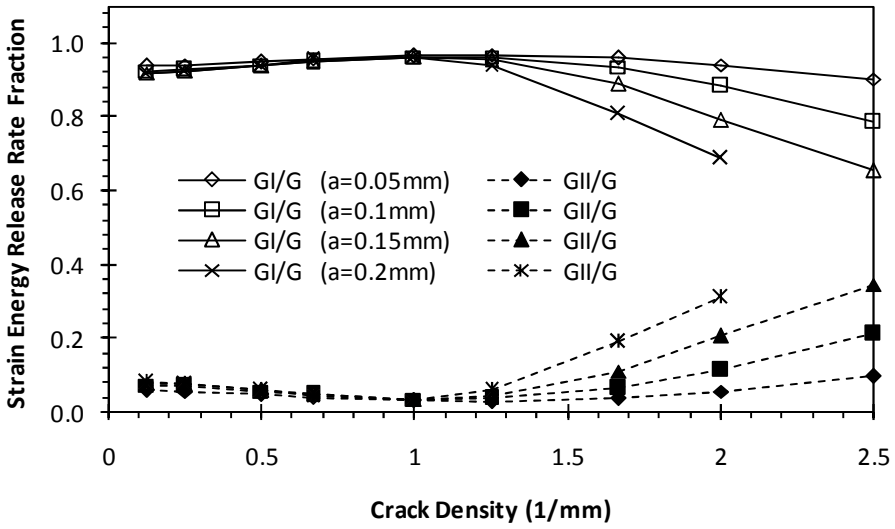

Fig. 6.12. Strain energy release rate fraction VS crack density for $[90_3/0_1]_S$

certain value, the contribution of the fracture mode is changing. The contribution of Mode I appears to be predominant when the crack density is low and the delamination length is short. The contribution of Mode II increases as the crack density increases and the delamination length becomes larger.

The number of 90-degree plies also significantly affects the fracture mode. The more 90-degree plies compose the laminate, the more delamination is led by Mode I. When the crack density is low, the maximum contribution of Mode I is about 73% for $[90_1/0_3]_S$, 85% for $[90_2/0_2]_S$ and 95% for $[90_3/0_1]_S$. That is, when the 90-degree plies becomes thicker and eventually thicker than 0-degree plies, Mode I can be seen as the main fracture mode for the initial delamination growth at a low crack densty and the growth of the initial delamination may be predicted by neglecting Mode II and $G_I \approx G$.

When the length of delamination crack approaches the transverse crack spacing with a high crack density, the contribution of Mode II becomes larger and the delamination can be driven by Mode II according to the laminate lay-up composition and the crack length.

6.3. Influence of Delamination on Transverse Cracking

For the same numerical model depicted in Fig. 6.1, an analysis from a different perspective is attempted to investigate the influence of delamination on transverse cracking in this section.

6.3.1 Transverse Cracking Due to Delamination Growth

The axial normal stress distribution along the outer surface of 90-degree layer in the tensile side over half the transverse cracking space is illustrated for the lay-ups of $[90_1/0_3]_S$ in Fig. 6.13 and Fig. 6.14. The stress shows a constant along the delaminated interface from the transverse crack ($x = 0$) to the interfacial crack tip ($x < a$). The stress shows a sudden drop around the tip of the interfacial crack and it increases after the interfacial crack tip ($x > a$), then it finally tends to show a maximum value at around the half way to the next nearest transverse crack. Over all, it can be found that the stress level of the low crack density is higher than that of the high crack density.

The stress level in between the interfacial crack tips for a short length of delamination crack is higher than that of a long delamination crack. This indicates that the possibility to create a new transverse crack in between the pre-existing adjacent transverse cracks is higher when the delamination length is short. The stress level in

between the pre-existing transverse crack and the interfacial crack tip induced from the initial transverse crack is relatively very low comparing to the stress level at the region ahead of the interfacial crack tip.

Comparing Fig. 6.13 and Fig. 6.14, the stress level in between the interfacial crack tips is found higher when the transverse crack density is lower. This shows a good agreement with the case of uniformly distributed transverse cracks without delamination. That is, a new transverse crack is expected to form easily in between the pre-existing adjacent transverse cracks when the crack density is lower, and the new crack appears to be harder to form as the crack density becomes high (see for example, [9, 13]).

Application of the stress distribution figures shown in Fig. 6.13 and Fig. 6.14 can be made to determine whether a new transverse crack will be formed in the unit cell under a given transverse crack density and a given interfacial crack length. Suppose the axial strength of the 90-degree layer were 70MPa, for example, the new transverse crack would be created in between the pre-existing transverse cracks for a low crack density (Fig. 6.13) regardless of the length of the delamination. However, a new transverse crack would not develop under the delamination length (a/d) greater than 0.25 for a high crack density (Fig. 6.14). Additionally, one will be able to give a quantitative prediction whether a further transverse cracking damage will occur or a further delamination damage will occur, under the given bending load condition, if the results presented in Fig. 6.7 through Fig. 6.9 are compared along with Fig. 6.13 and Fig. 6.14.

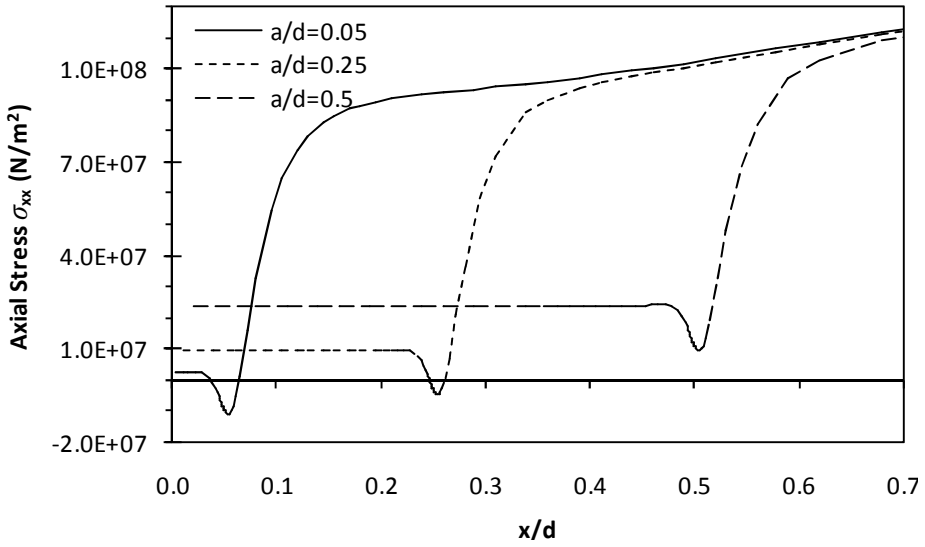

Fig. 6.13. $[90_1 / 0_3]_S$ Cross ply at a low crack density (1/d=0.25/mm)

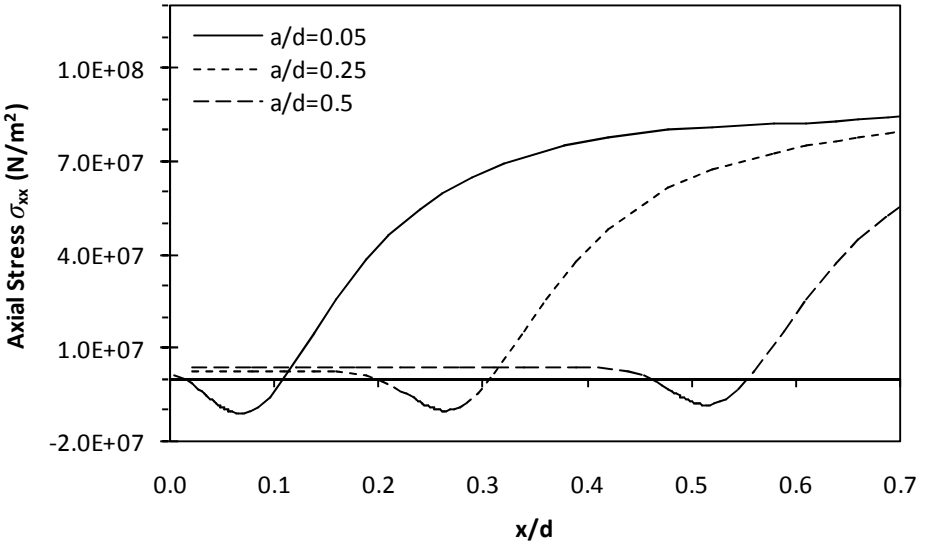

Fig. 6.14. $[90_1 / 0_3]_S$ Cross ply at a high crack density (1/d=1/mm)

6.3.2 90-Degree Plies and Transverse Cracking

The axial stress distribution along the outer surface of 90-degree layer in the tensile side of the laminated beam is presented in Fig. 6.15 and Fig. 6.16 for different combinations of 90 and 0-degree lay-ups. In order to demonstrate the effect of 90-degree plies, the total thickness of the laminate is remained the same and the number of plies of 90-degree and 0-degree are changed. The length of the interfacial crack is fixed with a ratio of a/d=0.25.

With delamination existing, thicker 90-degree layers tend to lower the axial stress. That is, less transverse cracking is expected under the same condition of other factors. This tendency is consistent for both of the low transverse crack density (Fig. 6.15) and the high transverse crack density (Fig. 6.16). It should be reminded that the effect of 90-degree plies on delamination was depending on the delamination length in the previous section (6.2).

The stress level at $x > a$ shows a bigger change due to the change of number of 90-degree plies when the transverse crack density is higher. Thus, transverse cracking progression tends to be more affected by the interfacial crack when the crack density is high, and increasing the number of 90-degree plies under the existence of delamination makes transverse cracking more difficult. In other words, the effect of 90-degree plies is not so prominent under the given length of interfacial crack when the transverse crack density is low.

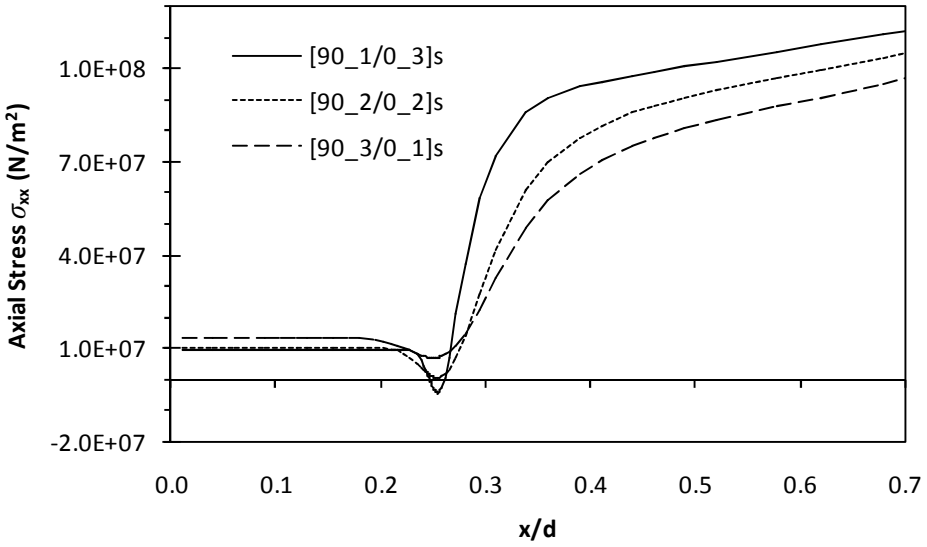

Fig. 6.15. Effect of 90-degree plies at a low crack density (1/d=0.25/mm)

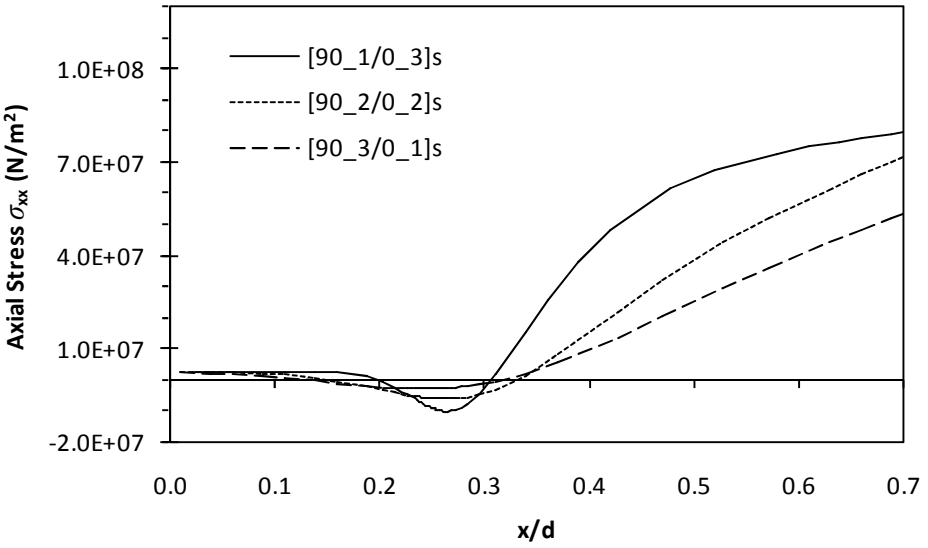

Fig. 6.16. Effect of 90-degree plies at a high crack density (1/d=1/mm)

CHAPTER VII

SUMMARY AND CONCLUSIONS

A finite element model for the laminated beam based on the von Kármán type nonlinear strains and layer-wise kinematics has been developed. The finite element model of layer-wise laminated beam provides solutions showing an excellent agreement with the exact elasticity solutions or stresses as well as deflections. The layer-wise laminated beam model is used to analyze the unit cell of the transversely cracked laminate in mesoscale, in order to determine the material properties of the damaged laminate. The analysis on the bending behavior of the transversely cracked laminated beam can be performed by replacing the material properties obtained from the mesoscale model for the cracked ply. As a result, two steps of numerical simulations can be accomplished using LWT and the effort to construct a number of meshes can be minimized in the present multi-scale damage analysis.

Using nonlinear laminated beam model based on LWT, a beam is analyzed under a distributed transverse load with a clamped-clamped boundary condition. It is found that the nonlinear beam model is necessary for the damage study, especially when the damage occurs under a large deformation so that the geometric nonlinearity develops before the material is damaged. Further, the feature of the largely deformed bending beam such as the shift of neutral axis can be captured by the nonlinear laminated beam model using LWT.

For the clamped-clamped bending beam studied, a sequential propagation of

transverse cracks has been successfully predicted. It is also found that the damage at the center of the bending beam affects the stress at the clamped boundary end whereas the damage at the clamped end does not disturb the stress at the center of the beam.

The layer-wise beam model is extended to consider interlaminar discontinuity in the displacement through the thickness. The Heaviside step function is incorporated in the formulation of layer-wise beam model, which successfully evaluates the local stresses around the interfacial crack. This model enables the strain energy release rate to be computed with a good accuracy.

The virtual crack closure method in the frame work of fracture mechanics is regarded as a simple and accurate way to compute the strain energy release rate or the stress intensity factor of the cracked strip. In particular, the application to the beam finite element model based on the layer-wise theory has been attempted and the accuracy of the solutions is satisfactory within a certain percentage of error comparing to the analytical values. The size of the finite elements at the crack tip usually shows a low sensitivity to the stress intensity factor, but to achieve a better accuracy without losing the modeling efficiency for the various case studies, the ratio of the crack tip element to the crack length ratio should be considered. In this study, only the homogeneous material has been examined for the sake of verifying the accuracy by comparing to the well known analytical results from the literature. However, the application of the virtual crack closure method combined with the layer-wise beam finite element model is capable of predicting the progress of delamination damage.

Two cases of delamination in $[90_m / 0_n]_S$ cross plies subjected to bending loads

are investigated using the finite element method based on the layer-wise beam theory. The boundary conditions imposed on the beam to be subjected to the bending causes a significant effect on the delamination growth and the strain energy release rate strongly depends on the location of the delamination crack tip because the bending moment distribution along the beam is determined by the boundary condition. The effect of boundary condition can be avoided by applying four-point bending which simulates a pure bending condition.

An interlaminar crack originated from a transverse crack in the 90-degree ply on the tensile side is primarily led by the fracture Mode I and the strain energy release rate is nearly constant under pure a bending condition if the delamination length is larger than a critical size. The interlamiar crack without transverse crack is driven by the fracture Mode II when the crack size is small and the primary fracture mode is shifting to the Mode I as the delamination length increases.

Very little effects are induced to the behavior of the delaminated beam by taking into account the von Kármán type nonlinearity in the numerical analysis. In this regards, the growth of delamination can occur when the beam deforms within the range that linear strains are applicable.

Interactions between the interlaminar cracks and the transverse cracks have been intensively studied in a cross-ply laminated beam with uniformly distributed damage subjected to the bending loads. The relationship between the transverse crack density and the delamination crack length is revealed that the higher the crack density becomes the less the delamination grows.

It is also found that the number of 90-degree plies sigificantly changes the delamination growth for a given crack density. The thickness of 90-degree layer also greatly affects the pattern of strain energy release rate curve, the characteristic delamination length and the effect of crack density as well. The failure mode contribution to the total strain energy release rate is changed as the thickness of 90-degree layer varies. The degree of mode contribution in delamination is also governed by the number of 90-degree plies and the crack density. The thckness of the 90-degree layer in the laminate makes Mode I more predominent.

The predominant fracture mode is governed by the crack density and the delamination length as well. When the crack density is low, Mode I fracture turns out to lead the delamination growth. However, the dominant fracture mode changes as the crack density increases, and Mode II becomes prominent. In the early stage of delamination, i.e. when the interlaminar crack is short, the predominant frailure mode driving the delamination growth is found to be Mode I. Mode II fracture leads the delamination as the interlaminar crack progresses.

Finally, main contributions of this research work can be summarized as follows:

1. A nonlinear finite element model based on the von Kármán type nonlinear strains is developed using the layer-wise theory to analyze delamination as well as transverse cracking in laminated beams under bending loads.
2. Employing the multiscale analyis approach, the effective material stiffness coefficients in the transversely cracked layer are extracted from a mesoscale

model and they are applied to a macroscale model to predict the sequential damage in a cross-ply laminated beam.

3. Nonlinearity in laminated beams under bending loads is found to develop before the initial transverse crack forms. Therefore, nonlinearity due to a moderately large flexural deformation should be taken into account in the analysis of transverse cracking in laminated beams under bending loads.
4. Boundary conditions significantly affect the behaviour of delamination and the predominant fracture mode is found to vary during the growth of delamination. Thus, unlike the progression of delamination under a tensile load, mode mixture should be considered for analysis of delamination under a bending load.
5. Delamination can progress in a laminated beam under a bending load before nonlinearity due to a large rotational deformation is prominent, and the general idea of linear analysis on delamination is numerically justified by comparing the results from linear and nonlinear analyses.
6. Interactions between intralaminar and interlaminar damage are investigated for cross-ply laminated beams under bending loads, and the growth of delamination originated from the tip of transverse crack is found to strongly depend on the thickness of 90-degree layers as well as the crack density. The effect of interfacial crack growth on the transverse cracking is also investigated in this study, and the quantatative prediction of damage progress is made with considering the interactions of the two damage modes.

REFERENCES

[1] Reddy, J. N., *Mechanics of Laminated Composite Plates and Shells – Theory and Analysis*, Boca Raton, FL, CRC Press, 2004.

[2] Levinson, M., "A new rectangular beam theory," *Journal of Sound and Vibration*, vol. 74, pp. 81-87, Jan. 1981.

[3] Reddy, J. N., "A simple higher order theory for laminated composite plates," *Journal of Applied Mechanics*, vol. 51, pp. 745-752, Dec. 1984.

[4] Reddy, J. N., "A generalization of two-dimensional theories of laminated composite plates," *Communications in Applied Numerical Methods*, vol. 3, pp. 173-180, May-Jun. 1987.

[5] Rosca, V. E., Poterasu, V.F., Taranu, N. and Rosca, B.G., "Finite-element model for laminated beam-plates composite using layerwise displacement theory," *Engineering Transactions*, vol. 50(3), pp. 165-176, 2002.

[6] Robbins, D. H., and Reddy, J. N., "Analysis of piezoelectrically actuated beams using a layer-wise displacement theory," *Computers & Structures*, vol. 41(2), pp. 265-279, Jan. 1991.

[7] Reifsnider, K. L., and Masters, J. E., "Investigation of characteristic damage states in composite laminates," ASME Paper, 78WA/Aero-4, 1978, p. 10.

[8] Bader, M. G., Bailey, J. E., Curtis, P. T., and Parvizi, A., "Mechanisms of initiation and development of damage in multi-axial fibre-reinforced plastics laminates," in *Proc. 3rd. Int. Symp. Mech. Behavior of Matls*., 1980, Cambridge, U.K., p. 227.

[9] Aveston, J., Cooper, G. A., and Kelly, A., "Single and multiple fracture," in *The Properties of Fiber Composites, Conf. Proc. of the National Physical Laboratory*, 1971, Surrey, England, pp. 15-26.

[10] Garrett, K. W., and Bailey, J. E., "Multiple transverse fracture in 90^{o} cross-ply laminates of a glass fiber-reinforced polyester," *Journal of Materials Science,* vol. 112, pp. 157-168, Jan. 1977.

[11] Highsmith, A. L., and Reifsnider, K. L., "Stiffness reduction mechanisms in composite laminates," *ASTM Special Technical Publication*, vol. 775, pp. 103-117, Jan. 1982.

[12] Smith, P. A., and Ogin, S. L., "On transverse matrix cracking in cross-ply laminates loaded in simple bending," *Composites: Part A*, vol. 30, pp. 1003-1008, Aug. 1999.

[13] Hashin, Z., "Analysis of cracked laminates: A variational approach," *Mechanics of Materials*, vol. 4, pp. 121-136, Jul. 1985.

[14] Hashin, Z., "Analysis of orthogonally cracked laminates under tension" *Journal of Applied Mechanics*, vol. 54, pp. 872-879, Dec. 1987.

[15] Nairn, J. A., and Hu, S., "The initiation and growth of delaminations induced by matrix microcracks in laminated composites," *International Journal of Fracture Mechanics*, vol. 57, pp. 1-24, Sep. 1992.

[16] Varna, J., Joffe, R., and Talreja, R., "A Synergistic damage mechanics analysis of transverse cracking in $[\pm\theta/90_4]_s$ laminates," *Composite Science and Technology*, vol. 61, pp. 657-665, Apr. 2001.

[17]Krajcinovic, D. K., "Continuum damage mechanics," *Applied Mathematics Reviews*, vol. 37(1), pp. 1-6, Jan. 1984.

[18] Lemaitre, J., "How to use damage mechanics," *Nuclear Engineering and Design*, vol. 80, pp. 233-245, Jul. 1984.

[19] Kachanov, L. M., "Rupture time under creep conditions," *International Journal of Fracture*, vol. 97, pp. 11-18, Apr. 1999.

[20] Talreja, R., "A continuum mechanics characterization of damage in composite materials," *Proc. Royal Soc. London*, A 399, 1985, pp. 195-216.

[21] Talreja, R., "Transverse cracking and stiffness reduction in composite laminates," *Journal of Composite Materials*, vol. 19, pp. 353-375, Jan. 1985.

[22] Thionnet, A. and Renard, J., "Meso-macro approach to transverse cracking in laminated composites using Talreja's model," *Composites Engineering*, vol. 3(9), pp. 851-871, 1993.

[23] Boniface, L., Ogin, S.L. and Smith, P.A., "Strain energy release rates and the fatigue growth of matrix cracks in model arrays in composite laminates," in *Proc. Mathematical and Physical Sciences*, vol. 432, 1991, pp. 427-444.

[24] Li, S., Reid, R. and Soden, P.D., "A continuum damage model for transverse matrix cracking in laminated fibre-reinforced composites," *Phil. Trans. R. Soc. Lond*. A356, pp. 2379-2412, Oct. 1998.

[25] Crossman, F. W., and Wang, A. S. D., "Dependence of transverse cracking and delamination on ply thickness in graphite/epoxy laminates," *Damage in Composite Materials*, *ASTM Special Technical Publication*, vol. 775, pp. 118-139, Jan. 1982.

[26] O'Brien, T. K., "Characterization of delamination onset and growth in a composite laminate," *Damage in Composite Materials, ASTM Special Technical Publication*, vol. 775, pp. 140-167, Jan. 1982.

[27] Wang, A. S. D., Kishore, N. N., and Li, C. A., "Crack development in graphite-epoxy cross-ply laminates under uniaxial tension.," *Composites Science and Technology*, vol. 24, pp. 1-31, Jan. 1985.

[28] Griffith, A. A., "Phenomena of rupture and flow in solids," *Royal Society of London: Philosophical Transactions*, vol. 221, pp. 163-198, Oct. 1920.

[29] Rice, J. E., "Mathematical analysis in the mechanics of fracture," in *Fracture - An Advanced Treatise*, H. Liebowitz, Ed., New York, Academic Press, pp. 191-311, 1968.

[30] Gurtin, M. E., "On the energy release rate in quasi-static elastic crack propagation," *Journal of Elasticity*, vol. 9, pp. 187-195, Apr. 1979.

[31] Pagano, N. J., and Pipes, R. B., "Some observations on the interlaminar strength of composite laminates," *International Journal of Mechanics and Science*, vol. 15, pp. 679-688, Aug. 1973.

[32] Kim, K. S., "Characteristics of free edge delamination in angle-ply laminate," *International Conf. on Composite Materials ICCM-V*, San Diego, CA, 1985, pp. 347-361.

[33] Kim, R. Y., "Experimental observations of free-edge delamination" in *Interlaminar Response of Composite Materials*, Pagano, N. J. Ed., Amsterdam, The Netherlands, Elsevier Science Publishers B.V., pp. 111-160, 1989.

[34] Kim, R. Y., "Initiation of free-edge delamination in composite laminates," *Key Engineering Materials*, vol. 37, pp. 103-136, 1989.

[35] Brewer, J., and Lagace, P. A., "Quadratic stress criterion for initiation of delamination," *Journal of Composite Materials*, vol. 22, pp. 1141-1155, Jan. 1988.

[36] Wang, A. S. D., "Growth mechanisms of transverse cracks and ply delamination in composite laminates," in *Proc. of ICCM-3*, Paris, France, 1980, pp. 170-185.

[37] Wang, A. S. D., Kishore, N. N., and Feng, W. W., "On mixed mode fracture in off-axis unidirectional graphite-epoxy composites," in *Progress in Science and Engineering of Composites, Proc. of ICCM-IV*, Tokyo, Japan, 1982, pp. 599-606.

[38] Wang, A. S. D., Slomiana, M., and Bucinell, R. B., "Delamination crack growth in composite laminates," *Delamination and Debonding of Materials*, *ASTM Sepcial Technical Publication*, vol. 876, pp. 135-167, Jan. 1985.

[39] Johannesson, T., and Blikstad, M., "Fractography and fracture criteria of the delamination process," *Delamination and Debonding of Materials, ASTM Special Technical Publication*, vol. 876, pp. 411-423, Jan. 1985.

[40] Hwu, C., Kao, C. J., and Chang, L. E., "Delamination fracture criteria for composite laminates, Critical strain energy release rate experimentally measured for CFRP specimen with pre-existing delamination cracks", *Journal of Composite Materials*, vol. 29(15), pp. 1962-1988, Oct. 1995.

[41] Sih, G. C., Paris, P. C., and Irwin, G. R., "On cracks in rectilinearly anisotropic bodies," *International Journal of Fracture Mechanics*, vol. 1, pp. 189-203, Sep. 1965.

[42] O'Brien, T. K., "Mixed mode strain energy release rate effects on edge delamination of composites," *Effects of Defects in Composite Materials, ASTM Special Technical Publication*, vol. 836, pp. 125-142, Jan. 1984.

[43] Wilkins, D. J., Eisenmann, J. R., Camin, R. A., Margolis, W. S., and Benson, R. A., "Characterizing delamination growth in graphite-epoxy," *Damage in Composite Materials, ASTM Special Technical Publication*, vol. 775, pp. 168-183, Jan. 1982.

[44] Hahn, H. T., "Mixed-mode fracture criterion for composite materials," *Composites Technology Review*, vol. 5, pp. 26-29, Spring 1983.

[45] Takeda, N., Sierakowski, R. L., and Malvern, L. E., "Microscopic observations of cross-sections of impacted composite laminates," *Composites Technology Review*, vol. 4, pp. 40–44, Summer 1982.

[46] Joshi, S. P., and Sun, C. T., "Impact-induced fracture in a laminated composite," *Journal of Composite Materials*, vol. 19, pp. 51–66, Jan. 1985.

[47] Liu, D., and Malvern, L. E., "Matrix cracking in impacted glass/epoxy plates," *Journal of Composite Materials*, vol. 21, pp. 594–609, Jan. 1987.

[48] Echaani, J., Trochu, F., Pham, X. T., and Ouellet, M., "Theoretical and experimental investigation of failure and damage progression of graphite-epoxy composites in flexural bending test," *Journal of Reinforced Plastics and Composites*, vol. 15, pp. 740-755, Jul. 1996.

[49] Murri, G. B., and Guynn, E. G., "Analysis of delamination growth from matrix cracks in laminates subjected to bending loads," *Composite Materials: Testing and Design, ASTM Special Technical Publication*, vol. 972, pp. 322-339, Jan. 1988.

[50] Choi, H. Y., Downs, R. J., and Chang, F. K., "A new approach toward understanding damage mechanisms and mechanics of laminated composites due to low-velocity impact: Part I—Experiments," *Journal of Composite Materials*, vol. 25, pp. 992–1011, Aug. 1991.

[51] Choi, H. Y., Wu, H. Y. T., and Chang, F. K., "A new approach toward understanding damage mechanisms and mechanics of laminated composites due to low-velocity impact: Part II —Analysis," *Journal of Composite Materials*, vol. 25, pp. 1012–1038, Aug. 1991.

[52] Salpekar, S. A., "Analysis of delamination in cross-ply laminates initiating from impact induced matrix cracking," *Journal of Composites Technology & Research*, vol. 15, pp. 88-94, Summer 1993.

[53] Kim, Y., and Im, S., "Delamination cracks originating from transverse cracking in cross-ply laminates under various loadings," *International Journal of solids Structures*, vol. 30, pp. 2143-2161, Jan. 1993.

[54] Liu, S., and Chang, F., "Matrix cracking effect on delamination growth in composite laminates induced by a spherical indenter," *Journal of Composite Materials*, vol. 28, pp. 940-977, May 1994.

[55] Zhang, J., and Lewandowski, J. J., "Delamination study using four-point bending of bilayers," *Journal of Materials Science*, vol. 32, pp. 3851-3856, Jul. 1997.

[56] Dharani, L. R., Wei, J., Ji, F. S., and Zhao, J. H., "Saturation of transverse cracking with delamination in polymer cross-ply composite laminates," *International Journal of Damage Mechanics*, vol. 12, pp. 89-114, Apr. 2003.

[57] Kuriakose, S., "Analysis of damage in composite laminates under bending," Ph.D dissertation, School of Aerospace Engineering, Georgia Institute of Technology, Atlanta, GA, 2002.

[58] Kondo, K., "Delamination originating from transverse crack tips in laminates under mechanical loadings," *Journal of Reinforced Plastics and Composites*, vol. 18, pp. 1231-1241, Sep. 1999.

[59] Javidrad, F., "Experimental and numerical study of delamination growth induced by a transverse crack in unidirectional laminates subjected to bending loads," *Journal of Testing and Evaluation*, vol. 28, pp. 12-21, Jan. 2000.

[60] Kuboki, T., Jar, P.-Y. B., and Cheng, J. J. R., "Damage development in glass-fiber-reinforced polymers(GFRP) under transverse loading," *Annual Technical Conf.-ANTEC*, Nashville, TN, 2003 , pp. 2168-2172.

[61] Takeda, N., and Ogihara, S., "Initiation and growth of delamination from the tips of transverse cracks in CFRP cross-ply laminates," *Composite Science and Technology*, vol. 52, pp. 309-318, Jan. 1994.

[62] Reddy, J. N., *Energy Principles and Variational Methods in Applied Mechanics*, Hoboken, NJ, John Wiley & Sons Inc. , 2002.

[63] Reddy, J. N., *An Iintroduction to Nonlinear Finite Element Analysis*, New York, Oxford University Press, 2004.

[64] Pagano, N. J., "Exact solutions for composite laminates in cylindrical bending," *Journal of Composite Materials*, vol. 3, pp. 398-411, Jan. 1969.

[65] Talreja, R., "Internal variable damage mechanics of composite materials," in *Yielding Damage and Failure of Anisotropic Solids*, London, Mechanical Engineering Publications, pp. 509-533, 1990.

[66] Li, S., Reid, R. and Soden, P.D., "A finite strip analysis of cracked laminates," *Mechanics of Materials*, vol. 18, pp. 289-311, Oct. 1994.

[67] Zhao, J., S. V. Hoa, Xiao, X. R., and Hanna, I., "Global/local approach using partial hybrid finite element analysis of stress fields in laminated composites with Mid-plane delamination under bending," *Journal of Reinforced Plastics and Composites*, vol. 18(9), pp. 827-843, Jun. 1999.

[68] Fujii, T., and Sun, Q., "Stress distribution of fiberglass reinforced plastic beam with a delamination under three point bending," in *Proc. of the Japan Congress on Material Research*, Tokyo, Japan, 1984, pp. 257-261.

[69] Wang, S. S., "Edge delamination in angle-ply composite laminates," *AIAA/ASME/ ASCE/AHS Structural Dynamics and Materials Conf.*, Atlanta, GA, 1981, pp. 474-484.

[70] Murthy, P. L. N., and Chamis, C. C., "Free-edge delamination: Laminate width and loading conditions effects," *Journal of Composite Technology and Research*, vol. 11(1), pp. 15-22, Spring 1989.

[71] Feraboli, P., and Kedward, K. T., "Four point bend interlaminar shear testing of uni- and multi-directional carbon/epoxy composite systems," *Composites: Part 34*, pp. 1265-1271, Dec. 2003.

[72] Irwin, G. R., "Analysis of stresses and strains near the end of a crack traversing a plate," *Journal of Applied Mechanics*, vol. 24, pp. 361-364, Sep. 1957.

[73] Westergaard, H. M., "Bearing pressures and cracks," *Journal of Applied Mechanics*, vol. 6, pp. 49-53, Jun. 1939.

[74] Broek, D., *Elementary Engineering Fracture Mechanics*, Dordrecht, The Netherlands, Martinus Nijhoff Publishers, 1986.

[75] Paris, P. C., and Sih, G., "Fracture toughness testing and its applications," *ASTM Special Technical Publication*, vol. 381, pp. 30-81, Jan. 1965.

[76] Fedderson, C., "Discussion on plane strain crack toughness testing," *Plane Strain Crack Toughness Testing of High Strength Metallic Materials*, *ASTM Special Technical Publication*, No. 410, pp. 77-79, Jan. 1967.

[77] Isida, M., "On the tension of a strip with a central elliptical hole," *Transactions of the Japan Society of Mechanical Engineers*, vol. 21, pp. 507-518, 1955.

[78] Rybicki, E. F., and Kanninen, M. F., "A finite element calculation of stress intensity factors by a modified crack closure integral," *Engineering Fracture Mechanics*, vol. 9, pp. 931-938, Jan. 1977.

[79] Mowbray, D. F., "A note of the finite element method in linear fracture mechanics," *Engineering Fracture Mechanics*, vol. 2, pp. 173-176, Nov. 1970.

[80] Walsh Jr., R. M., "Strain energy release rate determination of stress intensity factors by finite element methods," M.S. thesis, Center for Composite Materials, University of Delaware, Newark, DE, 1982.

[81] Parks, D. M., "Stiffness derivative finite element technique for determination of elastic tip stress intensity factors," *International Journal of Fracture Mechanics*, vol. 10, pp. 487-502, Dec. 1974.

[82] Hellen, T. K., "On the method of virtual crack extension," *International Journal for Numerical Methods in Engineering*, vol. 9(1), pp. 187-207, Spring 1975.

[83] Raju, I. S., "Calculation of strain-energy release rates with higher order and singular finite elements," *Engineering Fracture Mechanics*, vol. 28, pp. 251-274, Jan. 1987.

[84] Bowie, O. L., "Rectangular tensile sheet with symmetric edge cracks," *Journal of Applied Mechanics*, vol. 31, pp. 208-212, Jun. 1964.

VITA

Wook Jin Na graduated from Korea University with the Bachelor of Science degree in mechanical engineering in 1995. He joined the Center for Noise and Vibration Control at the Korea Advanced Institute of Science and Technology (KAIST) in March 1995 and received his Master of Science degree in mechanical engineering in February 1997.

After working for Hyundai Motor Company as a research engineer in a body design team from 1997, he resumed his education for the Ph.D degree in mechanical engineering at Texas A&M University in September 2003 and he received his Ph.D in May 2008. His research interests include structural dynamics, progressive damage in composite laminates and development of finite element method.

Wook Jin Na may be reached through his email, woodyna@gmail.com or at Department of Mechanical Engineering c/o Dr. J. N. Reddy, Texas A&M University, College Station, TX 77843.